Université d'Ottawa · University of Ottawa

Université d'Ottawa · University of Ottawa

FACULTÉ DES ÉTUDES SUPÉRIEURES ET POSTDOCTORALES

FACULTY OF GRADUATE AND POSTDOCTORAL STUDIES

Guy GAGNON

AUTEUR DE LA THÈSE - AUTHOR OF THESIS

M. A. Sc. (Electrical Engineering)

GRADE - DEGREE

Department of Electrical Engineering

FACULTÉ, ÉCOLE, DÉPARTEMENT - FACULTY, SCHOOL, DEPARTMENT

TITRE DE LA THÈSE - TITLE OF THE THESIS

Thermo-optic Variable Optical Attenuators Using Plasmon-polariton Waveguides

P. Berini

DIRECTEUR DE LA THÈSE - THESIS SUPERVISOR

CO-DIRECTEUR DE LA THÈSE - THESIS CO-SUPERVISOR

EXAMINATEURS DE LA THÈSE - THESIS EXAMINERS

M Cada

G. Tarr

J.-M. De Koninck, Ph.D

LE DOYEN DE LA FACULTÉ DES ÉTUDES SUPÉRIEURES ET POSTDOCTORALES

DEAN OF THE FACULTY OF GRADUATE AND POSTDOCTORAL STUDIES

Thermo-Optic Variable Optical Attenuators Using Plasmon-Polariton Waveguides

By:

Guy Gagnon. B.A.Sc

A thesis submitted to the
School of Graduate Studies and Research
in partial fulfillment of the requirements for the degree of

Master of Applied Science

Ottawa-Carleton Institute for Electrical Engineering
Department of Electrical Engineering
Faculty of Engineering
University of Ottawa

Your file Votre référence
ISBN: 0-494-01474-1
Our file Notre référence
ISBN: 0-494-01474-1

Abstract

A plasmon-polariton waveguide is investigated for its thermo-optic capability for the first time in the context of variable optical attenuators. The optical waveguide's metal core embedded into thermo-optic materials can be heated due to ohmic losses when current is injected through it. Hence, the optical and electrical function is agglomerated into the same waveguide layer. Heat changes the surrounding materials' refractive index and affects light propagation. The variable optical attenuator's response time was shown to be as fast as 50μs. The 8μm x 20nm metal waveguide achieves 19dB extinction ratio with 222 mW of electrical power consumption. Many other waveguide's characteristics were obtained experimentally and through thermal, electrical and optical modeling.

The metal waveguide was used as a non-invasive, direct and accurate temperature sensor. Electromigration and electrostatic discharge were investigated as the waveguide's degrading mechanisms. A novel optical method to study thin metal films' degradation due to electromigration is suggested.

Dedication

I would like to dedicate this thesis to my wife and family.

Abstract

A plasmon-polariton waveguide is investigated for the first time for its thermo-optic capability in the context of variable optical attenuators. The core of the optical waveguide embedded into thermo-optic materials is made of metal and can therefore be heated due to ohmic losses when current is injected through it. Hence, the optical and electrical function is agglomerated into the same waveguide layer. Heat changes the refractive index of the surrounding materials and affects propagation of light. The response time of the device was shown to be as fast as 50μs, with smaller values being possible. The 8μm x 20nm metal waveguide achieves 19dB extinction ratio with 222 mW of electrical power consumption with significant improvements being possible. Mode field diameter, propagation loss, coupling loss and return loss of the waveguides were also obtained experimentally.

The metal optical waveguide was calibrated and used as a non-invasive, direct and accurate temperature sensor useful in the context of thermo-optic devices. It is the first time that the core of an optical waveguide is simultaneously used as a temperature sensor.

Electromigration tests were conducted to determine if this phenomenon is a limiting factor to the regime of operation of the variable optical attenuator. A novel optical method to study the degradation of thin metal films due to electromigration is suggested. Furthermore, the waveguide is shown to be very susceptible to the damaging effect of an electrostatic discharge.

A 2D steady-state finite-difference method based on the heat diffusion equation was developed to predict the temperature distribution surrounding the heated plasmon-polariton waveguide for the first time. Through the thermo-optic coefficient, the new refractive index distribution can be determined.

A 1D modal analysis based on Maxwell's equations solving a thin film slab structure embedded in a spatially dispersive dielectric medium resulting from heating was obtained for the first time and used as an approximation to the 2D model. The two most significant modes were investigated: s_b and s_L modes. Performance parameters resulting from the model are presented.

Results from the model are compared to that from the experiments. Improvements and suggestions were made to the thermal/optical model.

Acknowledgements

I would like to acknowledge the support of my thesis supervisor, Pierre Berini, Ph. D., from the University of Ottawa, and Spectalis Corp. throughout the course of this work.

This research project was performed at Spectalis Corp. who had the necessary equipment and facilities. The project was also exclusively funded by Spectalis Corp. who owns the intellectual property. More specifically, I would like to thank Robert Charbonneau for his enlightening conversations and for reviewing this work.

I would like to acknowledge Carleton University's fabrication laboratory for having made its facilities and equipment available to Spectalis Corp. to be able to build the integrated planar lightwave circuit used in this work. I would like to thank Spectalis' fabrication team. A particular thanks to Nancy Lahoud and Angela Burns without whom the samples would never have been built.

Table of contents

List of Figures

List of acronyms

1D:	One-dimensional
2D:	Two-dimensional
3D:	Three-dimensional
ATR:	Attenuated total reflection
AFM:	Atomic Force Microscopy
DUT:	Device under test
EO:	Electro-optic
ER:	Extinction ratio
ESD:	Electro-static discharge
FDM:	Finite difference method
FOTP:	Fiber optic test procedure
IL:	Insertion loss
MMF:	Multimode fiber
MZ:	Mach-Zehnder
P1:	Port 1
P2:	Port 2
P3:	Port 3
PDL:	Polarization dependent loss
PLC:	Planar lightwave circuit
PMF:	Polarization maintaining fiber
SMF:	Single mode fiber
TEC:	Thermo-electric cooler
TM:	Transverse magnetic
TO:	Thermo-optic
TOC:	Thermo-optic coefficient
VOA:	Variable optical attenuator

List of constants

a_b: Asymmetric bound mode supported by a thin metal film slab.
a_L: Asymmetric leaky mode supported by a thin metal film slab.
aa_b^0: Asymmetric-asymmetric bound mode supported by a thin metal film of finite width.
as_b^0: Asymmetric-symmetric bound mode supported by a thin metal film of finite width.
c_p: Heat capacity.
D: Density.
E: Electronic charge, $e = 1.602 \times 10^{-19}$ Coulomb.
$\vec{E}$: Electric field vector.
E_{eg}: Excitonic band gap energy.
$E_{x_i}(z)$: Electric field's x component dependence on z position, in medium i.
$E_{z_i}(z)$: Electric field's z component dependence on z position, in medium i.
$\vec{H}$: Magnetic field vector.
$H_{y_i}(z)$: Magnetic field's y component dependence on z position, in medium i.
k_0: Propagation constant in free space (vacuum), $k_0 = \dfrac{2\pi}{\lambda}$.
k_x: Propagation constant in the x direction, $k_x = \beta - j\alpha$, equal in all media.
k_{z_i}: Propagation constant in the z direction, in medium i.
$\vec{J}$: Current density vector.
K: Thermal conductivity.
m_0: Effective mass of conduction electrons.
n: Refractive index.
N: Density of conduction electrons.
P: Atmospheric pressure.
Q''_{gen}: Volumetric heat generation.
$\vec{Q}''$: Power flux density.
$\vec{Q}$: Power flux.
R: Thermal resistance.
s_b: Symmetric bound mode supported by a thin metal film slab.
sa_b^0: Symmetric-asymmetric bound mode supported by a thin metal film of finite width.
ss_b^0: Symmetric-symmetric bound mode supported by a thin metal film finite in width.
$\vec{S}$: Poynting vector, $\overline{S} = \overline{E} \times \overline{H}^*$.
S_x: x component of Poynting vector.

S_z: z component of Poynting vector.
t: Time
T: Temperature.
α : Attenuation constant. Imaginary part of the propagation constant.
α_T : Thermal expansion.
β : Phase constant. Real part of the propagation constant.
δ : Temperature coefficient of resistivity.
ε : Permittivity of a material.
ε_0 : Permittivity of free space (vacuum).
ε' : Real part of the permittivity of a material.
ε'' : Imaginary part of the permittivity of a material.
ε_r : Relative permittivity of a material.
μ_0 : Permeability of free space (vacuum).
μ_r : Relative permeability.
λ : Wavelength.
λ_{ig} : Wavelength associated with the isentropic band gap.
ψ : Normalization factor.
ρ : DC electrical resistivity.
σ : DC electrical conductivity.
τ : Relaxation time of electrons.
υ : Effective electron collision frequency.
ω : Frequency of electromagnetic wave.
ω_p : Plasma frequency.
$\frac{dn}{dT}$: Thermo-optic coefficient.
$h(\theta_a + \theta_b)$: Distance between discretization points.
$\frac{1}{E_{eg}}\frac{dE_{eg}}{dT}$: Temperature coefficient of the excitonic band gap.

1. Introduction

1.1 Purpose

The purpose of this work is to introduce the thermo-optic (TO) effect within a new metal optical waveguide technology and to study its behavior within the context of TO variable optical attenuators (VOAs).

1.2 Contributions

This thesis makes a number of contributions to the advancement of science and engineering. For the first time, an active capability is introduced to a new metal optical waveguide technology, in particular, the TO effect. The TO effect is used to affect the electromagnetic field propagating through a waveguide; hence, it can be used to modulate or attenuate an optical signal. VOAs based on mode cutoff are a relatively new concept within TO applications and the present thesis suggests a novel way of achieving this. The metal optical waveguide technology simplifies fabrication of active devices since the electrical and optical function is agglomerated into a single waveguide layer. The metal optical waveguide used as a heater influences light more efficiently than that of conventional thin film heating technologies. The heat source is already in the optical path such that little heat diffusion is needed to affect the optical mode substantially; however, heat diffusion is necessary for cooling. It follows that the device size, power consumption and switching time of the device may be reduced in comparison to other conventional planar lightwave circuit (PLC) TO VOA technologies. Some inherent properties of the metal optical waveguide enable accurate, direct and non-invasive temperature monitoring of the device, which may be useful for TO devices. Electromigation tests are conducted on the metal waveguide and a new qualitative optical method to monitor the degradation of thin films due to electromigration is suggested and demonstrated experimentally as this method is an alternative to the resistance measurements and scanning electron microscopy. The failure of the 1D modal analysis to predict the waveguide's behavior suggests that a more elaborate optical model be used such as a 2D or 3D model.

1.3 Organization

The current chapter will introduce the TO effect and its use in the context of VOAs. Performance parameters of TO VOAs will be presented. Subsequently, current TO VOAs will be presented and criticized.

In Chapter 2, a review, which led to the development of plasmon-polariton waveguides, will be presented. Furthermore, we will introduce the basic theory and principles explaining the behavior of the plasmon-polariton waveguides. Finally, the principles from which the TO VOA functionality is accomplished using plasmon-polariton waveguides will be revealed.

Chapter 3 investigates experimentally some aspects of the performance of the thin metal film TO VOA based on mode cutoff for a simple structure. Chapter 3 also introduces accurate, direct and non-invasive temperature monitoring of the metal waveguide, which is useful in the context of TO devices. Given the high current densities injected into the waveguide, the possible degradation due to electromigration is investigated. Based on this simple investigation, we suggest a new way to investigate electromigration within the context of metal optical waveguides.

In order to have more insight on the behavior of the waveguide and to be able to predict its behavior for design purposes a model was developed. One of the goals was to develop a model that was not too computationally intensive, but still accurate enough to predict the behavior of the waveguide. The smaller the domain of computation, the less computationally intensive it is, which means that a model with reduced dimensionality will generate results more rapidly, but sometimes less accurately. We will determine if these inaccuracies have an important impact by comparing experimental results with those provided by the model.

The model is separated into two main parts. The first part is a 2D steady-state thermal model, which predicts the temperature distribution in the structure resulting from heating the waveguide. The thermal model is validated by comparison with results from the literature. The results of the 2D thermal model for the TO VOA structure are presented in Chapter 4. From the temperature distribution, the refractive index distribution in the structure may be determined from the thermo-optic coefficient (TOC) of each material.

The second part of the model is a 1D optical model. The optical model uses the refractive index distribution found earlier to obtain the results. The model is validated by comparison with literature. The results of the 1D optical model for the TO VOA structure are presented in chapter 5. Finally, the last chapter expresses the concluding remarks and summarizes the thesis. Improvements and future work are also presented.

1.4 Variable optical attenuators

VOAs have a fundamental role in optics; they control the power level of an optical signal. There is a wide range of applications where VOAs can be used. For example, they can be used to equalize the optical output power of different channels in a dense wavelength division multiplexing system. The VOA function can be implemented in several ways such as by using the electro-optic (EO) and TO effect. In general, the TO effect is slower and consumes more power than the EO effect, but the design of TO devices is simpler and their construction is cheaper due to lower material cost. Since no active devices have ever been designed in this new metal optical planar waveguide technology, it would be wise to start with something simple to design and build. For this reason, in this present work, a VOA will be designed using the TO effect. Studying the behavior of the thermo-optic VOA may give us an insight on how to develop an EO modulator or EO VOA in the future.

1.4.1 Thermo-optic VOAs: The thermo-optic effect

The TO effect is a phenomenon by which heat can influence the refractive index of a material. A simple linear model describing the refractive index change due to a temperature variation is given by Equation (1.1).

$$n\big|_{\lambda_0,P_0,T_1} = n\big|_{\lambda_0,P_0,T_0} + (T_1 - T_0)\frac{dn}{dT}\bigg|_{\lambda_0,P_0,T_{\frac{1}{2}}} \tag{1.1}$$

Where "n", λ_0, P_0 and "T" are the refractive index, the free space wavelength, pressure and temperature respectively. The subscripts only reflect the conditions in which the refractive index was obtained. The variation of the refractive index as a function of temperature and at a constant pressure is called the thermo-optic coefficient (TOC) and is denoted $\frac{dn}{dT}$. The

TOC is usually assumed constant over the range of temperature considered for practical purposes. This is usually valid if the temperature range is relatively small.

If the TOC is non-constant in the range of temperature considered, then it is possible to decompose it as a sum over smaller ranges of constant TOC. This is denoted:

$$n\big|_{\lambda_o,P_o,T_N} = n\big|_{\lambda_o,P_o,T_1} + \sum_{i=1}^{N-1}\left((T_{i+1} - T_i)\frac{dn}{dT}\bigg|_{\lambda_o,P_o,T_{i+\frac{1}{2}}} \right) \tag{1.2}$$

where "i" and "N" are the ith sub-range and total number of sub-ranges respectively. $\sum_{i=1}^{N-1}(T_{i+1} - T_i) = T_N - T_1$ represents the total temperature range considered. In practice, the TOC usually varies for a range of temperature 100°C or less [1]. The behavior of the TOC as a function of temperature and wavelength is best described by a new physically meaningful relation [1]:

$$2n\frac{dn}{dT} = (n_o{}^2 - 1)\left[-3\alpha_T R - \frac{1}{E_{eg}}\frac{dE_{eg}}{dT}R^2 \right] \tag{1.3}$$

where n, $\frac{dn}{dT}$, n_o, α_T are the room-temperature refractive index, its variation with temperature, the low-frequency refractive index in the IR region and the thermal expansion coefficient respectively. $R = \frac{\lambda^2}{\lambda^2 - \lambda_{ig}^2}$ where λ and λ_{ig} are the wavelength and the wavelength associated with the isentropic band gap lying in the UV region respectively. $\frac{1}{E_{eg}}\frac{dE_{eg}}{dT}$ is the temperature coefficient of the excitonic band gap. Hence, Equation (1.3) shows that the refractive index change of Equation (1.1) and (1.2) depends on these physically meaningful parameters. More details about the origin of this equation and its limitations are given in reference [1]. Alternatively, the TOC can also be obtained via experimental measurements.

From relations (1.1), (1.2) or (1.3) and knowing the temperature distribution of the optical device, it is possible to determine the refractive index distribution resulting from applied heat.

1.4.2 Performance parameters

A TO VOA described as having good performance parameters is one that has a fast response time, low electrical power consumption, large extinction ratio (ER), low insertion loss (IL), low thermal cross-talk, low return loss, low polarization dependent loss (PDL), low polarization mode dispersion and is broadband. Other parameters of importance are compactness, low cost, low drive voltage and ease of fabrication. Some of the above parameters are inherent to the technology selected while other parameters can be improved with careful design.

Power consumption depends on the ER desired, material properties and the geometry of the structure. Materials with high absolute TOCs are of interest since less heat is required to affect the refractive index by an equal amount than that of low absolute TOC materials. A material with low thermal conductivity will reduce the device's power consumption to obtain the same temperature increase if it is located between the heat source and heat sink. Furthermore, the heat source must be very close to the optical waveguide and the low thermal conductivity material must be in the optical path.

The response time is subdivided into two categories: the rise time and the fall time. The rise time of an optical device is the minimum time for which the output optical power increases from 10% to 90% of its steady "on" state. The fall time of an optical device is the minimum time for which the output optical power reduces from 90% to 10% of its steady "on" state. The response time is determined by the diffusivity of the material and the structure geometry. A material with high thermal diffusivity will have a shorter response time than that with low thermal diffusivity. The diffusivity is a function of the thermal conductivity, density and specific heat of a material. Usually, selecting a material with low thermal conductivity translates into a slower response time. Hence, usually a trade-off occurs between power consumption and the response time.

The ER is defined as the ratio of the output optical power between the "off" state and "on" state of the device. The ER of a VOA depends on the materials, electrical power consumption and geometry of the structure; hence, it depends on a careful design.

The return loss is the amount of optical power reflected back to the optical source relative to the amount of optical power launched by the optical source. The return loss may be relevant since it contributes to the IL and may destabilize the optical source. To minimize the return loss, materials with matching refractive indices are used. Air gaps between connections or devices must be eliminated and this can be achieved by using index matching oil or a similar technique. The angled polished connectors are probably the best type of connector to minimize reflection back into the laser source.

A device is said to be broadband if it meets the required specifications in a large range of wavelengths. The device will be broadband in accordance to its geometry and its constituent materials.

A device with low PDL has essentially the same IL independent of the input polarization. The standard medium through which light propagates in a network is single mode fibers (SMFs) or multimode fibers (MMFs). The polarization state coming out of these fibers is random and varies with time. As a result, most devices within the network must have low PDL.

The IL of the device is dependent on the input and output coupling loss and return loss of the device along with the propagating loss of the waveguide, which is also dependent on material loss. In essence, it is important that the waveguide geometry be properly designed and its constituent materials are chosen with low loss and are compatible with the other materials in the system.

Having a low thermal-cross talk in a multi-channel system refers to limiting the influence of heat to its own channel. In this work, we are analyzing a single channel such that this parameter is of small importance.

Polarization mode dispersion occurs when modes of different polarizations supported by a waveguide or device propagate at different speeds causing pulses to spread and become difficult to detect. This effect must be minimized.

In this thesis, attention was focused towards the response time, power consumption and ER.

1.4.3 Literary Review

VOAs may be referred to as switches or modulators since all these devices have similar functions. In any case, there is an overwhelming amount of work dedicated to the subject. Only the most relevant work regarding thermo-optic VOAs will be presented. In the prior art, the usual configuration in which the TO effect is exploited consists of depositing a thin metal film on top of a TO material located in or near the propagation path of the light. Light propagation can be affected by injecting a high current density into the thin metal film, which will generate heat through ohmic losses and affect the refractive index of the surrounding material. This is illustrated in Figure 1.1. As shown by the figure, it is crucial to have a heat sink in order for the device to evacuate heat quickly when the VOA is switched to the "off" state. This enables the TO VOA to have a faster response time.

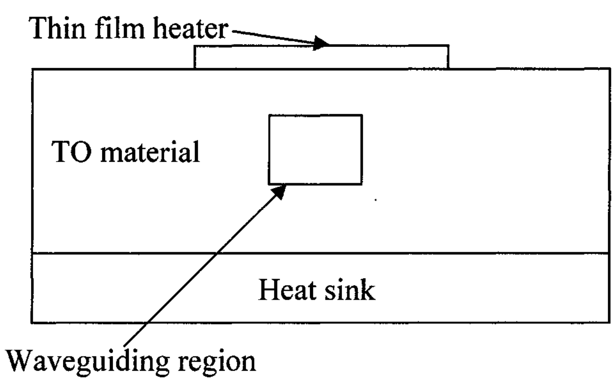

Figure 1.1: Typical TO VOA structure.

In reference [2], TO modulators based on mode cutoff were introduced for the first time even though this effect was well known to be used in conjunction with the EO effect. The structure presented by Sang-Shin Lee is similar to that of figure 1.1, except that the waveguiding region is a polymer rib waveguide. The rib width is made larger in a given region to reduce confinement such that it becomes more prone to the effect of heating. As explained by the author, applying heat reduces the refractive index near the middle of the rib waveguide, which reduces the lateral confinement of the structure. This device has an ER of 20dB with an electrical power consumption of 160mW. The response time was evaluated to be faster than 1.5ms.

In reference [3], a similar structure with an inverted rib waveguide was investigated. The authors claimed that by heating sufficiently they could create an anti-waveguiding region, which could improve the ER of the device as compared to cutoff modulators.

In reference [4], the authors activate a heater above a polymer based waveguide to create an asymmetrical refractive index profile along the vertical axis extending between the thermal source and the heat sink. The optical energy propagating along the core is transversely deflected in the region away from the thermal source. The device is able to achieve an ER of 30dB with 15mW of electrical power and has a rise and fall times of at least 270 s and 1260 s respectively.

It is also possible to create a VOA in conjunction with a Mach-Zehnder (MZ) as shown by Figure 1.2. The light propagating along the waveguide in the figure to the left is split in two beams having equal power propagating in each branch of the MZ. One of the branches of the MZ is influenced by heating which causes a phase difference between the modes supported by both branches of the MZ. The amount of heating power dictates the amount of phase difference induced. At the output of the MZ, both beams combine constructively or destructively according to the induced phase difference. A π-phase difference causes total extinction of the mode while no phase difference results in maximum optical power to flow at the output.

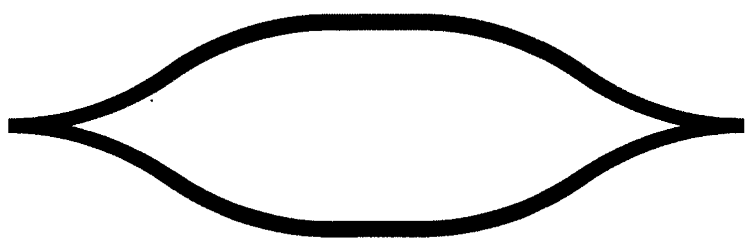

Figure 1.2: Mach-Zehnder configuration.

The MZ configuration operates in a low power regime in comparison to that of the VOAs based on mode cutoff. The most relevant prior art related to VOAs based on the MZ structure is found in reference [5]. The device was able to achieve π-phase difference with only 4.8 mW with a rise and fall time of 9 ms.

Finally, reference [6] uses a novel approach to cause TO switching of an optical waveguide. Essentially a Schottky diode was created on top of a ridge waveguide made of an optically transmissive semiconductor. A ground plane was deposited under the device. The Schottky diode was forward biased and a current was injected between the electrode and the ground plane causing internal Joule heating of the semiconductor. Furthermore, heat is localized to the diode's depletion region. Because of the interesting properties of GaAs and because of internal heating, switching time is as fast as 0.3 μs while power consumption varies between 100mW and 800mW depending if the device attenuates or switches.

Each device above has some performance advantages, but also disadvantages. Mode cutoff VOAs and anti-waveguiding structures consume a lot of electrical power in comparison to MZ VOAs because, unlike the MZ VOA, they must displace the optical mode. Except for reference [6], the prior art had a heat source located some distance away from the optical waveguide. Heat must diffuse towards the waveguide in order to affect it, but this is a time consuming process. Furthermore, heat diffuses away from the heat source; not all the energy is directed towards the waveguide. Therefore, some energy is lost or unused. These losses can be reduced by adding trenches each side of the waveguide to limit lateral heat diffusion, but at the expense of slowing switching time.

On the other hand, in reference [6], the source of heat lies within the waveguiding region and no heat diffusion is necessary before affecting the optical mode. Therefore, switching time is fast. Because internal heating is caused by flow of current between the electrode and ground plane, power is consumed throughout that region, but unfortunately, only a fraction of this power is used effectively in the optical region. For this reason, there is a waste of electrical power.

Most of the prior art is ambient temperature sensitive and would therefore require temperature control. Devices using high thermal conductivity materials will consume a lot of power with a fast switching time and vice versa, but it cannot achieve, both, fast switching time and low power consumption. Finally, device size and manufacturing costs are other concerns of the optics industry.

In addition to introducing a new TO technology, one of the goals is to design a device that is an improvement over some or all the performance parameters as compared to the prior art. The detailed analysis of the performance of the metal optical waveguide will be presented in the next few chapters. Before dealing with the thermo-optic VOA within the plasmon-polariton waveguide, its waveguiding characteristics will be presented in the next chapter.

2. Introduction to metal optical waveguides

In this chapter, a brief history of how the metal optical waveguide came into existence will be presented. Basic notions regarding metal optical waveguide will also be presented. Finally, the mechanism by which the metal optical waveguide can be used as a VOA will be explained.

2.1 Definition of surface plasmon polariton

The propagation of light along a metal optical waveguide is possible due to the existence of surface plasmon-polaritons (SPP). The term "polariton" denotes the coupling of electro-magnetic (EM) fields with macroscopic polar excitations in solids. Surface polaritons may be defined as the coupling of EM radiation to surface dipole excitations, which propagate in a wave-like manner along the interface between two media [7]. Therefore, the surface plasmon-polariton occurs at the interface between plasma, characterized by a negative real permittivity, and a dielectric, which has a positive real permittivity, when a EM wave polarizes the dielectric's surface, disrupts the plasma's surface charge density causing plasma oscillation (or plasmon) and becomes coupled to it.

2.2 Metal permittivity according to Drude's theory of metals

At optical wavelengths, the electromagnetic properties of some metals closely resemble those of an electron gas or, equivalently, cold plasma. The conduction electrons coupled to the EM field influence the permittivity of metals. Under specific conditions, the permittivity of metal may be modeled by the Drude theory of metals according to[8]:

$$\varepsilon(\omega) = \varepsilon' - j\varepsilon'' \tag{2.1}$$

$$\varepsilon' = \varepsilon_r \left(1 - \frac{\omega_p^2}{\upsilon^2 + \omega^2} \right) \tag{2.2}$$

$$\varepsilon'' = \varepsilon_r \left(\frac{\omega_p^2 \upsilon}{\omega(\upsilon^2 + \omega^2)} \right) \tag{2.3}$$

$$\omega_p^2 = \frac{Ne^2}{m\varepsilon_0} \tag{2.4}$$

$$\tau = \frac{1}{\upsilon} = \frac{m_0}{\rho N e^2} \tag{2.5}$$

where ω_p is the plasma frequency, υ is the average electron collision frequency, τ is the relaxation time (or average time between electron collisions), m_0 is the effective mass of the electron, N is the conduction electron density, "e" is the electron charge and ρ is the DC electrical resistivity of the metal. If $\omega^2 + \upsilon^2 < \omega_p^2$, then $\varepsilon' < 0$ and surface plasmon-polariton can be supported by a metal-dielectric interface. The plasma frequency is an important parameter since for lower optical frequency the metal is opaque whereas at higher frequency the metal becomes transparent.

2.3 Surface plasmon-polariton guided by a single interface

The discovery of the metal optical waveguides followed the work of many researchers. Fano and Zenneck were the first to describe a mode guided by the interface between semi-infinite media [9] [10]. Fano modes are found for non-absorbing media, while Zenneck modes are found for absorbing media such as metal. In order for Fano modes to exist, the condition: $|\varepsilon_2| > \varepsilon_1$ and $\varepsilon_2 < 0$ must hold where ε_2 is a collisionless plasma and ε_1 is a lossless dielectric. This is not the case for Zenneck modes. In fact, only a small region of the complex space for ε_2 will not generate solutions. In the case of $|\varepsilon'_2| >> |\varepsilon''_2|$ the Zenneck mode becomes almost a purely radiative mode, that is, a Brewster wave [11].

It is only after Otto, Kretschmann and Raether [12] introduced attenuated total reflection (ATR) by which a prism is used to effectively couple the bulk EM wave to the surface EM wave supported by an interface, that significant researching effort was devoted to SPP. The interest in SPP modes was spawned by its highly localized fields near interfaces, which make them particularly sensitive to any irregularities near those interfaces. Hence, this property, along with information provided by ATR, constitutes a powerful investigative tool to determine the properties and quality of interfaces and thin films.

2.4 Surface plasmon-polariton guided by a thin metal film slab

In practice, thin metal films bounded by semi-infinite media are used instead of single metal-dielectric interfaces since some of the modes supported by the thin metal film structure exhibit lower losses than those supported by a single metal-dielectric interface. The most relevant work regarding this structure was conducted by Burke, Stegeman and Tamir [14]. Their work presents the numerous modes supported by this structure based on the fact that a purely non-magnetic thin metal film slab can only support transverse magnetic (TM) modes [7]. This makes thin metal films useful in polarizing applications. For the case where the metal thickness is much greater than the classical skin depth, the solutions are decoupled SPP propagating at each interface, which very much resembles the solutions found for the semi-infinite metal-dielectric interface. When the metal film is thin enough, the SPP modes guided by each interface become coupled by field tunneling through the metal, thus creating supermodes that exhibit dispersion with metal thickness

In some instance of the structure, the substrate's and superstrate's refractive indices were matched making a symmetrical structure and, in another instance, they were mismatched. For a symmetric structure, a symmetric bound (s_b) mode and an asymmetric bound (a_b) mode can be found as shown in Figure 5.2 where their phase (β) and attenuation (α) constants are plotted as a function of film thickness. For the asymmetric structure, the s_b, a_b, symmetric leaky (s_L), and asymmetric leaky (a_L) modes can be found as shown in Figures 5.3 and 5.4 where their propagation and attenuation constants are plotted as a function of metal film thickness. The term "bound" and "leaky" indicate that the mode is non-radiative and radiative respectively. The nomenclature comes from the particular field distribution found for each mode. The symmetric mode comes from the fact that the transverse electric field present in the slab structure does not exhibit a phase reversal within the metal. Conversely, we refer to the asymmetric mode when the transverse electric field suffers a 180°-phase reversal within the metal. An example of the field distribution of a symmetric mode in a symmetric structure is the E_z field (see details in chapter 5) of the s_b mode illustrated in Figure 5.11 and indicated as curve "a". The propagation loss of the s_b mode diminishes as the metal thickness is reduced in opposition to that of the a_b mode. This is true for the symmetric and asymmetric structure as shown in Figure 5.2 and 5.4 (a). This occurs because, for the s_b mode, the field confinement within the lossy metal is reduced while it increases for the a_b mode. For this reason, the s_b mode is often called "long-ranged" while the a_b mode is short-ranged. When one designs a waveguide, a tradeoff has to be made between propagation loss and confinement. A similar situation occurs for the s_L mode except that, as the metal thickness is reduced, radiative losses become dominant. This is shown by comparing Figure 5.6 curve "a" and D.2 because the main difference between these two modes is radiation. For the a_L mode the confinement increases as metal thickness is reduced, therefore the radiative losses remain small compared to the losses incurred within the metal.

An important difference between the symmetric and asymmetric structure is that the s_b mode of the asymmetric structure exhibits a cutoff thickness while it does not for the symmetric structure, which can be observed by comparing Figure 5.2 and 5.4. Instead, beyond the cutoff thickness of the s_b mode, a growing wave exists where more power is provided than dissipated; therefore, the wave grows in amplitude along the structure [14]. This mode can only exist, if power is provided along the whole length of the device. The asymmetric modes do not change in character as the film thickness is reduced except for a change of confinement, attenuation and phase constants. This is not the case for the symmetric modes, which evolves slowly towards the TEM mode supported by the background material. Finally, these authors suggest "end-fire excitation", different from the ATR, as a new way to couple light to the SPP supported by the metal slab structure.

2.5 Surface plasmon polariton guided by thin metal film of finite width

2.5.1 Theoretical review

Thin metal film slabs are of limited practical interest since they offer 1D field confinement only in the transverse plane and losses remain high for all metals at communications wavelengths. Two-dimensional optical confinement in the transverse plane can be achieved by a thin metal film of finite width, which is commonly named a plasmon-polariton waveguide. Such a structure does not support pure TM modes; instead, all six field components are present. The plasmon-polariton waveguides were analyzed in a symmetric and asymmetric structure for various metal thicknesses and widths [15], [16], [17]. The author makes a detailed analysis of the modes supported by the various waveguide structures and presents results through graphs. The reader is strongly advised to read these publications in order to properly comprehend the remaining of section 2.5.1 since it summarizes their results and graphs. Four fundamental bound modes were found for this structure: aa_b^0, sa_b^0, as_b^0 and ss_b^0. Leaky modes also exist, but they have yet to be investigated in detail. The nomenclature is an extension of the thin metal film slab's nomenclature where the additional letter indicates the symmetry or asymmetry of the main transverse electric field component along the width of the waveguide. The subscript indicates whether the mode is bound or leaky while the superscript denotes the number of extrema of the field component along the width of the waveguide. All bound modes supported by the symmetric structure except aa_b^m, sa_b^m and ss_b^0 have a cutoff thickness where m>0 indicates higher order modes. In addition to exhibiting dispersion as a function of metal thickness, the modes also exhibit dispersion as a function of width. Furthermore, the finite width metal waveguide has a cutoff width in addition to a cutoff thickness. The general trend of these modes is that the attenuation constant increases with vanishing thickness for the aa_b^m and sa_b^m modes while it reduces for the ss_b^m and as_b^m. In particular, the ss_b^0 mode tends towards the TEM mode supported by the background materials as the metal film vanishes. This is the main mode of interest in these waveguides.

An asymmetric structure has a more complex behavior where it is possible that the ss_b^0 mode (and possibly other modes) becomes asymmetric-like with decreasing metal thickness. However, if this is not the case, then, the ss_b^0 will exhibit a cutoff thickness that was not present in the symmetric structure. Further detail is given in [15]. In any case, for a very thin metal waveguide in an asymmetric structure, the ss_b^0 either does not exist or exhibits too high propagation loss to be able to propagate a useful distance.

In a symmetric structure, the ss_b^0 mode is one of the most useful modes for practical purposes since, for thin enough metal film, it can propagate a useful distance. In addition, it is the only long-ranged bound mode, which does not exhibit cutoff in a symmetric structure. In fact, it is possible to design and excite the waveguide in such a way that virtually only the fundamental ss_b^0 mode propagates, which eliminates problems related to multimode waveguiding. In addition, it was shown that the ss_b^0 mode supported by a thin metal waveguide in a symmetric structure had a Gaussian-like intensity distribution suitable for end-fire excitation [15]. With careful design, this mode can be coupled to a SMF or polarization maintaining fiber (PMF) with minimal coupling loss.

2.5.2 Experimental review

Recently, the plasmon-polariton waveguides were examined experimentally for the first time [18], [19], [20]. Basic structures such as straight waveguides, tapers, Y-junctions, couplers, bends and MZs were investigated for different widths. End-fire excitation was proven to couple light effectively to the waveguide. Plasmon-polariton waveguides with large aspect ratios w/t>>1, where "w" and "t" are the width and thickness of the waveguide respectively, were shown to have high PDL as suggested by purely TM modes supported by thin film slabs. For aspect ratios near unity such as a square waveguide, the waveguide is shown theoretically to be insensitive to the input polarization of the optical source [21].

Consequently, for large aspect ratio metal optical waveguides, it is critical that the input polarization of the optical source be perpendicular to the deposition plane of the metal layer, if the plasmon-polariton wave is to propagate a useful distance. In the context of the telecommunications industry, large aspect ratio metal optical waveguides may only find applications near the transmitting end of an optical network where light is polarized. As light propagates through the network, it becomes arbitrarily polarized and is not suitable for large aspect ratio metal optical waveguides. Because the TO VOA presented in this work is made of a large aspect ratio metal optical waveguide, it would need to be placed near an optical transmitter.

2.6 Mechanism from which VOA functionality is possible

As was suggested by this chapter, it is possible to cutoff a mode supported by the waveguide simply by introducing a refractive index asymmetry whether in a slab structure or finite width waveguide. The input power would then be transferred to the other existing modes, which are much lossier. A careful design could use the ss_b^0 mode such that, when it is heated, it becomes asymmetric-like as proven by comparing results from reference [15] and [16]. This would cause the attenuation constant to increase dramatically, which is useful in the context of VOAs.

There are other means by which heating can cutoff the modes supported by the waveguide. Reducing the refractive index near the waveguide is one of them. It causes the waveguide's confinement to be reduced [20], causes more optical power to radiate and couples to cladding modes. However, in this work, mode cutoff was achieved by introducing a refractive index assymetry.

3. Experimentation

In this chapter, the TO VOA will be designed, built and its thermal, electrical and optical behavior will be investigated experimentally. In section 3.1, the TO VOA's design will be explained. Section 3.2 discusses the setup to stabilize the temperature of the sample. The waveguide is also characterized electrically and calibrated for use as a temperature sensor. In section 3.3 current is injected through the waveguide and the temperature increase is measured. Waveguide degradation due to electromigration and electrostatic discharge (ESD) is also investigated. Finally, in section 3.4, the waveguide is characterized optically. The IL, ER, mode field diameter (MFD) and response time are measured.

3.1 Description of waveguide structure and method of fabrication

3.1.1 Design of the structure

The finite width metal optical waveguide is designed to exploit the basic properties introduced in the previous chapter. Essentially, the waveguide is heated due to its ohmic losses when a high current density is injected through it, which introduces an asymmetric refractive index profile that induces cutoff of the mode supported by the waveguide. First, the design of the waveguide structure will be explained from a thermal and optical perspective.

A refractive index asymmetry can be easily achieved between the upper and lower claddings when the sample is heated, if the claddings' TOCs are of opposite polarity. It is also important that the amplitude of at least one of the TOCs be large to minimize electrical power consumption. Silica, a standard optical material, and an optical polymer were chosen. Silica has a small positive TOC while the polymer has large negative TOC.

Silica having a higher thermal conductivity was placed between the heat source and heat sink rather than polymer because it enables faster response time of the device, but at the expense of electrical power consumption [22]. The "electrical power consumption" performance parameter is considered to be of less importance than that of the response time because it is already known that the heat source will affect light efficiently within this particular structure (more on this next).

Heat comes from the metal optical waveguide due to ohmic losses when a current is injected through it. The maximum temperature of the waveguide is at its core and reduces with distance from it, as does the electric field intensity, due to the optical excitation. For this reason, it is expected that heat affects the optical mode efficiently and electrical power is conserved.

Gold was chosen as the metal forming the waveguide for the following reasons. Gold, a noble metal, is very chemically stable as it does not oxidize or tarnish as does other metals. Its permittivity can be described by Drude's model. In addition, its use as a metal optical waveguide is known to produce low propagation losses as compared to most other metals [20].

The distance separating the heat sink and heat source also affects power consumption and response time of the device. Thermal investigation shows that reducing the thickness of the top cladding slightly increases the device's response time and reduces its power consumption [22]. These results are based on the assumption that the device lies within air, a good thermal insulator. However, it is important that the claddings be thick enough to not perturb the modes supported by the waveguide. In such a case, the fields are negligible when they reach the edge of the claddings. It was determined theoretically and reinforced with experimentation that claddings 15μm thick or more would be sufficient for normal operation of the waveguide [23]. For this reason, the lower cladding, silica, is set to 15μm. Given the way that polymer was deposited on top of the waveguide, we did not have as much control over its thickness (more on this later).

The heat sink is simply a large high thermal conductivity material with a large surface exposed to its surroundings such that heat can be exchanged easily. Wafers on which are built optical devices are typically made of silicon, a material with high thermal conductivity. It will be shown in chapter 5, in the context of TO VOAs that silicon was not a good choice from an optical perspective because its refractive index is not matched to silica.

In summary, we have committed ourselves to silica, polymer, silicon and gold as the the claddings, heat sink and metal core respectively. Furthermore, the claddings are at least 15μm thick. The device is assumed to lie within the air. The device incorporating these materials is constructed in the next section and is shown in Figure 3.1.

3.1.2 Construction of the structure

The TO VOA structure presented in Figure 3.1 was constructed. In order to construct this structure, wafers from Silicon Quest International having a 15µm layer of thermally grow silica on top of 600µm silicon were used. The metal deposition was provided from Carleton University. A mask was designed to pattern pure gold onto the thermal oxide.

Because gold does not adhere well on silicon dioxide, a thin adhesion layer of Molybdenum a few Ångstroms thick was first deposited onto the thermal oxide. As will be shown in chapter 5, the modes supported by the waveguide structure have fields that are large near the metal-dielectric interface. Therefore, it can be expected that the supported modes will be especially sensitive to the material property near the interface. It is known from simulations that Molybdenum as the waveguide's core will produce higher propagation losses than that of gold. It was determined that a very small adhesion layer, much thinner than the gold thin film, will still have a noticeable impact on the total propagation loss. However, a few Angstom thick of Molybdenum, a few atoms thick, will undeniably be an uncontinous film making it much more difficult to model or determine its experimental impact. In addition, there may be the presence of a cermet layer. As a first approximation, the adhesion and cermet layer will be neglected in the optical model shown in chapter 5.

A 20 nm layer of gold was then deposited. The metal was patterned by removing it in predetermined regions according to the mask in a lift-off lithography process. Waveguides of 4, 6 and 8 microns wide were patterned along with arms extending perpendicular to the waveguide on the thermal oxide as shown in Figure 3.1. It is known from optical simulations [24] that the coupling loss to PMF for the 8µm wide waveguide is lower than that of the other waveguide widths; therefore, the 4 and 6 µm wide waveguide had tapers at their input and output in order to reduce the coupling loss. Figure 3.2 is a cross-sectional view of Figure 3.1, taken away from the pads.

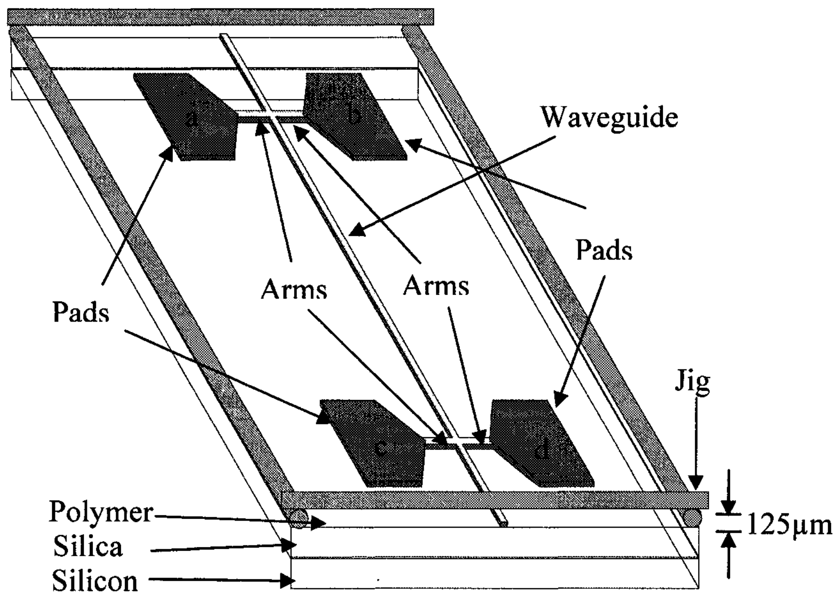

Figure 3.1: Isometric view of the waveguide structure.

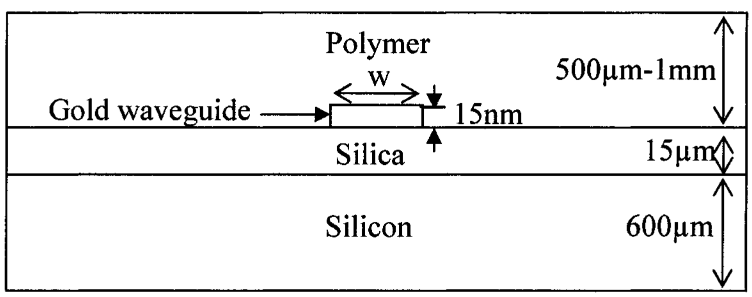

Figure 3.2: Cross-sectional view of the waveguide structure.

Subsequently, samples were sent to Surface Science Western for a line profile measurement using atomic force microscopy (AFM) and it was determined that the gold thickness was in fact 15 nm as shown in Figures 3.3 and 3.4. The line profile measurement was done on two samples, X014604.13 and X014604.14, where the 8μm wide waveguide was deposited. The sample names will be referred as .13 and .14 henceforth. On sample .13 and .14 the width of the metal waveguide was measured to be 8.1μm and 8μm respectively. The metal thickness of both samples was measured to be the same, 15nm, which is significantly different from the expected value of 20nm.

XO14604.13

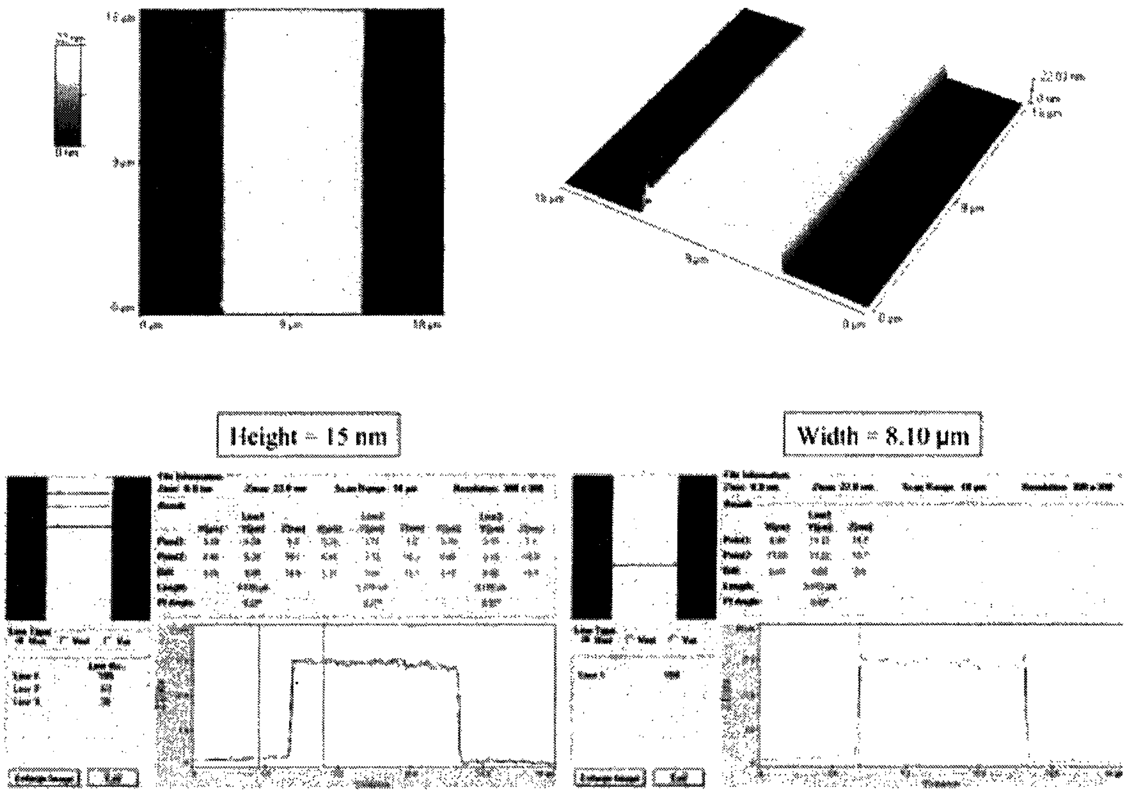

Figure 3.3: Line profile measurements using AFM of sample .13.

One of the purposes of the arms of the waveguide is to connect the contact pads to the waveguide electrically. The arms are made of gold and are of the same width and thickness as that of the waveguide. The pads are made of a 0.5µm thick aluminum layer since they must be robust enough to accommodate metal probe, henceforth named electrodes, which will deliver the current to the waveguide. Because the pads are made of metal, they can technically support a plasmon-polariton mode and interact with that of the waveguide. This is unwanted and this is the reason why the main role of the arms is to bring the pads further from the waveguide to minimize optical interaction. It is known that most of the power of the fundamental modes supported by the waveguide is contained within a radius of 15-20µm [23]. For this reason, the closest part of the pads is at a least 20 µm away from the waveguide. Furthermore, the pads are also tapered as it reaches the arms of the waveguide. The large rectangular region of the pads being 150µm x 100µm is convenient because it is difficult to insert an electrode very precisely even with the help of micro-positionners.

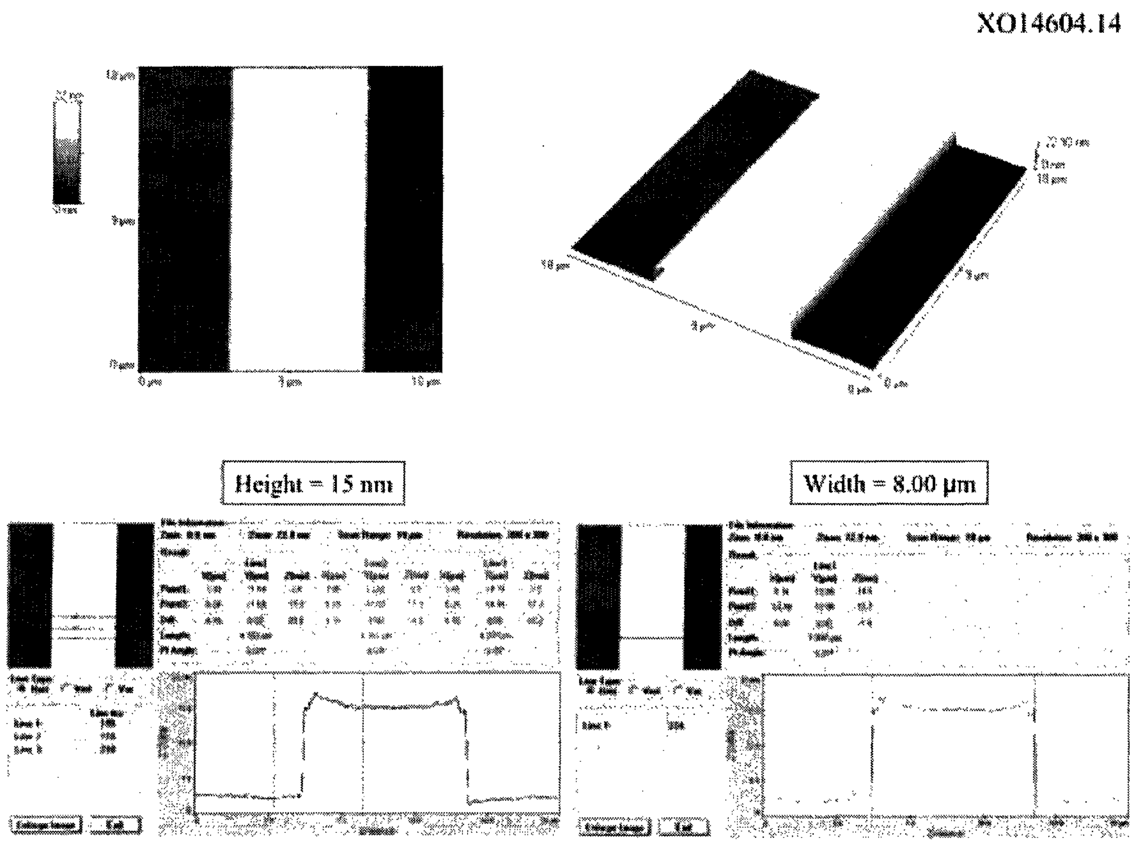

Figure 3.4: Line profile measurements using AFM of sample .14.

It is well known that metals may degrade from electromigration (to be discussed in a later section) when a large current density is passed through [25]. For this reason, the whole waveguide including its arms can be seen as a fuse in such conditions. Because we need the waveguide to be heated through ohmic losses, it is important that it cannot sustain as much current as the sum of the currents flowing through pad "a" and "b" or "c" and "d" as shown in Figure 3.1. Arms on each side of the waveguide, in total, can carry twice as much current as the waveguide; therefore, if current is injected from pad "a" to "c" and "b" to "d", the waveguide is most likely to be destroyed due to electromigration before the arms. For the same reason, most of the heating will occur in the waveguide rather than its arms. However, while testing the device in the laboratory, it was noted that it was difficult to insert all four electrodes appropriately on the pads and conduct a full series of experiments without damaging the waveguides. For this reason, to increase the probability that the experiments would be conducted successfully, only two pads were used. For the same reason, resistance measurements will only use two pads. The purpose for making resistance measurements will be explained later.

The sample was cleaved perpendicular to the longitudinal direction of the waveguide to the desired length, which includes at least a few pads to be able to inject current into the waveguide. A picture of the real device was taken and its top view is shown in Figure 3.5.

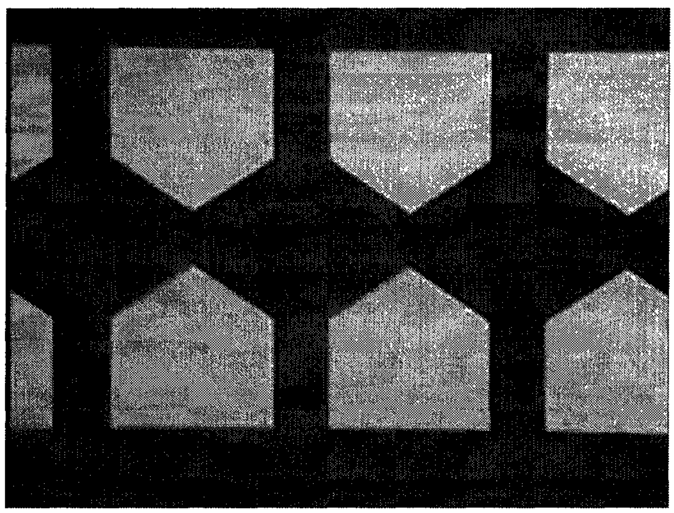

Figure 3.5: Picture of the the waveguide with pads: Top view.

Finally, Nye optical curing gel (OCK-433) was deposited on top of the waveguide to form the upper cladding. The gel addresses an issue. As most gels would behave, it is possible to poke through it. Hence, this eliminates a few steps in the lithography process; we do not need to etch a hole to be able to reach the pads as would be required with the use of solid materials. On the other hand, the optical curing gel introduces another problem, but it can be solved rather easily. Essentially, the gel is composed of two liquids that cure when mixed together. As is expected from surface tension of liquids, the shape of the gel covering the waveguide is not flat; it looks elliptical in shape. In fact, there is a serious concern regarding the gel's ability to cover the waveguide at its ends. It is important that the material covering and supporting the waveguide be vertically flat at the edge of the sample, otherwise, it would cause undesired effects. A solution to this problem is to put a jig on top of the edges of the sample as shown in Figure 3.1. The jig is constructed from fibers that were stripped down. As seen from the figure at the input and output of the waveguide, there is a 125μm gap between the edge of the sample and the fiber. As the curing gel is poured into the jig, it fills the 125μm gap and the surface tension between the edge of the sample and fiber causes the gel to be almost vertically flat. On the other hand, there is still an elliptical shape on top of the sample. However, this will have a negligible impact on the experimental results for the purpose of this thesis because the gel is very thick. Another role of the jig is to prevent the gel from spilling outside of the sample during the curing process.

The thickness of the gel layer was measured by using a micro-positionner and an electrode. The position of the electrode was recorded when it touched the top of the gel in the middle of the sample. Subsequently, the electrode was poked into the gel until it touched the silica and a second position was recorded. The difference in positions gave us the gel thickness. There was a high variability from sample to sample. We determined that the gel thickness varied between 500-1000μm.

The material properties constituting the waveguide structure is as follows. Silica has a refractive index of $1.4457 \pm 4*10^{-4}$ measured with a Metricon at 1548 nm and room temperature (near 23°C). The other parameters were determined from typical values from the literature. The thermal conductivity is assumed to be $1.1 \frac{W}{m.K}$ [26] and the TOC is $10.75*10^{-6}$ $(°C)^{-1}$ [1]. The properties of silicon also come from the literature. The refractive index is assumed to be 3.475 [1] with a TOC of $1.818*10^{-4}$ [1] and thermal conductivity of $145 \frac{W}{m.K}$ [27]. The thin gold film properties where obtained from the literature in similar conditions than our structure. The refractive index was assumed to be 0.55-1i*11.5 [1] (bulk value) with thermal conductivity $30 \frac{W}{m.K}$ [28] and electrical conductivity $1*10^{7}$ $(\Omega m)^{-1}$ obtained from the measurements in chapter 5. Those are thin film values, which are different from the typical bulk values. The refractive index of the polymer is 1.4469 [29] at room temperature with a TOC of $-1.3*10^{-4}$ and thermal conductivity of $0.14 \frac{W}{m.K}$ [30]. The refractive index of the silica and polymer can be matched by increasing the temperature of the whole device uniformly with the use of a thermo-electric cooler/heater (TEC).

3.2 Sample preparation for experiments

3.2.1 Sample setup for temperature stabilization

As explained earlier, we want to induce cutoff of the modes supported by the waveguide when a current is injected through it. One the other hand, we wish to have maximum output optical power when no current is injected. This occurs when polymer and silica are matched. As we know, the polymer and silica have very different TOCs, which means that, at a given ambient temperature, the claddings may be matched, but not at another temperature. Devices on the market are required to operate in a large a range of ambient temperature; therefore, for our design to meet those requirements, it is necessary that the sample temperature be stabilized. This can be done by using a thermo-electric cooler/heater (TEC). Unfortunately, temperature stabilization involves more power consumption and extra cost. This is a disadvantage for our particular structure. Other designs could eliminate this problem, but this is not one of the goals of this thesis.

Once the sample was constructed, it was placed on top and in the middle of a thermo-electric heater/cooler (TEC), which is used to heat or cool the sample in order to match the refractive indices of the silica and polymer. To control the temperature, a current is injected through the leads of the TEC. The direction of the current flow dictates if a given side of the TEC will heat or cool. A silver based thermally conductive compound was used at the interface between the sample and the TEC to minimize the thermal contact resistance. The sample was pressed firmly on the TEC and wiggled to make sure the thermal compound would spread uniformly under the sample. A thermistor was also placed and fixed on top of the TEC near the sample via a thermally conductive epoxy. The temperature on top of the TEC could then be determined by using the Steinhart-Hart relation:

$$\frac{1}{T} = A + B * \ln R + C * (\ln R)^3 \tag{3.1}$$

where T and R are the temperature in degree Kelvin and resistance in ohms respectively. The parameters A, B and C are dependent on the specific thermistor used. The thermistor that was used in the experiments had the following parameters: $A=9.6542*10^{-4}$, $B=2.3356*10^{-4}$ and $C=7.7781*10^{-8}$ and these parameters are valid between 0 and 69°C. The leads of the TEC and thermistor were connected to a TEC controller. Essentially, a feedback loop was created and the TEC controller was able to dynamically control/stabilize the temperature of the device to a desired value. Also, the TEC controller through the Steinhart-Hart equation calculated and displayed the temperature detected on the top of the TEC.

3.2.2 Waveguide calibration as a temperature sensor

In addition to determining the temperature on top of the TEC, it is also useful to know the temperature of the waveguide when it is heated by injecting a current through it because, from this, we can determine the induced refractive index asymmetry that may cutoff the mode supported by the waveguide. Unfortunately, heating the waveguide does not generate a uniform temperature distribution throughout space and cannot be determined from the thermistor. In such a situation, we would think that the most accurate temperature measurement occurs when a thermal probe, such as a thermo-couple, is placed closest to the waveguide. Because the thermo-couple is large in comparison to the dimensions of the waveguide, placing it close to the waveguide would perturb the optical mode, the temperature distribution and render the temperature measurement inaccurate. Another approach was considered.

It is well known that the resistivity or resistance of a metals changes with temperature. Near room temperature, resistance or resistivity varies linearly as a function of temperature [32]. Conversely, it is possible to determine the temperature knowing the resistivity or resistance of a metal given a calibration. The core of the waveguide is a metal, therefore, it can itself be a temperature sensor; the need for a thermal probe is eliminated. The same electrodes that are connected to the pads to inject current can be used to measure the resistance of the waveguide and determine the temperature.

It is quite simple to calibrate the waveguide as a temperature sensor. A given length and width of waveguide is selected for resistance measurement, the resistance is measured and the temperature of the waveguide is noted. With the exact same electrode connection, these measurements are accomplished for various temperatures of the device until the temperature range of interest is covered. The temperature at the waveguide level is determined from the temperature measurement of the thermistor on top of the TEC given the assumption that they are the same when the waveguide is not heated. This is proven true in Appendix A. In this manner, we can proceed with a non-invasive and accurate temperature measurement.

The resistance measurement was done by injecting a 100μA current into the waveguides. We determined experimentally that such a small current does not produce enough heat to influence the electrical and optical characteristics of the metal optical waveguide structure. Furthermore, to eliminate the resistance of the wires from the measurements we can use a four-point probe. Typically, two of the electrodes are connected directly to one pad while the other two are connected to another pad; this constitutes the four point probe. However, in practice I failed multiple times to introduce four probes on two pads since, each time, either a probe accidentally scratched the waveguide or the effect of elecstrostatic dischard destroyed it even if I was grounded (something that I still don't understand to this day). Given the limited number of samples available for the experiments, a less risky configuration was used instead: the four-point probe connections were made at the end of the two micro-positionners where the input of the electrode is attached. Using this particular configuration, only two electrodes are inserted onto the pads. Unfortunately, this modified setup does not eliminate the resistance of the electrode and its contact resistance with the pad. However, by plotting the resistance of a waveguide as a function of length, it is possible to extrapolate this linear relationship to obtain a value at its ordinate. The value found at the y-ordinate represents the total resistance of the electrodes including the contact resistance with the pads. This value is subtracted from the results to obtain the true resistance of the waveguide.

For each waveguide width, resistance measurements were made over the temperature range of interest for a few waveguide lengths. The results are shown in Figures 3.6 and 3.7.

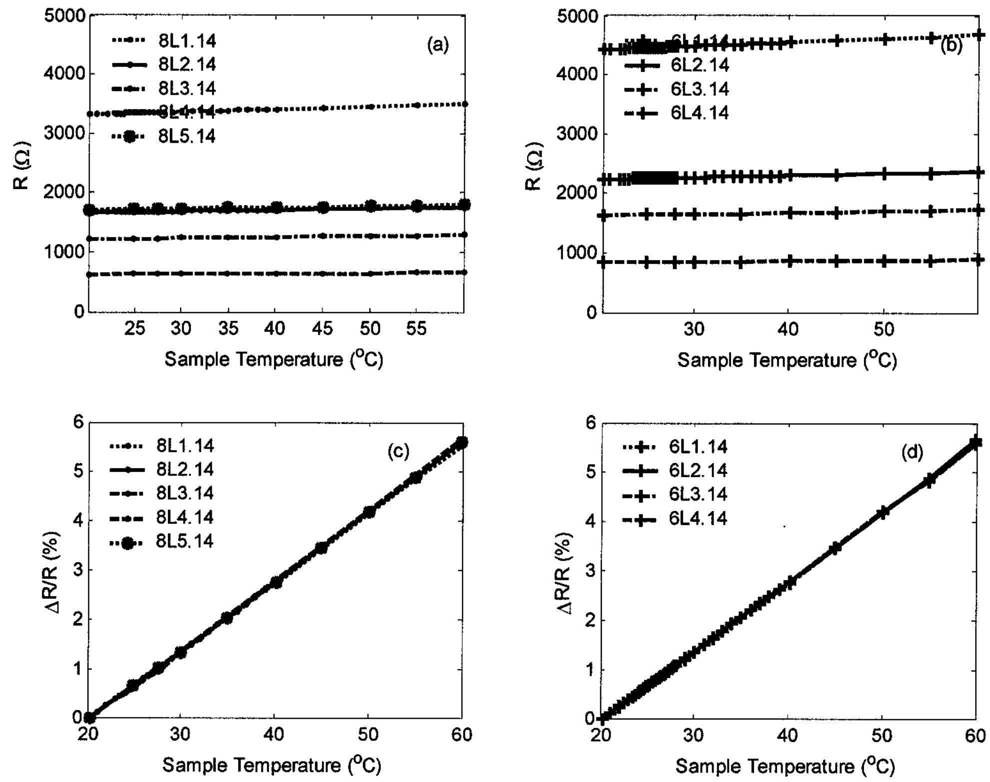

Figure 3.6: Temperature calibration of waveguide on sample .14. (a) and (b) show the resistance versus temperature of the TEC for the 8 and 6μm wide waveguide respectively for various waveguide lengths. (c) and (d) show the percentage of variation of resistance of the 8 and 6μm wide waveguide respectively for various waveguide lengths when the sample is heated from the TEC. In the legend, the first number indicates the waveguide width in microns. L1, L2, L3 and L4 are the lengths of the metal waveguide between the pads. L1=4440μm, L2=2240μm, L3=1640μm, L4=840μm and L5=2290μm. Resistance is shown to be a linear function of temperature.

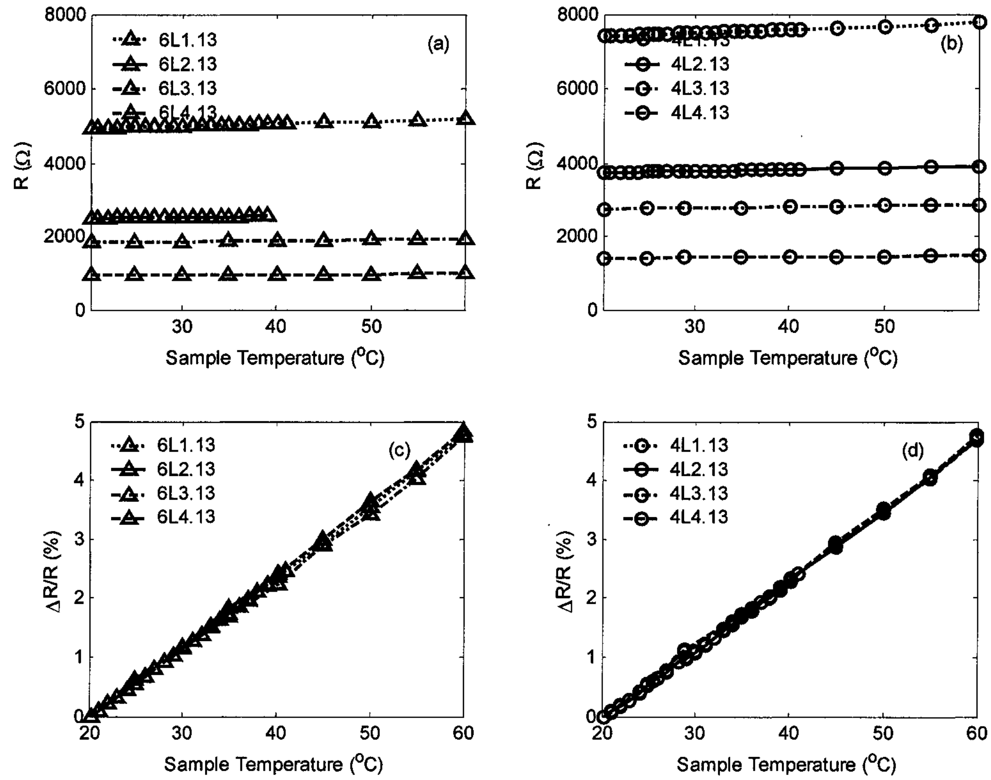

Figure 3.7: Temperature calibration of waveguide on sample .13. (a) and (b) show the resistance versus temperature of the TEC for the 6 and 4μm wide waveguide respectively for various waveguide lengths. (c) and (d) show the percentage of variation of resistance of the 6 and 4μm wide waveguide respectively for various waveguide lengths when the sample is heated from the TEC. In the legend, the first number indicates the waveguide width in microns. L1, L2, L3 and L4 are the lengths of the metal waveguide between the pads. L1=4440μm, L2=2240μm, L3=1640μm, L4=840μm. Resistance is shown to be a linear function of temperature.

Because the resistance versus temperature is a linear relationship, we can fit a linear model through the experimental data using a least square method.

$$R = mT + b \tag{3.2}$$

where "m" and "b" are coefficients to be determined by fitting the curve through the above data. R and T are the resistance and temperature in Ω and °C respectively. Now that the waveguides have been calibrated for some selected lengths and widths, we can introduce a current through the waveguides, heat them via ohmic losses and monitor the temperature using changes in resistances. The heat produced by the ohmic losses will change the resistance of the waveguide in a similar way that the TEC achieved it. Because the thermal conductivity of the metal is much higher than that of the polymer or silica, the temperature will be rather uniform inside the metal. Because the waveguide is now calibrated, it is easy to determine the average temperature increase inside the metal due to the injection of current.

In addition to calibrating the waveguide as a temperature sensor, we can determine the resistivity of the thin gold film knowing the resistance and the cross-sectional area of the waveguide. The thin film resistivity differs from the bulk resistivity.

The resistance of a bulk homogeneous isotropic rectangular material is defined by the following equation:

$$R = \frac{\rho L}{wT} \tag{3.3}$$

where R, ρ, L, w and T is the resistance, resistivity, length, width and thickness of the material respectively. ρ is itself represented by the following equation:

$$\rho = \frac{m}{Ne^2\tau} \tag{3.4}$$

where m, N, e, τ is the effective mass of the electron, the number of electrons per unit volume, the electric charge and the relaxation time[8]. These equations do not apply to thin films because many microscopic effects become significant. However, Equation (3.3) may be used in conjunction with an effective resistivity where the microscopic effects are considered.

Modeling the resistivity as a function of microscopic phenomena can become quite complex. The effective resistivity of a thin film is higher than the one from bulk materials in part because, in a thin film, the thickness of the waveguide can be comparable to or less than the mean free path of the electron. The electrons are only mobile within the waveguide; therefore, collisions at the interface between the metal and dielectric must occur. For thin films, this phenomenon can be significant, while for bulk materials the internal collisions are dominant [31]. The effective relaxation time or mean free path in a thin film is therefore seen to be reduced which implies, according to Equation (3.4), that the resistivity is increased. Grain size of the metal can influence its resistivity. The surface roughness of the metal has also a small impact on the resistivity.

The resistivity of metals is known to increase with temperature. For a small range of temperature near 20°C, the resistivity can be assumed to vary linearly according to

$$\rho_T = \rho_0[1 + \delta(T - T_0)] \tag{3.5}$$

where ρ_T, ρ_0 and δ are the resistivity at the temperature T, the resistivity at the standard temperature T_0 and the temperature coefficient of resistivity for the particular metal, respectively [32]. It follows that resistance will also vary linearly in those conditions.

Figure 3.8 represents the resistivity of the gold metal as a function of sample temperature determined from waveguides of various widths and lengths.

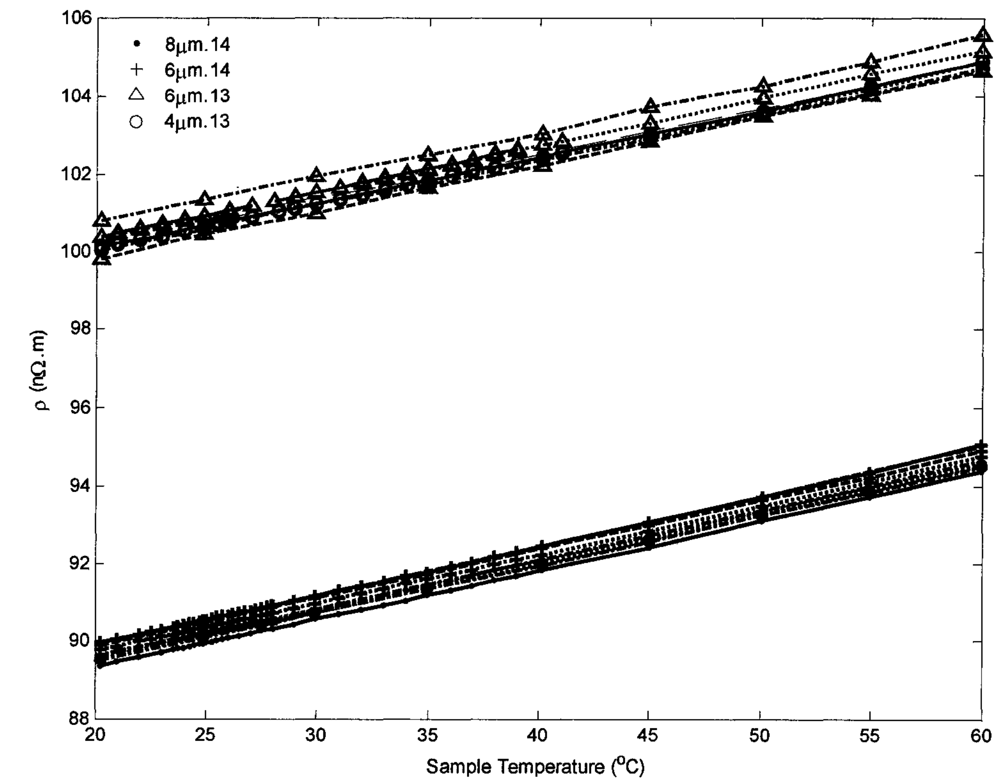

Figure 3.8: Resistivity of gold as a function of temperature.

Notice the significant difference in resistivity from sample .13 and .14. The difference in resistivity is probably due to the different deposition conditions. De-embedding errors from the contact and electrode resistance is not significant enough to account for the discrepancy. Although the thickness of all waveguides is 15nm, the width of the 4μm and 6μm wide waveguide was not measured using AFM. The results shown in Figure 3.8 are based on the assumed widths.

Based on equation (3.5), we determined δ for thin films. We obtained $1.4*10^{-3}(°C)^{-1}$ for the .14 sample and $1.2*10^{-3}(°C)^{-1}$ for the .13 sample.

3.3 Electrical and thermal characterization of waveguide

3.3.1 Effect of current on resistance and temperature of waveguide

Resistance was measured as a function of injected current through the waveguide and results are illustrated in Figure 3.9. Figure 3.9 (a) shows the percentage variation of resistance as a function of applied power density for a few waveguide widths and lengths. The relationship between power density and current density is shown in Figure 3.9 (b). The relationship between power density and power per unit length is shown in Figure 3.9 (d).

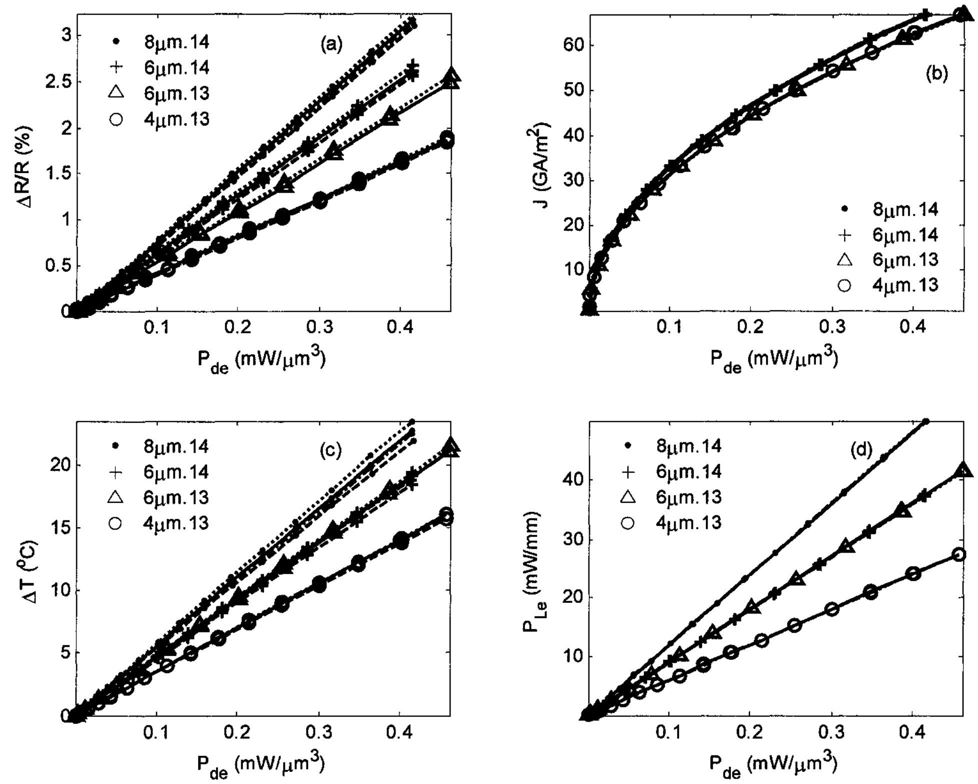

Figure 3.9: Temperature increase of waveguide from injection of current. a) represents the percentage of variation in resistance as a function of applied power density for various waveguide lengths and widths. The relationship between current density and power density is shown in Figure b). Figure c) shows the increase in waveguide temperature as a function of the applied power density. Figure d) shows the electrical power per unit length dissipated for known cross-sections of the metal waveguide as a function of power density.

From the theory of thermo-dynamics, we know that the temperature increase of the waveguide is directly related to the input power in the form of heat. In fact, it appears linear as shown by Figure 3.9 (c). The heat generation due to ohmic losses is of the form $P=RI^2$, consequently it follows that the temperature increase as a function of current is of the second order. A curve can be fitted to the experimental data through an equation that takes the following form:

$$R = n\ P_{de} + c \tag{3.6}$$

where "n" and "c" are coefficients to be determined by fitting the curve to the experimental data. "R" and "P_{de}" are the resistance and electrical power density applied to the waveguide respectively. The experimental data for Equation (3.6) is found by measuring the resistance as a function of the injected current into the waveguide. Except for the second order behavior explained above, there is no particular reason why Equation (3.6) should take that form. We are merely trying to find a simple equation that closely fits the data points. By equating Equation (3.2) and (3.6) and isolating the temperature, it is possible to find the temperature of the waveguide for an applied power density (or current density). To find the temperature increase due to the applied power density into the waveguide, the following relationship is useful:

$$\Delta T = \frac{n P_{de} + c - b}{m} - \mathrm{To} \tag{3.7}$$

where "n" and "c" were found from Equation (3.6) while "m" and "b" were found from Equation (3.2). ΔT and T_o are the variation of temperature due to injected electrical power density and the TEC temperature respectively. From Equation (3.7), the temperature increase is plotted as a function of electrical power density, as shown in Figure 3.9 (c), for different waveguide widths and lengths. Essentially, Figure 3.9 (c) shows that, for the same applied power density, a wider waveguide will provide more temperature rise than a narrower one. This is also the reason why, for the same power density, the percentage of variation of resistance for the wider waveguide is larger than that of the narrower one. It is important to reiterate that Equation (3.7) is an average temperature increase because the temperature in the waveguide is almost but not quite uniform.

Power density is useful to compare waveguides of different geometry, but in the end, we want to know how much a given waveguide structure will consume power. For this reason, rather than expressing results as a function of power density, they can be expressed as a function of the electrical power consumption per unit length considering the cross-sectional area of each metal waveguide. For this purpose, Figure 3.9 (d) shows the power per unit length as a function of power density for all waveguide geometries. The figure shows that, for the same power density, a wider waveguide will consume more electrical power per unit length than a narrower one.

3.3.2 Electrical phenomena degrading waveguide: electromigration and electrostatic discharge

A scheme was devised to cutoff the mode supported by the waveguide by introducing a refractive index asymmetry by heating the metal waveguide through ohmic losses when a current was injected through it. However, based on the high current density required to heat the waveguide sufficiently to have a significant optical impact, we recognize a potential problem. The current density injected through the metal may be so high that it may suffer degradation. For gold metal, the current density threshold at which degradation (or a change of morphology) occurs is as low as 9 GA/m^2-70 GA/m^2 [25]. The degradation process is named electromigration. Electromigration occurs when the heavy positive ions constituting the metal are displaced due to the strong electron-wind colliding on them when a high current density is applied.

In a polycrystalline metal such as in the case of our metal waveguide, the electromigration mechanism occurs predominantly through the migration of ions along the grain boundaries [33]. Unfortunately, the size of grain boundary reduces as the metal deposition thickness becomes very small such as in the present metal waveguide. The concentration of grain boundary per unit volume therefore increases and facilitates electromigration. A solution to this problem is to use a metal deposition process that produces large grain size even for thin films. It would be desired that the metal constituting the waveguide be a single crystal since it lacks grain boundaries. In addition, electromigration resistance can be improved with the presence of another metal whose ionic mobility is lower than that of the constituting metal of the waveguide's core. This metal combination (or alloy) may adversely affect the propagation loss of the waveguide. In addition, it would be preferable that the alloy be deposited in its amorphous form since it lacks the grain boundaries favorable to electromigration [34]. The presence of H_2 in gold is known to increase the electromigration resistance [35].

The electromigration phenomenon is non-reversible and will eventually destroy the wire if the current density is not reduced. Hence, in these conditions, the resistance of the wire can change dramatically over time. The rapidity of degradation, for a given current density, depends on material deposition conditions, metal melting point and temperature of the structure [25] just to name a few. From these facts, this morphology-altering phenomenon could potentially be a limiting factor on the performance, reliability and life-time of the thermo-optic device. Therefore, we must investigate, given our range of operation, if this is an immediate problem.

Usually products are tested for long-term reliability, but for the purpose of this thesis, only a short-term electromigration test will be investigated. A waveguide surviving this test is believed capable of surviving at least a few days within the normal limits of operation if not more. In order to conduct the electromigration test, probes were inserted onto the pads beside the waveguide and different levels of current intensity starting at 0.1 mA with increasing steps of 1mA, were injected into the waveguide. Because electromigration alters the resistance of the waveguide, each level of current intensity was applied for two minutes using a current source and the resistance was observed as a function of time. The temperature of the sample was stabilized during the whole experiment through the TEC. In 8, 6 and 4 μm wide and 15 nm thick waveguides, 13, 10 and 7 mA were required respectively before a variation of resistance as a function of time could be detected. The corresponding threshold electromigration current densities are 108.3, 111.1 and 116.6 GA/m^2 respectively. We would expect that resistance increase steadily from degradation of the waveguide, but in fact, the resistance would reduce and increase multiple times as a function of time. Eventually, the resistance increases before the waveguide is completely destroyed. After the test, the waveguide was brought back to room temperature and the resistance was measured and compared to those before the test. Both values were distinct indicating that electromigration altered the waveguide's resistance. This along with short-term tests, are reasons why the true electromigration threshold current density is believed to be lower than demonstrated by this test. This is consistent with the current density values obtained from literature. The maximum current density used in the experiments was 66.6 GA/m^2 and this is deemed sufficiently low to not have a destructive impact on the waveguide in the short-term but, yet, high enough to have a reasonable impact on the optical mode. The electromigration issue is therefore not an immediate concern in the short-term.

Before and after injecting current to heat the waveguide throughout the experiments in this chapter, the resistance was measured and compared. The results suggest that no macroscopic changes occurred in each waveguide during the optical measurements, which typically lasted a few hours. Therefore, in all the measurements, it was assumed that no significant metal degradation occurred causing the results to be questionable.

As was already mentioned in chapter 2, the modes supported by the waveguide are very sensitive to any irregularities in the thin metal film due to their highly localized fields near interfaces. Although surface plasmon-polaritons were used to evaluate the quality of deposited film, they were never used to study metal degradation due to electromigration. As electromigration degrades the quality of the film, it is expected to influence the surface plasmon-polariton mode propagating through the metal optical waveguide.

In order to investigate this impact, the same setup as explained in section 3.4.2 was also used here. Essentially, the input of the waveguide was excited with a PM fiber whose polarization is set perpendicular to the plane of the waveguide. The output of the waveguide was collected by a multimode fiber (MMF) connected to an optical power meter. The temperature of the sample was set to match the refractive index of the polymer and silica claddings. At first, the optical output was measured without injecting current through the waveguide. Subsequently, different levels of current intensity starting at 3 mA with increasing steps of 1mA were injected into the waveguide. The optical output was measured as a function of time for a given injected current density. Of course, upon injecting current through the waveguide, it will heat and cause a refractive index mismatch that will tend to cutoff the mode supported by the waveguide. However, once the temperature has stabilized in the structure, it is expected that the optical output will remain constant assuming that electromigration is not occurring. In the event that electromigration degrades the waveguide, it is expected that the optical output will fluctuate as a function of time.

The experiment was preliminary so only qualitative results are provided at this time. We observed that at current densities lower then the electromigration threshold current density, the output optical power remained constant. On the other hand, for current densities higher than that for electromigration, the optical output was attenuated as a function of time. Interestingly enough, at even higher current densities, upon increasing the current, the optical output intensity temporarily increased for a few seconds and, then, resumed its steady decrease. The temporary optical fluctuation is believed to be due to the thermal transients. Even when the waveguide was destroyed due to electromigration, the optical output power could still be observed, but its intensity was slightly reduced as compared to that before the electromigration test.

The main difference between the resistance fluctuation measured above and the optical fluctuations is that, at every increase in level of current density, the optical output consistently increased before resuming its steady decrease. On the other hand, the resistance fluctuation did not seem to follow any particular pattern except at the rupture of the waveguide.

Finally, another phenomenon that has a destructive impact on the waveguide is the electrostatic discharge (ESD). Given the electromigration tests, we know that a current density even lower than 110 GA/m^2 may cause degradation of the waveguide. Given the resistance of the samples, only 77 V is required to cause degradation of the waveguide. A few standard human body ESD models exist in the literature, but it is still not clear which one reflects most accurately the reality since the result depends on the exact method of measurement [36]. However, it is known that our body can easily develop a difference of potential of many thousand volts in the right conditions [37]. In addition, each model has something in common; the human body can accumulate enough charge to sustain a human body ESD of a few amperes for a few microseconds [36]. To develop a model to determine the minimum amount of energy (sustained current) required to destroy a thin metal electrode would require extensive research and this is too great a task for this thesis considering that it is not part of our main goal. However, because the human body can sustain ESD current many orders of magnitude higher than that required for electromigration in our metal waveguide, it is expected that the time required for the waveguide to rupture (or to be destroyed) would be significantly less than 2 minutes (see electromigration tests explained earlier). Therefore, amperes of current sustained for a microsecond or less seems plausible to destroy the waveguide.

An experiment was conducted by accident, which confirms our suspicion. After setting up the experiment as explained in section 3.2.2, the waveguide was observed through a microscope. The waveguide was of good quality and the Keithley source meter indicated its resistance. Unfortunately, right after observing the waveguide, one of the waveguide's electrodes was touched and I was not grounded. A big shock was felt; a large ESD occurred through the waveguide. According to the literature, an ESD of at least a few thousand volts occured. It is at that moment, that the source meter indicated an open circuit proving that the waveguide was ruptured. It could be observed through the microscope that the waveguide was, now, completely destroyed as shown in Figure 3.10 (b). In fact, damages caused by ESD are much more severe than that from the electromigration as can be observed by comparing Figure 3.10 (a) and (b). The optical output could still be observed even when the waveguide was completely destroyed by ESD, but its intensity was reduced substantially.

Hence, we are concerned that an ESD coming from the human body or other source could destroy the waveguide. It is crucial that we take all necessary precautions to prevent the device from the damaging effect of ESD. Standard ESD prevention and protection circuitry can be applied to protect the metal waveguide. ESD protective equipment includes but is not limited to wrist wrap connected to ground, ESD protected work stations, protective packaging, protective bags, conductive foam, electrostatic detector, conductive floors, special clothing, air ionizers and faraday shielding. Protection circuitry includes but is not limited to series resistance, shunt capacitance and shunt diodes at the input electrode of the device. Alternatively, more elaborate circuitry can be used to protect the device such as the use of transistors.

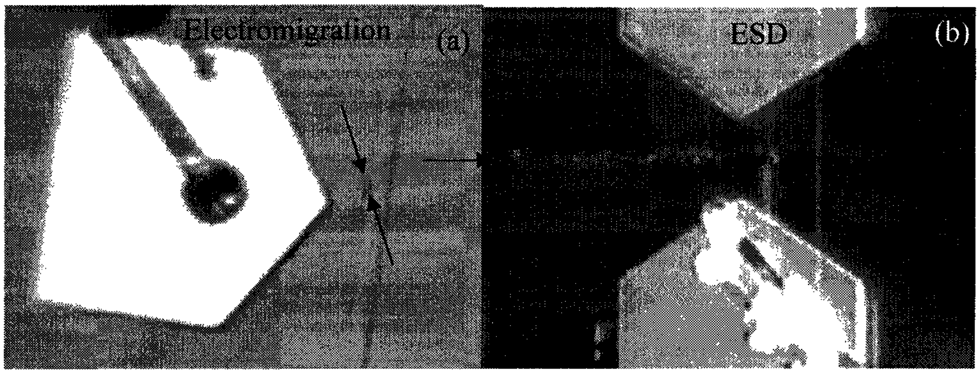

Figure 3.10: Degradation due to electromigration and electrostatic discharge of the metal optical waveguide. a) is degradation due to electromigration whereas b) is the degradation due to ESD.

3.4 Optical characterization of waveguide

3.4.1 Insertion loss as a function of sample temperature

In the last section, the waveguide was calibrated, characterized electrically and thermally. The waveguide will now be investigated optically. As was explained earlier, the optical modes supported by the waveguide can be cutoff simply by introducing an asymmetry in the refractive index profile near the waveguide. This can be achieved in two ways, injecting a high current density into the waveguide and/or heating/cooling the sample with a TEC. We will start by investigating the latter situation. The goal is to measure the IL as a function of sample temperature or equivalently, the induced refractive index asymmetry. The sample must first be prepared for the experiments, then, measurements will be made and results will be presented.

It is known that only TM modes are supported by a thin metal film slab [7]. From these facts, it was suspected and later shown experimentally that the propagation loss of the laser beam propagating through the finite width waveguide is very sensitive to its polarization state [19] [20]. Equivalently, the waveguide has a very high PDL in this particular waveguide geometry. For this reason, a Tunics polarized laser was connectorized to a PMF and its polarization was oriented normal to the metal deposition plane in order to minimize propagation loss.

The elevation angle of the fiber is matched to that of the sample by making the fiber parallel to the TEC on which lies the sample. The other horizontal angle was adjusted by placing the input fiber over the sample with its position aligned with that of the waveguide such that, by observation, we could match the angle of the fiber with that of the waveguide.

The input fiber was, then, removed from the top of the sample and placed at the input cleaved vertical face of the sample where the input of the waveguide is located. The position of the input fiber was aligned vertically and horizontally with the input of the waveguide with the use of micro-positionners. In order to minimize the return loss, index matching oil was used between the fiber and the input of the sample. To make sure that the input fiber was aligned properly to the input of the waveguide, the output of the waveguide was captured by an "Electrophysics" CCD camera using a Melles-Griot 6x microscope objective. The CCD camera was connected to a monitor. The position of the objective was adjusted such that the image on the monitor was in focus. Whenever the input fiber's alignment was optimal, a Gaussian shaped bright spot was displayed on the monitor. However, the spot can only be seen if the top and bottom claddings' refractive indices are matched; therefore, the TEC was tuned to match the claddings prior to trying to observe the output of the waveguide.

An estimate of the temperature needed to match the claddings can be determined by the following equations:

$$n\Big|_{poly,\lambda 1,T2} = n\Big|_{poly,\lambda 1,T1} + \frac{\partial n}{\partial T}\Big|_{poly,\lambda 1,T1} *(T2-T1) \tag{3.8}$$

$$n\Big|_{sio2,\lambda 1,T2} = n\Big|_{sio2,\lambda 1,T3} + \frac{\partial n}{\partial T}\Big|_{sio2,\lambda 1,T3} *(T2-T3) \tag{3.9}$$

where Equation (3.8) and (3.9) are linear equations describing the dependence of the refractive index to temperature. n, $\frac{\partial n}{\partial T}$ and T represent the refractive index, TOC and temperature respectively. T1 and T3 are the temperatures from which the refractive indices of the polymer and silica were measured or obtained from the literature. T2 is the temperature at which polymer and silica will be brought to match their refractive indices. The subscripts identify of the material, the wavelength and temperature for which the refractive index and TOC are represented respectively. When the refractive index of the silica and polymer are matched, Equation (3.8) and (3.9) are equal. By equating these two equations and isolating T2, we obtain:

$$T2 = \frac{n\Big|_{sio2,\lambda1,T3} - n\Big|_{poly,\lambda1,T1} + T1 * \frac{\partial n}{\partial T}\Big|_{poly,\lambda1,T1} - T3 * \frac{\partial n}{\partial T}\Big|_{sio2,\lambda1,T3}}{\frac{\partial n}{\partial T}\Big|_{poly,\lambda1,T1} - \frac{\partial n}{\partial T}\Big|_{sio2,\lambda1,T3}} \tag{3.10}$$

which is the temperature required to match the claddings. Replacing the variables with the material properties mentioned in the beginning of the chapter, we obtain a temperature of 31.52°C. We iteratively optimized the temperature and position of the input of the waveguide to obtain a nice bright spot in the monitor. In the experiments, the actual temperature to match the claddings was near 27.50°C.

Since the CCD camera is connected to a computer, it is possible to take digital pictures of the output of the waveguide. Now that the alignment is reasonable enough to excite the waveguide, the microscope objective and CCD camera were removed and the optical output was collected instead by an Agilent power meter through a MMF.

The reason for using a MMF at the output of the sample was to collect the maximum amount of light near the waveguide resulting from its large core. However, after reflection, we realized that the core of the MMF was too large. It not only captured the optical power supported by the waveguide, but it also captured the power from cladding and radiative modes. As a result, even when the waveguide was cutoff, the MMF still collected a reasonable amount of cladding and radiative power. A SMF would have been a better choice since its core is small enough to only capture the optical power supported by the plasmon-polariton waveguide. Therefore, with the presence of a SMF at the output of the sample, the TO VOA is expected to achieve a better ER than with that of a MMF.

In any case, the angle and position of the output MMF was matched to that of the waveguide using the same procedure than was done for the input fiber. The alignment of the output fiber was optimal whenever the power detected was maximized. Finally, a final adjustment was made by iteratively optimizing the input and output fiber and temperature of the sample. The alignment of the input fiber was optimized with the power meter because it is more accurate than making an estimation based on the observation of the CCD camera. The electrodes were inserted onto the pads prior to having aligned the fibers with the waveguide, because inserting electrodes can move the sample; the fibers would need to be realigned.

The measured IL as a function of sample temperature is displayed in Figure 3.11. There are a few phenomena competing to produce those results. The first phenomenon was purposely designed as the refractive index mismatch. As the sample temperature changes, the claddings eventually becomes unmatched and the optical modes is displaced such that less power is collected by the MMF. Notice the asymmetry in the IL profile surrounding the optimum temperature (temperature matching the claddings). This occurs because the optical mode starts to be displaced due to the refractive index mismatch at the waveguide level and sees an asymmetric structure due to the proximity of the silicon and its large refractive index. A very similar structure was investigated experimentally except that the silica was made very thick (making a more symmetrical structure) and results were shown to be much more symmetrical [38]. The curve represented by 6μm.13 and 4μm.13 do not reflect the real IL because the input of the sample was contaminated with the conductive compound used between the sample and TEC. The main impact of the contamination is to increase uniformly the IL over the whole range of temperature. There was no simple way of cleaning the sample without risk of destroying it because the curing gel is very delicate. It is to be noted that the .14 and .13 samples have a difference in length. The .13 sample is 7.31 mm long while the .14 sample is 7.13 mm long; therefore, the results are not strictly comparable even though we will do so.

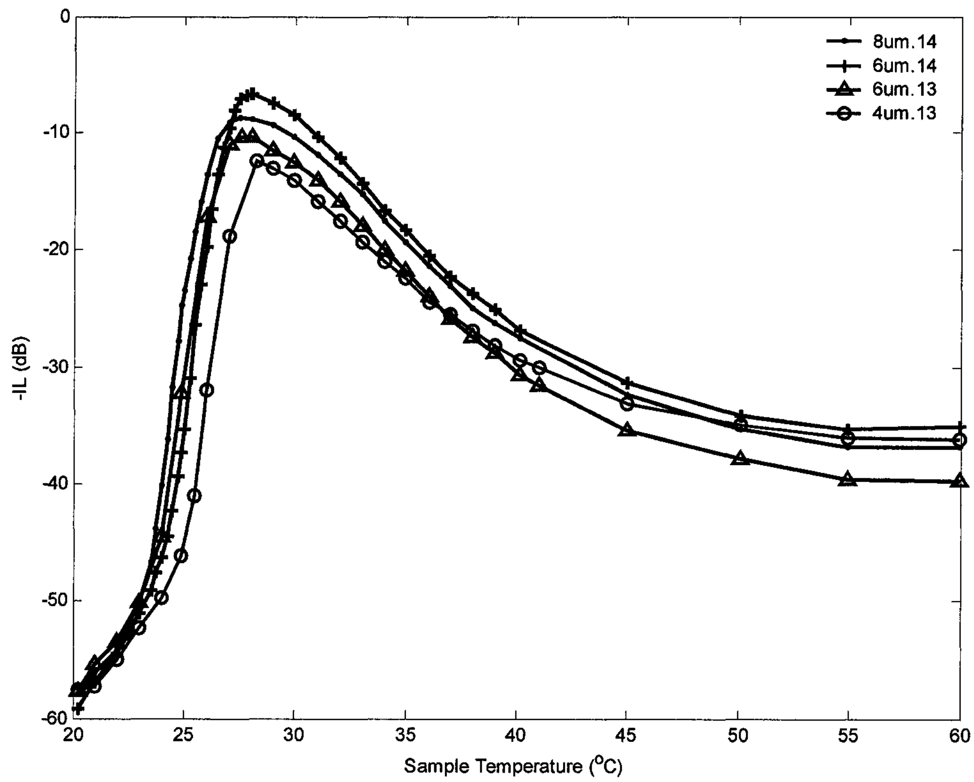

Figure 3.11: Insertion loss as a function of sample temperature. 8μm.14 indicates that results were obtained from an 8μm wide waveguide on the .14 sample. The results from the .13 sample are somewhat questionable because the sample was contaminated. The asymmetric IL profile around the optimal temperature comes from the asymmetry in the structure.

The second phenomenon is undesired and occurs due to material expansion or contraction from heating or cooling. The input and output fibers were aligned with the sample at the optimum temperature to match the refractive index of the claddings. When the TEC heats or cools the sample, the sample, the TEC and supporting structure will expand or contract. Since the input and output fibers are not fixed (or bonded) onto the sample, a misalignment may occur due to the expansion or contraction. A misalignment causes the waveguide to be improperly excited and the output will not collect as much optical power resulting in less optical power detected by the power meter.

Another less important phenomenon that contributes to the IL profile is that when the waveguide is heated its resistivity increases as was demonstrated in section 3.2.2 and 3.3.1.

The increase in resistance will have an impact on the permittivity of the metal in reference to Equation (2.1) through (2.5), which will also affect the IL.

Those were the phenomena competing to produce the result in Figure 3.11. The second phenomenon can be eliminated by bonding the input and output fibers to the sample. However, given the limited number of samples and the possibility that gluing the sample properly might fail, the risk was too high to attempt. It was not clear which two dominating phenomena was most important. Robert Charbonneau, working at Spectalis Corp. such as I was during the course of my thesis, had a large quantity of samples. He was able to use a similar structure for the same experiment except that the input and output fibers were bonded onto the sample. Comparing both results revealed that the misalignment due to expansion is the dominating effect of the IL profile shown in Figure 3.11 [38] (more on this in the discussion of chapter 5).

An array of pictures was taken with the CCD camera for the 6 and 8μm wide waveguide on the .14 sample at different temperatures. As can be seen in the array of pictures in Figure 3.12, there is some unwanted noise that degrades the quality of the picture. We later found out that because instruments were connected on different power bars, it caused ground loops, which were the source of the noise. Unfortunately, during the experimentation process the sample was broken so those are the best pictures currently available. Fortunately, this is not the case in Figure 3.13. When the temperature of the sample is below that required to match the claddings as shown in Figure 3.12 (a) and (b) and Figure 3.13 (a) and (b), the refractive index of the polymer is higher than that of the silica, the waveguide is cutoff and most of the power radiates into the polymer. In addition, the fibers are misaligned with the sample due to expansion and contraction of the materials. As the temperature is further increased, the refractive index of the polymer and silica becomes closer, less optical power radiates into the polymer and more is guided by the metal waveguide. At the optimum temperature, the claddings are matched and almost no power radiates as shown in Figure 3.12 (e) and Figure 3.13 (e). Furthermore, the fibers are properly aligned with the sample. This is where the IL is minimal. When the sample temperature is higher than that to match the claddings, the refractive index of the polymer is below that of the silica. We would expect the optical power to start radiating towards the silica, but this does not happen. Instead, the spot only dims and change shape slightly. The presence of the silicon having a large refractive index mismatch with silica has a confining effect that prevents light from escaping the waveguide through the silicon given that light propagates parallel to its interface. In addition, the fiber misalignement causes the output to dim.

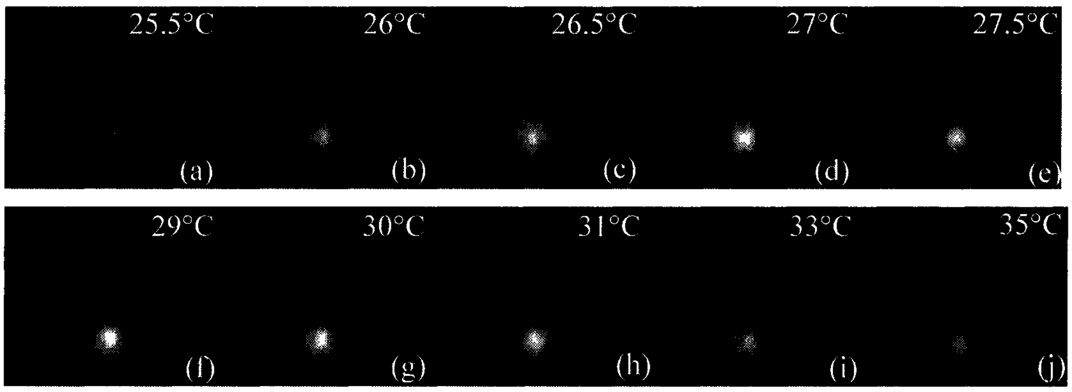

Figure 3.12: Picture array of optical output as a function of TEC temperature for the 8μm wide waveguide on sample .14.

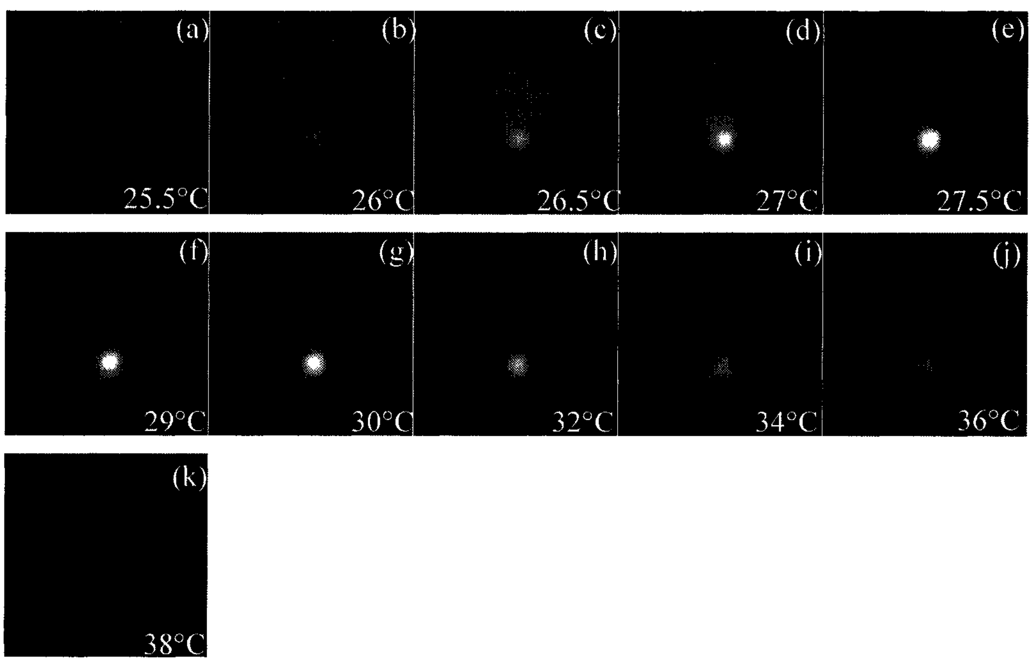

Figure 3.13: Picture array of optical output as a function of TEC temperature for the 6μm wide waveguide on sample .14.

3.4.2 Insertion loss and extinction ratio as a function of power density

We are now going to investigate the IL and ER as a function of current injected into the waveguide. The same setup as the previous section is used except that the TEC temperature is set to match the claddings while a high current density is injected through the waveguide. Other combinations could have been chosen. In reference to figure 3.11, we could have set the TEC temperature under the optimum value to match the claddings and, then, inject a current through the waveguide to bring it to the optimal temperature. However, because only 4.44mm or less of the waveguide is heated relative to its total length (near 7 mm) as shown in Figure 3.1, a portion of the waveguide would remain unmatched causing the ER of the VOA to be poor. Thus, the earlier method is chosen.

An array of pictures was taken with the CCD camera for various applied electrical power densities for the 8 and 6μm wide waveguide from the .14 sample. In each case, the heated length was 4440μm on a sample around 7.3mm long. The claddings were matched with the TEC prior to injecting current through the waveguide. On the lower right hand corner of each figure is a number which represent the applied electrical power density in $\frac{mW}{\mu m^3}$. As shown in Figure 3.14 and 3.15, as more current is injected through the waveguide (or for higher applied electrical power density), the bright spot is seen to dim. Also, not as clear in Figure 3.14 (c), (d), (e), (f), (g) and (h) and Figure 3.15 (c), (d), (e) and (f) we can see a small amount of optical power radiating from the sides and top of the waveguide.

The maximum temperature of the waveguide is at its core and reduces with distance from it. The polymer's TOC is negative; therefore, its refractive index near the core of the waveguide will be lower than that further from the core. The TOC of silica is positive; therefore, its refractive index near the core of the waveguide will be higher than that further from the core. Light tends to propagate where the refractive index is higher. When the waveguide is heated, the refractive index gradient in the polymer becomes large enough to pull some light away from the waveguide. As a result, we can see light radiating to its sides and on top. There is no light radiating from the bottom of the waveguide because the silica's refractive index is higher closer to the waveguide. In the previous section, the picture array did not reveal any lateral radiation.

The impact of expansion and contraction of materials due to heat is assumed negligible since only a small area around the waveguide is heated as opposed to heating the whole sample with the TEC. Furthermore, only a small section near the middle of the waveguide was heated. Both ends of the waveguide are not heated and it is not expected that the input and output fibers become misaligned with the sample. In any case, it would have still been preferable if the input and output fibers would be bonded onto the sample.

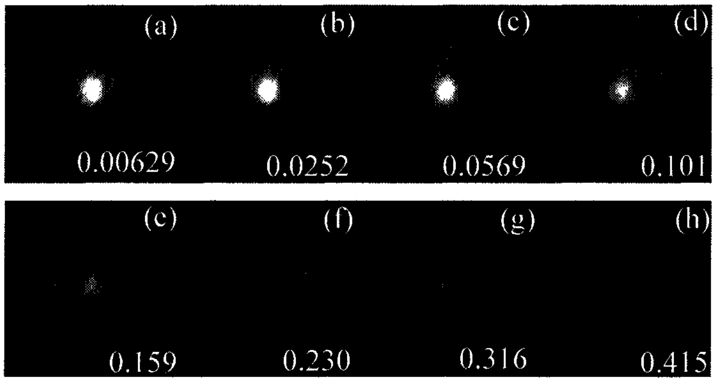

Figure 3.14: Picture array of optical output as a function of applied electrical power density for an 8μm wide waveguide with a 4.44 mm heated section on .14 sample. Electrical power density is expressed in $\frac{mW}{\mu m^3}$

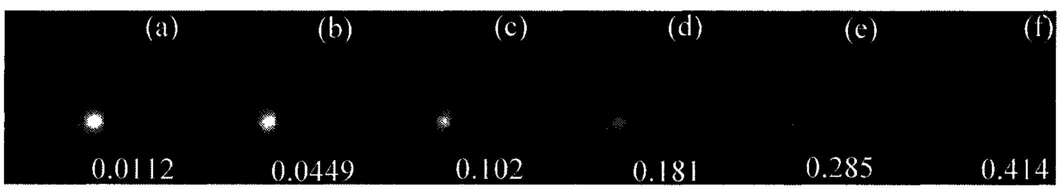

Figure 3.15: Picture array of optical output as a function of applied electrical power density for a 6 μm wide waveguide with a 4.44 mm heated section on .14 sample. Electrical power density is expressed in $\frac{mW}{\mu m^3}$

The CCD camera was removed and a MMF connected to a power meter was aligned with the sample. IL and ER measurements as a function of applied electrical power density are shown in Figure 3.16, 3.17 and 3.18 respectively for various heated waveguide widths and lengths.

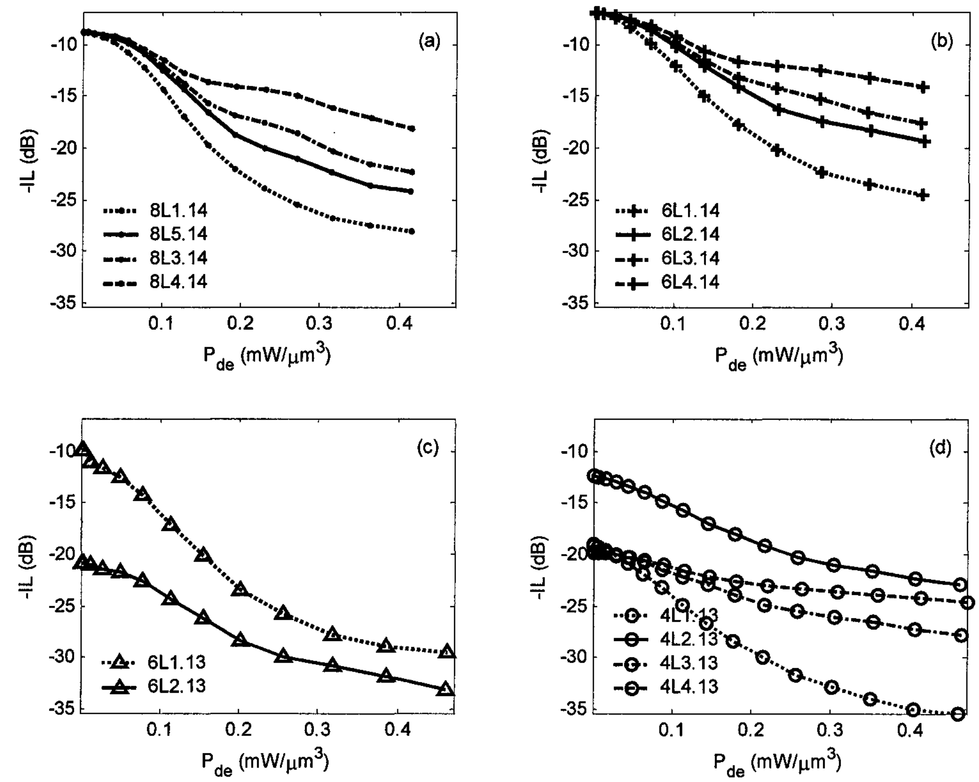

Figure 3.16: Insertion loss as a function of applied electrical power density for a variety of waveguide widths and lengths. a) and b) are measurements of the 8 and 6μm wide waveguide on the .14 sample respectively while c) and d) are measurements of the 6 and 4 μm wide waveguide from the .13 sample. In the legend, the first number indicate the waveguide widths in microns and is followed by L1, L2, L3, L4 or L5 specifying the length of the heated section of the waveguide. The last value identifies the sample. Any IL measurements obtained from sample .13 are somewhat questionable because of its contamination. L1=4440μm, L2=2240μm, L3=1640μm, L4=840μm and L5=2290μm.

The comparison of Figure 3.16 a) and b) shows that the unheated 8μm wide waveguide exhibits more IL than that of the 6μm wide waveguide. Figure 3.17 shows that a longer heated section of the waveguide, for a given width, enables a larger ER. Figure 3.18 reveals that a wider waveguide, for a given length, achieves a larger ER because it achieves a larger variation of temperature. Figure 3.19 shows the same information as figure 3.17 except that it is expressed as a function of electrical power consumption.

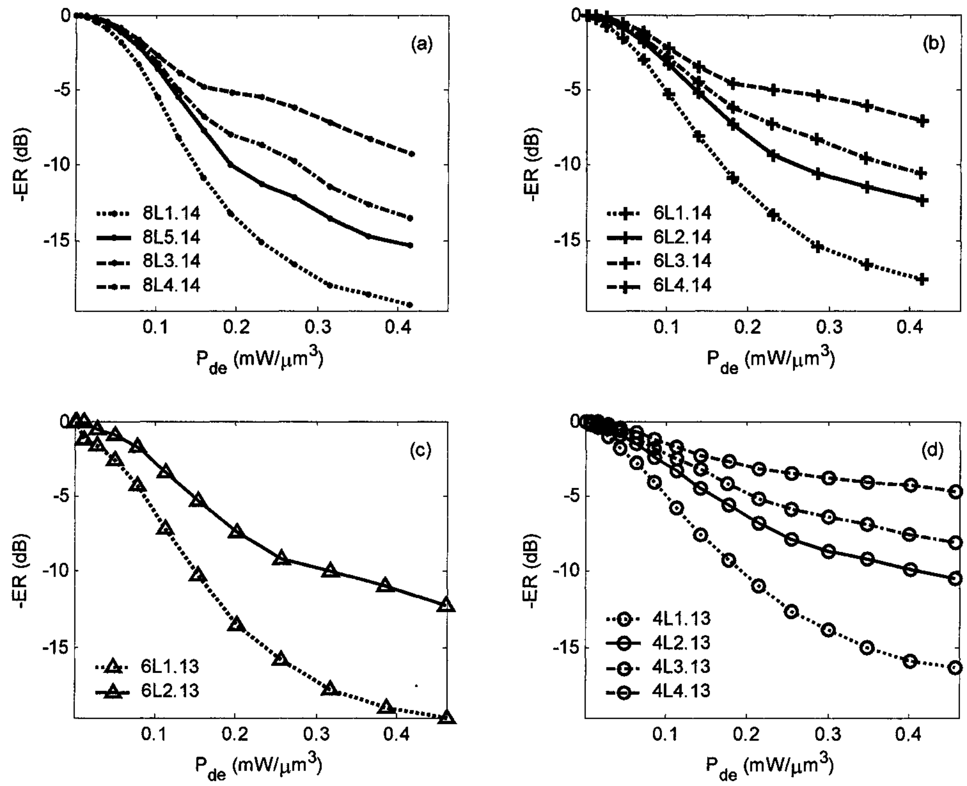

Figure 3.17: Extinction ratio as a function of the applied electrical power density for a variety of waveguide widths and lengths. a) and b) are measurements of the 8 and 6μm wide waveguide on the .14 sample respectively for different lengths while c) and d) are measurements of the 6 and 4 μm wide waveguide from the .13 sample respectively for different lengths. In the legend, the first number indicate the waveguide widths in microns and is followed by L1, L2, L3, L4 or L5 specifying the length of the heated section of the waveguide. The last value identifies the sample. L1=4440μm, L2=2240μm, L3=1640μm, L4=840μm and L5=2290μm. Contamination of sample .13 is not expected to have an impact on the ER.

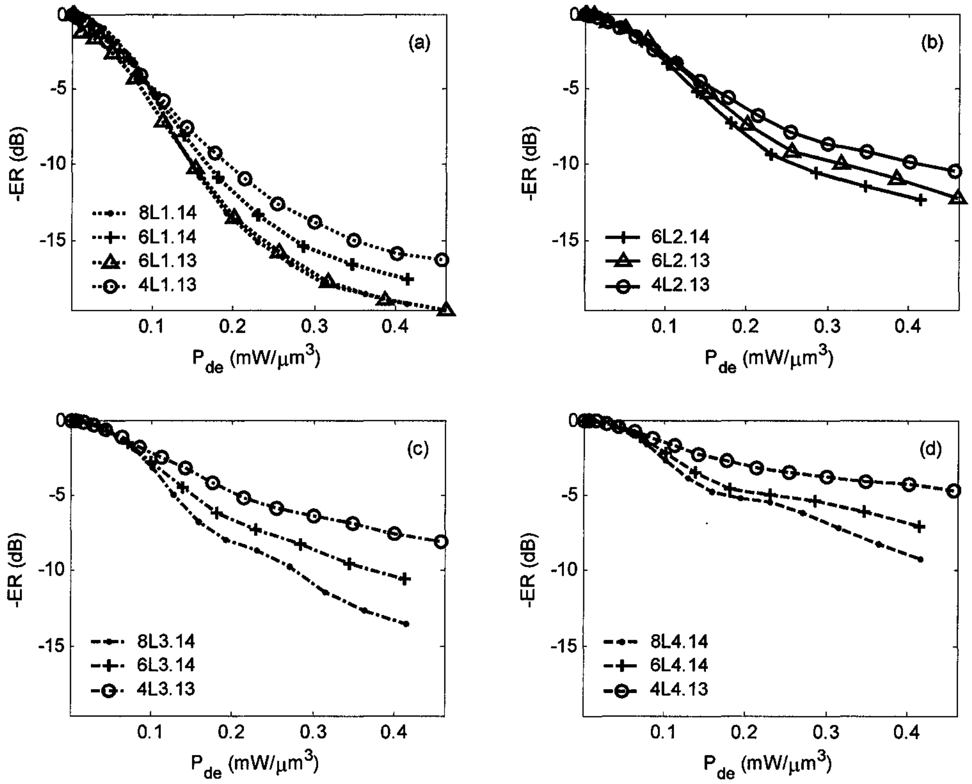

Figure 3.18: Extinction ratio as a function of applied electrical power density for a variety of waveguide widths and lengths. It compares the same information as the previous figure in a different order. a), b), c) and d) compare the same waveguide length to different widths. In the legend, the first number indicate the waveguide widths in microns and is followed by L1, L2, L3 or L4 specifying the length of the heated section of the waveguide. Finally, the last value identifies the sample. L1=4440μm, L2=2240μm, L3=1640μm, L4=840μm. The contamination of sample .13 is not expected to have an impact on the ER.

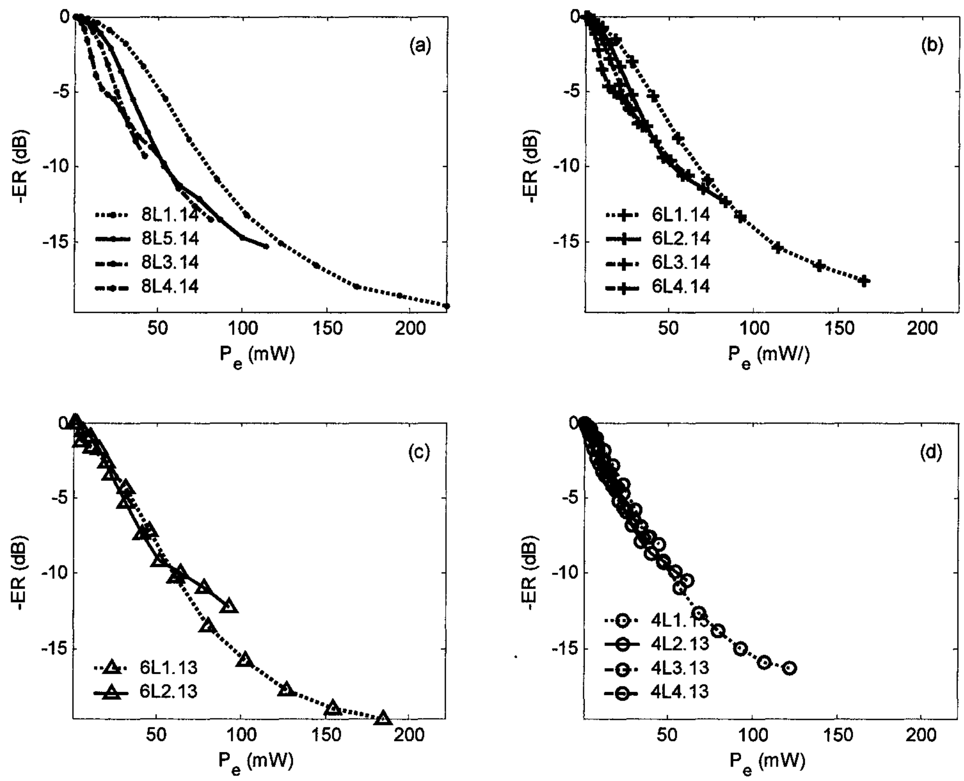

Figure 3.19: Extinction ratio as a function of applied electrical power for a variety of waveguide widths and lengths. In the legend, the first number indicate the waveguide widths in microns and is followed by L1, L2, L3 or L4 specifying the length of the heated section of the waveguide. Finally, the last value identifies the sample. L1=4440µm, L2=2240µm, L3=1640µm, L4=840µm, L5=2290µm. The contamination of sample .13 is not expected to have an impact on the ER.

Results of Figure 3.19 show that an 8µm waveguide whose 4.44mm section is heated with a power consumption of about 222mW is able to achieve 19dB ER for this particular structure.

3.4.3 Determination of propagation loss, coupling loss and return loss

In addition to the IL, we would like to obtain the return loss (RL), coupling loss (CL) and propagating loss of the waveguide from the measurements. We can obtain these results by following the standard fiber optic test procedures (FOTP). The procedure to obtain the propagation loss of the waveguide is the well known cutback method [39]. Essentially, we must make IL measurements for a few different sample lengths (or waveguide lengths). The

IL is plotted as a function of waveguide length. A straight line is fitted through the data points using a least square method. The value of the straight line at the abscissa is the total coupling loss from the input and output of the sample. Assuming the input and output coupling loss are equal, we divide the result by two to obtain the coupling loss of either the input or output of the sample. The slope of the straight line is the propagation loss.

Unlike, the description in the FOTP, we are purposely using a polarizing maintaining coupler for our particular measurements. Since the coherence length of the input laser is a few meters while the sample size is about 7mm and since the laser has a narrow linewidth, constructive and destructive interference will influence the results. To eliminate the effect of interference, a broadband source would be required. A broadband optical source is available but not in a connectorized form, which is necessary to be able to connect it to the only available coupler for the RL measurement. Another method can give similar results than that of a broadband source; one needs to sweep the tunable laser near the wavelength of interest, fit a line through the experimental data and find the value at the wavelength of interest.

IL measurements were done for three sample lengths: 7.31 mm, 5.60 mm and 3.42 mm respectively for the 8μm waveguide on sample .13. Typically, four or more sample lengths should be measured to obtain acceptable results, but there was not enough samples to do so. Furthermore, these measurements could not be conducted for the 4μm and 6μm wide waveguides because, at the point in time, these samples were damaged. The measurements were done at a temperature matching the claddings and without injecting current into the waveguides. IL measurements as a function of wavelength near 1550nm are presented in Figure 3.19. The straight line superimposed onto the data points is a linear fit as explained above. Figure 3.21 (a) shows the IL as a function of sample length. A straight line is fitted through the data points from where we obtained a coupling and propagating loss of 1.32 dB and 11.83 dB/cm, respectively. We compared these result with those obtained from other samples where the metal waveguide was thicker [40]. The results were noticeably different. The quality of the metal deposition of sample .13 and .14 are not believed to be as good as the later sample measured in [40], which may contribute to higher propagation loss. In fact, many of the earlier samples were not perfectly rectangular; some of the waveguides were slightly elevated at the superior edges attributed to lift-off lithography. In addition, the measurements in reference [40] did not have pads or arm coming out of the straight waveguide. The pads and arms of the waveguide should have a negligible impact on the optical mode, but this was not confirmed experimentally. More measurements should be made to validate these results in the future, if the necessary resources are available.

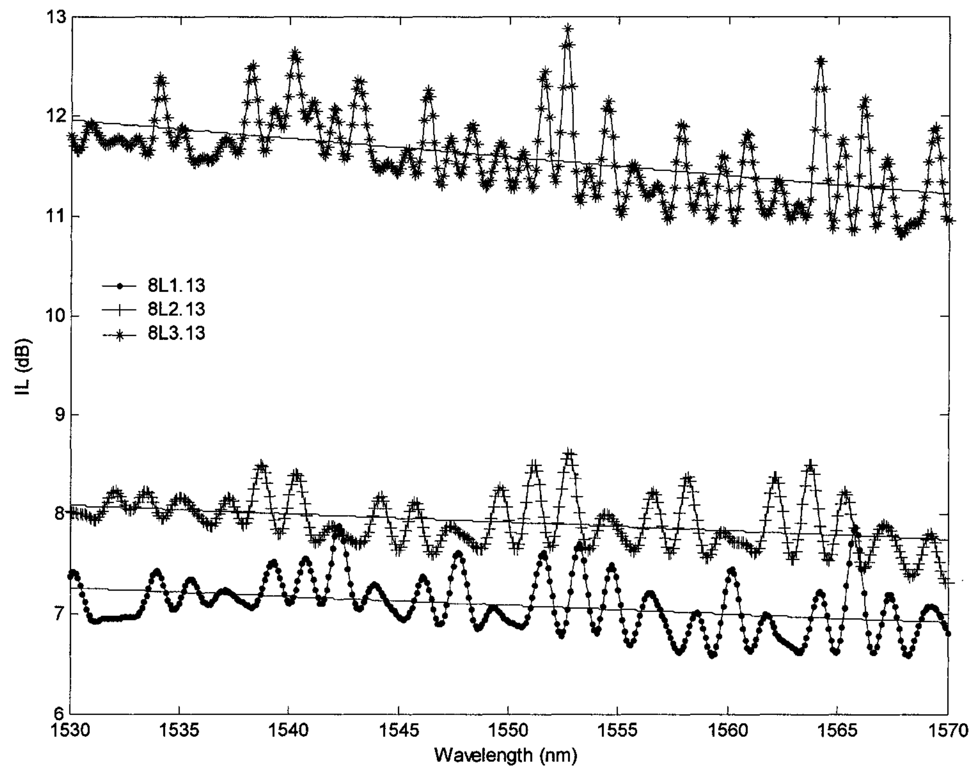

Figure 3.20: Insertion loss as a function of wavelength for the 8µm wide waveguide at different waveguide length. The ripples are in great part due to interference effects. The straight line is used to average the effect of the ripples and obtained the insertion loss at the desired wavelength. L1=3.42 mm, L2=5.06mm and L3=7.31mm

According to reference [42], to obtain a RL measurement, we need to use a three port coupler. If a coupler has more ports, the other ports must be matched at all times. The output of the laser source is connected to port one (P1) of the coupler as shown in Figure 3.19. The output of the coupler (P3) is connected to the input of the device under test (DUT). For our sample, this means that the fiber is aligned with our waveguide as described earlier. The temperature of the sample is also adjusted to match the cladding. Finally, the output of the sample (or DUT) is matched. Any power reflected from the DUT goes back into the coupler through P3 and a fraction of this power comes out of P2 where an optical detector is connected. Before making any measurements, the coupler must be calibrated, which is described by the FOTP.

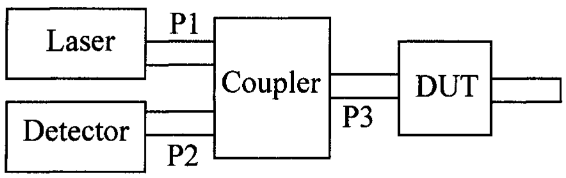

Figure 3.21: Instrument configuration to make return loss measurements.

In such a setup, the RL is defined as:

$$RL = -10 * \log\left(\frac{P2DW - P2W}{P3W}\right) - IL_{32} \tag{3.10}$$

where RL is the return loss expressed in dB. P2DW is the power expressed in mW coming out of P2 when the DUT's input is connected to P3 and its output is matched. P2W is the power expressed in mW coming out of P2 when P3 is not connected to the DUT but is matched instead. IL_{32} is the IL between P3 and P2 and is express in dB. The results of the return loss measurements as a function of wavelength are shown in Figure 3.21, where (b), (c) and (d) are related to the 3.42 mm, 5.06 mm and 7.31 mm samples respectively. In all cases, the return loss is around 50 dB.

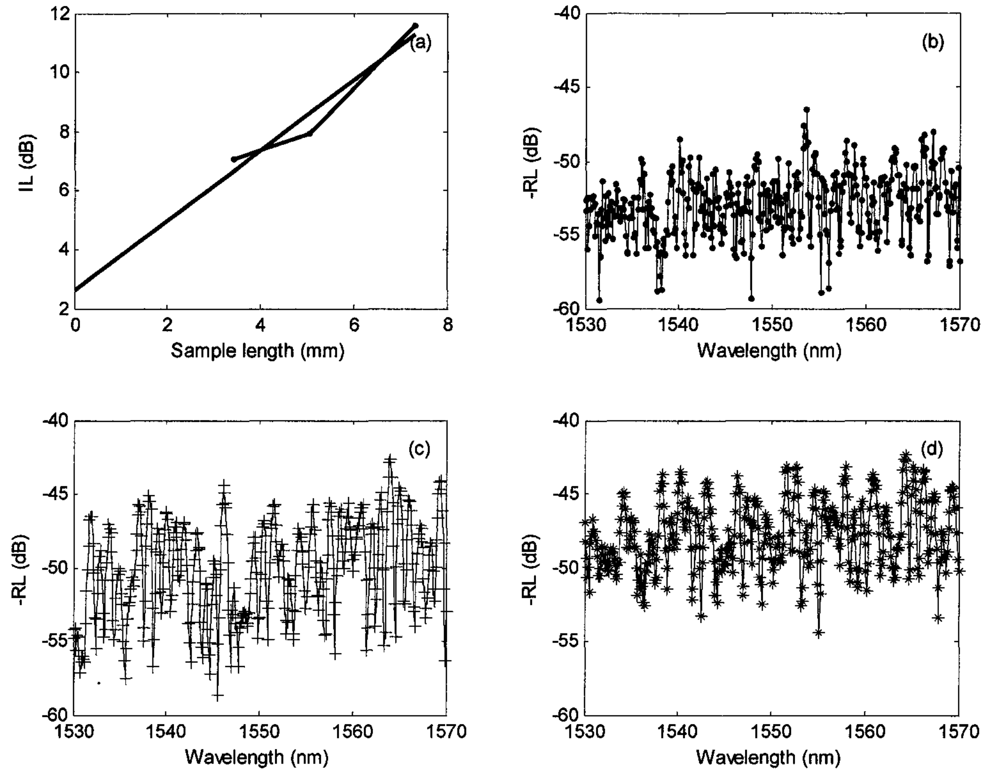

Figure 3.22: Insertion loss as a function of sample length and return loss as a function of wavelength. a) shows the insertion loss as a function of sample length used to determine the coupling loss and propagation loss. b), c) and d) are the return loss as a function of wavelength for a 3.42, 5.06 and 7.31mm samples respectively.

3.4.4. Mode field diameter measurements

From the pictures taken from the CCD camera, we obtain qualitative images, but we would like to obtain quantitative results: the mode field diameter. Quantitative results can be obtained with a beamscanner. The beamscanner is an optical detector whose position is swept behind two narrow intersecting perpendicular slits where the beam is shone. The beam passing through the slit is diffracted, scanned by the optical detector and deconvolved by software. The instrument generates two orthogonal intensity profiles whose direction is selected by rotating the slit in the desired position. For our purpose, the slit was rotated such that the vertical and horizontal intensity profile of the waveguide was measured. The mode field diameter measurements using a Beamscanner is relatively new and no standard test procedures yet exists. The measurements were conducted based on information sheets provided with the purchased Beamscanner. Photon fabricating the Beamscanner is writting documentation should eventually become the standard of MFD measurement using Beamscanners.

Given that the beamscanner provide little information on the beam, in order to make sure that the beam is properly adjusted at all times, the beam was split with a beam splitter and was simultaneously observed with the CCD camera as shown by Figure 3.21. A 40x flat field microscope objective was used to observe the output of the waveguide and was placed before the beam splitter. The distance of the optical path to the CCD camera was set to be exactly the same as that of the beamscanner such that we know that whenever the beam is focused on the CCD camera, it is also focused on the beamscanner. Once the beam is properly adjusted, the beam splitter can be removed and a measurement with the beamscanner can be achieved.

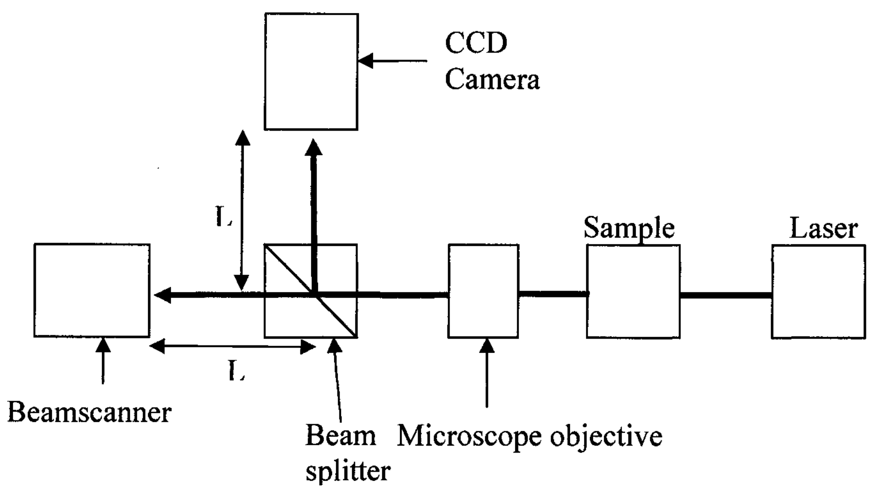

Figure 3.23: Instrument configuration to make mode field diameter measurements.

As the beam propagates, it diverges such that the size of the beam at the beamscanner is larger than that at the output of the sample. For this reason, we must calibrate the measurement to obtain the desired result. In order to do so, we excited the waveguide and adjusted the objective such that the output of the sample is focused. Without moving the sample, the microscope objective and the orientation of the PM fiber at the input of the sample, the longitudinal position of the PM fiber is aligned with the output of the waveguide and its vertical position is set slightly higher than the sample. Without moving the microscope objective, if the PM fiber is exactly aligned with the output of the sample, it should also be focused in the CCD camera. The vertical position of the objective is adjusted such that the beam is centered on the CCD camera and beamscanner. If the beam of the PM fiber is not focused into the CCD camera, its longitudinal position is adjusted. The beam splitter is removed. The mode field diameter of the PM fiber is measured with the beamscanner and is compared to its known value of 10.5 μm according to the standard definition. The electric field coming out of a PMF is approximated as a Gaussian distribution:

$$E(r) \propto e^{-\frac{r^2}{w^2}} \tag{3.11}$$

The optical power is proportional to the square of the electric field intensity:

$$P(r) \propto |E(r)|^2 \propto e^{-\frac{2r^2}{w^2}} \tag{3.12}$$

where "r" is the radial distance from the center of the fiber. "w" is a parameter of the fiber. The mode field diameter is defined as the diameter at which the electric field has reduced to 1/e of its maximum value or $1/e^2$ of its power. For a Gaussian profile as represented by Equation (3.11), the mode field diameter is defined by:

$$\text{MFD}=2\text{ w} \tag{3.13}$$

where "w" was defined in Equation (3.11).

The ratio of the expected value, 10.5μm, to the measured value is the calibrating factor. The PM fiber is aligned with the input of the waveguide, the waveguide is optically excited and the vertical position of the objective is adjusted so that the beam shines in the middle of the beamscanner. Since only the vertical position of the objective was moved, the beam is already properly focused on the beamscanner. A measurement is made and the calibrating factor is used to scale the results. This procedure was used to measure the mode field diameter of the 4, 6 and 8μm wide waveguide. The light intensity profile along the vertical and horizontal center of the waveguide were obtained and presented in Figure 3.23 (a) and (b).

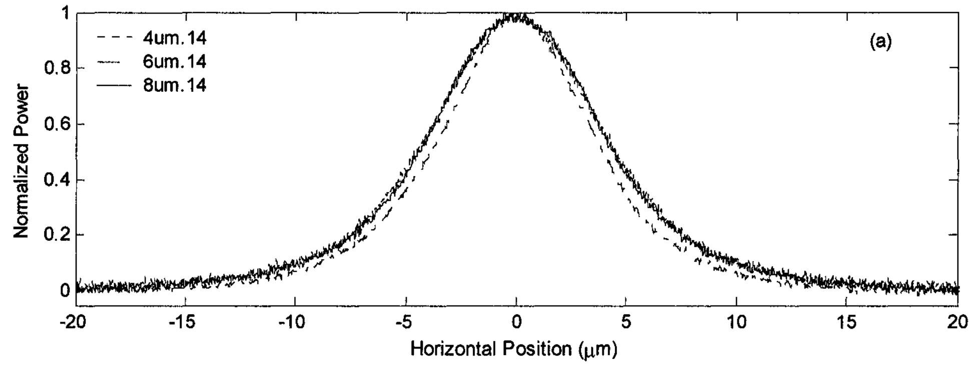

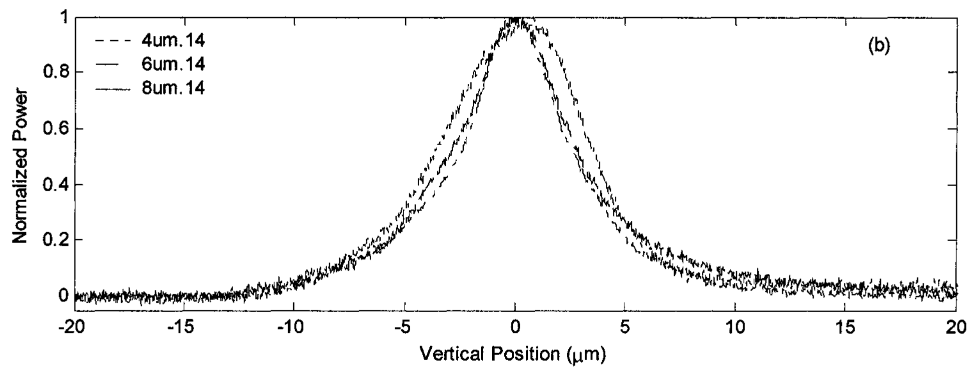

Figure 3.24: Light intensity profile as a function of horizontal and vertical position.

Results show that the 4μm waveguide has a minor and major axis diameter of 14.2 and 18 μm respectively. The 6μm waveguide has a minor and major axis diameter of 13 and 15.75 μm respectively. Finally, the 8μm wide waveguide has a minor and major axis diameter of 15 and 17.8 μm respectively. Measurements were repeated many times and results varied by as much as 1 or two microns. The results are very sensitive to the adjustment of the objective because of its large magnifying power. Furthermore, there is a range of objective positions that seems to lead to the optimum focus, but results in significantly different mode field diameters. The results are not accurate enough to compare them between themselves and more measurements would be required to confirm its validity. Although the results have a high variability, the figure shows that the mode field diameter of the major and minor axis remains near 15μm. Results prove that the mode shape is elliptical.

While investigating other sources of errors for the MFD measurements, we realized that a drop of oil from the earlier IL measurements remained at the output of the sample potentially distorting the optical power leaving the sample. In fact, observing the output of the sample through a microscope suggests that the polymer at the edge of the sample under the fiber constituting the jig was not as vertically flat as we had expected. The fiber constituting the jig should have been put further from the edge of the sample to improve the vertical flatness of the polymer from surface tension. The oil filled the areas that were not properly filled with the polymer. The effect of the presence of the oil is shown in Figure 3.22 and 3.23. Figure 3.22 (a) and Figure 3.23 (a) are the output of the waveguide with the presence of the index matching oil at its output while, in Figure 3.22 (b) and Figure 3.23 (b), there was no oil at the output.

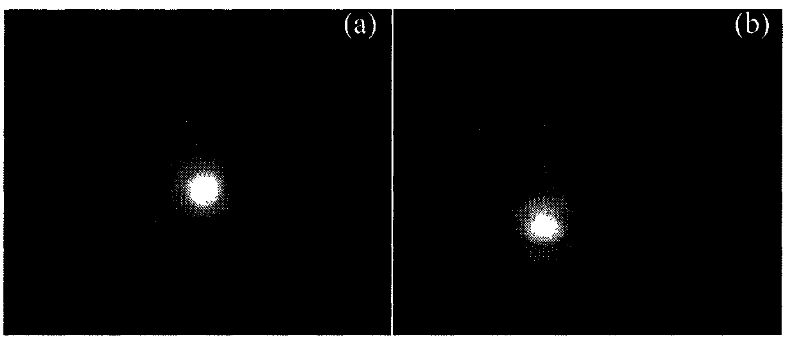

Figure 3.25: Output of sample with and without index matching oil of a 6µm waveguide taken with CCD camera.

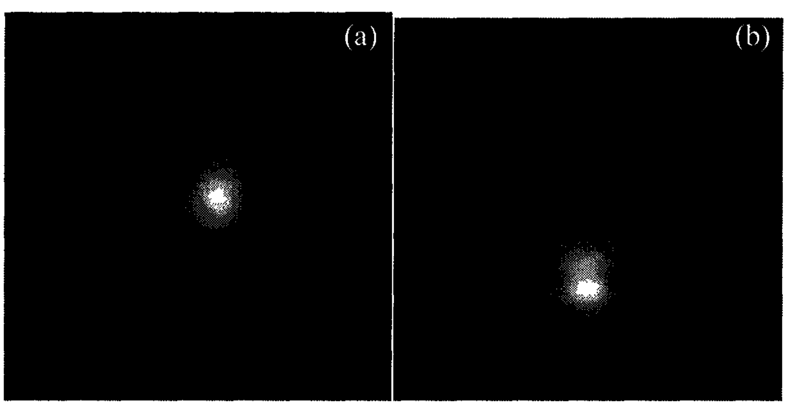

Figure 3.26: Output of sample with and without index matching oil of an 8µm waveguide taken with CCD camera.

This shows that the optical output depends critically on the quality of the output of the sample. This could also explain why the MFD did not have a great repeatability. It is to be noted that all previous CCD camera pictures where all taken with the presence of oil.

However, this has no impact on the measurements taken with the power meter because a MMF fiber was inserted at the output of the sample.

3.4.5 Rise and fall-time measurements

Other performances parameters of interest related to the thermo-optic VOA are its rise time and fall time. The rise-time is defined as the time taken for the optical power at the output of the waveguide to increase from 10% to 90 % of its maximum. The fall-time is defined as the time taken for the optical power at the output of the waveguide to decrease from 90% to 10% of its maximum. The goal of this section is to obtain the rise and fall-time of the device. The design of the experiment will be explained, results obtained and presented.

In order to make these measurements, the output of the waveguide is connected to a PDA-400, an amplified InGaAs optical detector from Thorlabs [41], via a MMF. Again, the alignment procedure was followed. The Thorlabs detector specifications are suitable for the regime of operation of the experiment; the Thorlabs detector can detect 1550nm radiation with a modulation frequency up to 10MHz and reasonable output voltage suitable for connection to an oscilloscope. The Thorlab detector has been calibrated by measuring the output voltage as a function of the input optical power and it was used in its linear region of operation. When excited with a laser beam, the detector generates an output voltage proportional to the input optical power according to its responsivity and transimpedance gain. The electrical signal is guided by a coaxial cable, which is connected to one of the two inputs of a Tektronix TDS-320 oscilloscope. From the calibration, the voltage read on the oscilloscope can be converted to its equivalent optical power. The oscilloscope has a serial port and all the information can be saved on a computer.

A waveform generator was connected to the electrodes that were inserted onto the pads to inject the current along the waveguide. The waveform generator was set to generate a square wave. The amplitude of the square wave was set high enough to inject a large amount of current to heat the waveguide sufficiently to influence the propagation of light. We verified that the rise and fall-times of the waveform generator is negligible compared to that of the VOA. The frequency of the waveform generator was set lower than the cutoff frequency of the waveguide near 50Hz.

While conducting the experiments, it was determined that the rise and fall-times are dependent on the TEC temperature and the amount of heat dissipated by the waveguide. The phenomenon has not been fully characterized. However, a choice was made to set the TEC to the temperature matching the claddings (optimum temperature) and inject a current via the waveform generator. In such a case, the optical rise-time was much longer than the fall-time as will be shown shortly.

It is important to understand that the application of voltage (or current through the waveguide), such as the rising-edge of a square voltage wave, may induce cutoff of the modes supported by the waveguide, hence, reduce the optical power captured by the optical detector. In summary, the rising-edge of the square voltage wave corresponds to the falling-edge of the output optical power, while the falling-edge of the square voltage wave corresponds to the rising-edge of the output optical power. Only the waveform of the output optical power resulting from an applied square voltage wave will be presented.

A few measurements were conducted to determine the dynamic operation of the device. The optical fall-time (or thermal rise-time) has been determined to be in the range of 35us-170us, but typically between 50us-75us as obtained from different waveguide widths, lengths and on different samples. On the other hand, the optical rise-time (or thermal fall-time) was much slower being in the range of 1.3-7ms. The optical rise-time seems to be dependent on the waveguide width, but more experiments would be required to confirm this. The optical rise-time range was typically 1-2ms, 2-3ms, 5-6.8ms for the 4, 6 and 8μm wide waveguide respectively. Figure 3.26 shows the optical rise and fall-times of the 4, 6 and 8μm waveguides for a 4.44mm heated section.

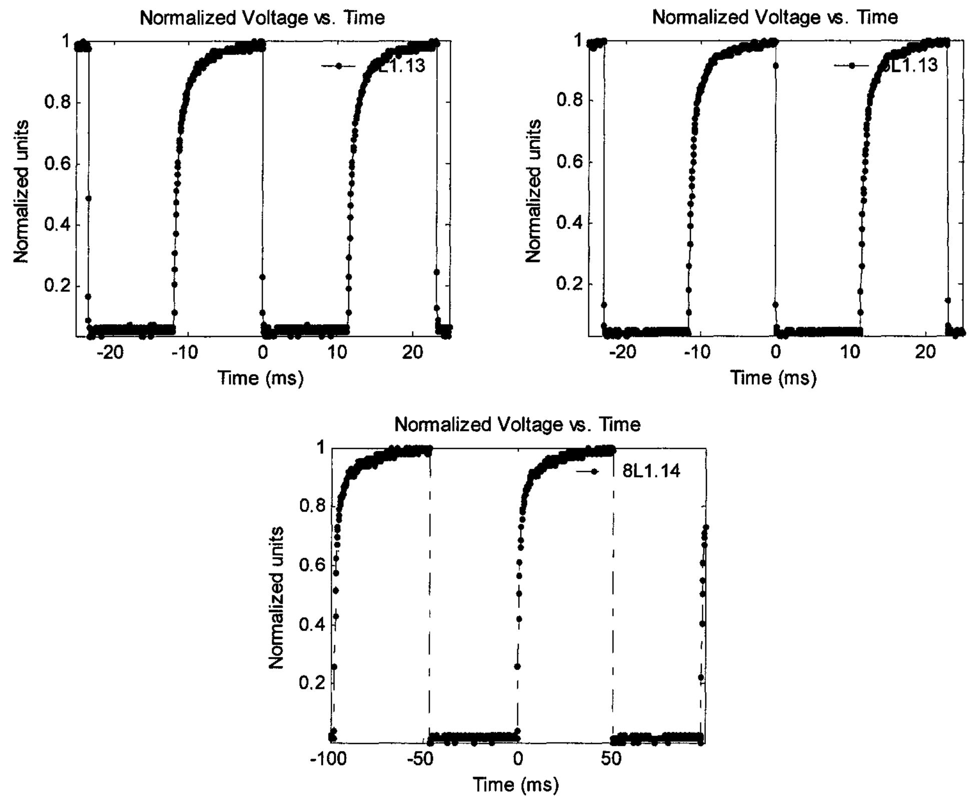

Figure 3.27: Rise time and fall time of the 4, 6 and 8μm wide waveguide for a 4.44 mm heated section.

Thermo-optic devices, as presented in the literature, usually have comparable values for rise and fall-times. It is quite surprising that, in this technology, the optical rise and fall-time have a difference of about two orders of magnitude. It is interesting to understand why this phenomenon occurs. As opposed to most other thermo-optic technologies, the heat source is located at the same location as the optical path. Upon injecting current into the waveguide, the heat does not need to diffuse very far from the source to have a significant optical impact. On the other hand, for the waveguide to cool down when the current is interrupted, heat must diffuse through the heat sink, which is a time-consuming process resulting from the constituting material properties and the waveguide's large distance from the heat sink. In summary, heating is fast but cooling is slow in these devices. If this hypothesis is true, then we would expect to have a fast optical rise-time and slow optical fall-time when the TEC is set lower than the optimum temperature and current is injected through the waveguide. Although the device's ER was poor for the reason explained in the beginning of section 3.4.2, results did support the hypothesis.

4. Thermal modeling of metal optical waveguide thermo-optic variable optical attenuator

A TO VOA was constructed and tested. From the results, modifications are suggested to improve the design's performance. Many experimental iterations can be conducted to improve the device's performance, but it is rather a slow and expensive process. In order to reduce the number of design cycles and its related costs, prediction of the structure's performance is desirable. This can be achieved by modeling the TO VOA, both, thermally and optically. The thermal model is used first since it generates results, which are subsequently used to obtain the refractive index distributions that are used in the optical model. The goal of the thermal model, in the present thesis, is to predict the temperature distribution of the TO VOA structure resulting from introducing heat into the system. More particularly, this work is focused on 2D isotropic steady-state results.

Chapter 4 is organized as follows. Section 4.1 will present the theory and the system of equation to solve. Since the solution will be found by numerical computing via a computer, the equation will be discretized . A finite difference method (FDM) formulation will be derived and solved. Numerical techniques to minimize computation time are also presented. In section 4.2, the thermal model is validated while in section 4.3 results are presented.

The particular motivation for developing a thermal model rather than using a commercial tool is purely for educational purposes. In doing so, I was able to acquire a more profound understanding of numerical methods and its use in developing a CAD tool.

4.1 Thermo-dynamic model: Theoretical background

The thermal model is based on the well-known general 3D thermal diffusion equation in integral form [43]:

$$\iiint_V Q'''_{gen} dV - \oint_S \vec{Q}'' \cdot \vec{n} dS = \iiint_V \frac{\partial (D c_p T)}{\partial t} dV \text{ [W]} \tag{4.1}$$

Q'''_{gen} is the volumetric heat generation rate (W/m^3) coming from a heat source within the control volume.The triple prime denotes a volumetric quantity. dV represents an infinitesimal volume within the volume V. Q'''_{gen} is integrated over the whole volume to determine the total power generated within the domain as shown by the left-most term of Equation (4.1). $\vec{Q}''$ is the heat flux vector (W/m^2) or equivalently, heat transfer rate per unit area, where the double prime denotes a per-unit-area quantity and the arrow indicates a vector. $\vec{n}dS$ or equivalently, $d\vec{S}$, is an infinitesimal section of the surface, S, and points outward in the direction perpendicular to the surface at that point as shown in Figure (4.1). At every point on the surface S, only the heat flux in the direction of $\vec{n}$ contributes to the power leaving the domain. This fact is represented by the dot-product of the middle term of Equation (4.1). To obtain the total amount of power leaving the volume,V, the heat flux is integrated over the whole closed surface S encapsulating the volume V. Given the conventions that $\vec{n}$ points outward and that the power leaving the control volume is negative, a negative sign is placed in front the middle term of Equation (4.1). The right hand term of Equation (4.1) represents the amount of power stored within the volume V. It is composed of the variables "D", c_p, "T" and "t" which are the density (kg/m^3), the heat capacity (J/(kg.K)), the temperature (K) and time (s) respectively.

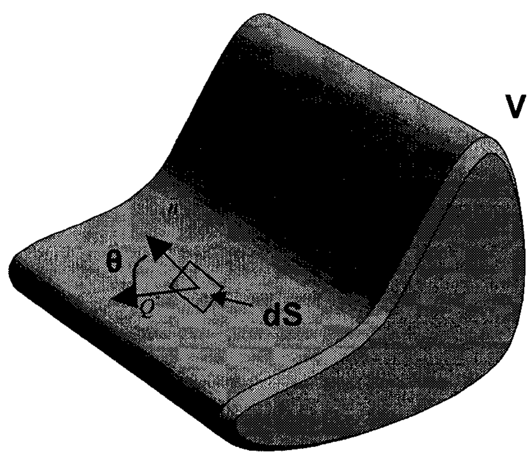

Figure 4.1: Heat flux coming out of the surface of an arbitrary volume.

The interpretation of this equation is that "the total thermal and mechanical power entering a control volume, plus the thermal power generated within the control volume, minus the thermal and mechanical power leaving the control volume must equal the power stored within the control volume" [44]. Hence, it is an equation that satisfies the conservation of power.

In order to simplify Equation (4.1), assumptions are made. As stated earlier, the focus is to generate steady-state results. When the device reaches steady-state, the temperature distribution becomes invariant with respect to time. Therefore, the term on the right of Equation (4.1) vanishes. The TO VOA was constructed by depositing a few layers of materials. The system is inhomogeneous and it is expected that thermal properties will change in each layer. Furthermore, materials with isotropic thermal properties were chosen such that tensors are not necessary to describe material properties. A Cartesian coordinate system was chosen since it is compatible with the geometry of the TO VOA structure proposed in earlier chapters. The heat source, the metal optical waveguide, is very long in comparison to its thickness and width; therefore, its thermal results should match closely those of a source infinitely long. For this reason, a 2D model will be used to simplify the problem and reduce computation time. Q'''_{gen} is produced by heating the metal optical waveguide via ohmic losses by injecting a current through it. It can be defined as:

$$Q'''_{gen} = \frac{J^2}{\sigma} \text{ [W/m}^3\text{]} \tag{4.2}$$

where J and σ are the current density (A/m^2) injected in the metal optical waveguide and electrical conductivity ($(\Omega.\text{m})^{-1}$) of the metal, respectively. Also, $\vec{Q}''$ presented earlier is described by the phenomenological equation [43]:

$$\vec{Q}'' = -K\overrightarrow{\nabla T} \text{ [W/m}^2\text{]} \tag{4.3}$$

where "K" is the thermal conductivity (W/(m.K)) of the material. Using these assumptions and replacing the appropriate variables in (4.1) by the Equations (4.2-4.3) we obtain:

$$\iint_S \frac{J^2}{\sigma} dS + \oint_C \left(K\overrightarrow{\nabla T}\right)\cdot \vec{n} dC = 0 \text{ [W]} \tag{4.4}$$

Equation (4.4) is the 2D isotropic steady-state heat diffusion equation in integral form. The volume integral becomes a surface integral while the integral over a closed surface becomes the integral over a closed curve.

Heat diffusion can often be compared to an equivalent electrical system. Using this analogy, heat flux has a more physical meaning and simplifies the thought process for future derivation. Here are different ways representing the heat flux:

$$\vec{Q}'' = -K\overrightarrow{\nabla T} \Rightarrow Q_n'' = -K\frac{\partial T}{\partial n} \Rightarrow Q_n = -KA\frac{\partial T}{\partial n} \tag{4.5}$$

where $\vec{Q}''$, Q_n, "k" and "A" represents the power flux density, the power flux along direction $\vec{n}$, the thermal conductivity and the cross sectional area considered respectively. ∂n is an infinitesimal distance in the direction $\vec{n}$.The last equation to the right resembles ohms law:

$$I = \frac{V}{R_E} \Rightarrow Q_n = \frac{-KA}{\partial n}\partial T \tag{4.6}$$

where Q_n, ∂T and $\left(\frac{KA}{\partial n}\right)^{-1}$ are equivalent to the current, I, voltage, V, and electrical resistance, R_E, respectively. Hence, it is sensible to define a thermal resistance, R_T as:

$$R_T = \frac{\partial n}{KA} \text{ [K/W]} \tag{4.7}$$

such that:

$$Q_n = -\frac{\partial T}{R_T} \text{ [W]} \tag{4.8}$$

where part of the differential operator, ∂n, is hidden in R_T.

Given a structure made of various materials, it is possible to determine its effective thermal resistance between two points in a similar manner than that of an electrical circuit by combining series and parallel resistances. This notion will be used in the next section.

4.2 Finite difference method formulation

Given the complexity of Equation (4.4), it cannot be solved analytically, but can be solved numerically. All variables constituting Equation (4.4) must be discretized in space. In particular, a FDM will be used. The discretization process will be explained in this section.

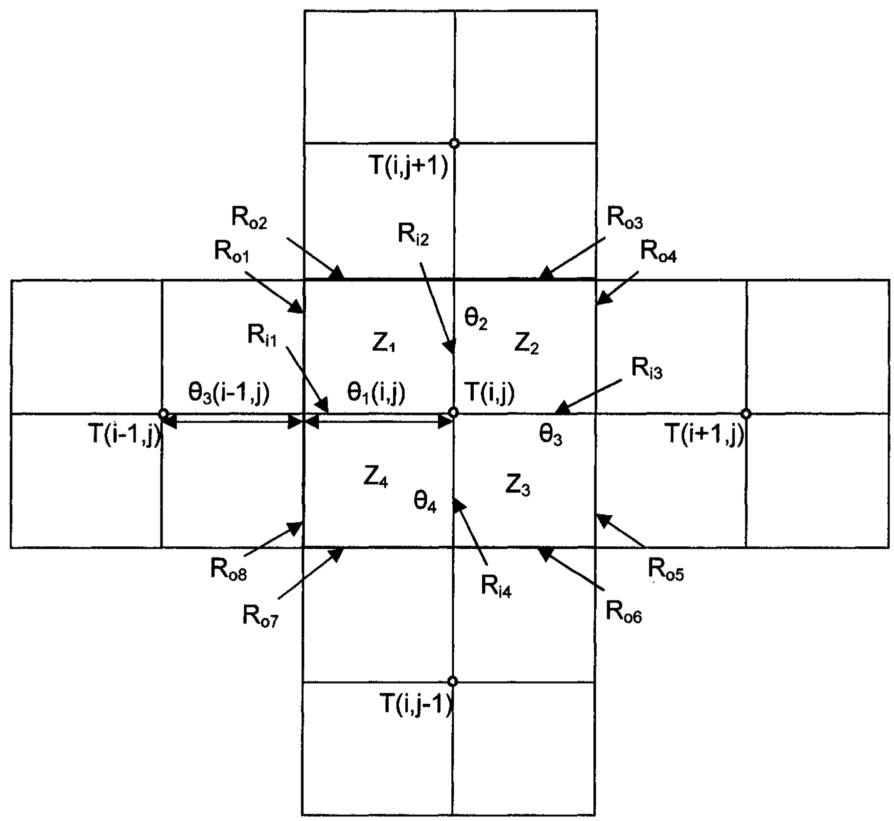

Figure 4.2: Illustration of the infinitesimal discretized space from which the discretized thermal diffusion equations will be derived. It contains thermal resistance, contact resistance, node separation and material properties associated to each node.

Figure (4.2) is used to illustrate the situation from which the discretized thermal diffusion equation will be derived. It shows an infinitesimal region of space where the conservation of power may be applied. The Cartesian coordinate system is discretized into a 2D mesh represented by nodes (i,j) . Each node has spatial coordinates, $(x(i,j), y(i,j))$ or simply (x,y) and temperature T(i,j) associated with it where T is the average temperature within the rectangular area. Each node (i,j) is encapsulated by a rectangular area. The rectangular area is itself subdivided into quadrants where the node lies at the quadrants' common vertices. Each quadrant has its own set of thermal properties representing the fact that the material properties may change from one quadrant to the next. In Figure (4.2), this is shown as Z_n where "n" may take a value from 1 to 4. Z represents all three parameters of the material: K, J or σ where each parameter is associated with its respective quadrant and node. R_{i1} through R_{i4} and R_{o1} through R_{o8} are contact resistances, which occur when two or more materials are joined together. The node, (i,j), is surrounded by four neighboring nodes on the left, right, up and down denoted by (i-1,j), (i+1,j), (i,j+1), (i,j-1) respectively. These nodes are illustrated since they are relevant to the derivation. Only the variables in the quadrants of the middle node are shown in the figure, but they nonetheless exist for the other nodes. The separation between T(i-1,j) and T(i,j) is $h(\theta_3(i-1,j)+\theta_1(i,j))$ as shown in Figure (4.2) where the distance, "h", is modified by the weighing factor θ_3 and θ_1. The weighing factors enable the possibility of using a non-uniform mesh. The reason for using non-uniform meshes will become apparent in the next section. In order to have a pattern of rectangular areas discretizing the Cartesian coordinate system, one may quickly realize that $\theta_2(i,j)=\theta_2(i\pm n,j)$, $\theta_4(i,j)=\theta_4(i\pm n,j)$, $\theta_3(i,j)=\theta_3(i,j\pm n)$ and $\theta_1(i,j)=\theta_1(i,j\pm n)$ must hold where n is any positive integer.

In the particular case represented by Figure (4.2) , Equation (4.4) becomes:

$$\iint_S \frac{J^2}{\sigma} dS - \left(Q_{-x} + Q_{+y} + Q_{+x} + Q_{-y}\right) = 0 \tag{4.9}$$

where $Q_{-x} + Q_{+y} + Q_{+x} + Q_{-y} = \oint_S \vec{Q} \cdot \vec{n} dS$. Q_{-x}, Q_{+y}, Q_{+x} and Q_{-y} are the heat fluxes leaving the rectangular control area by crossing the left vertical wall between node (i,j) towards (i-1,j), the same through the horizontal wall between node (i,j) towards (i,j+1), the same through the vertical wall between node (i,j) towards (i+1,j) and the same through the horizontal wall between node (i,j) towards (i,j-1) respectively. Each Q in Equation (4.9) is of the form of Equation (4.8) and its differential operator must be discretized. All differential operators in the continuous domain are transformed to finite-difference operators in the discretised domain.

Discretizing the differential operator involves an approximation. The Taylor series of a function f(x) provides an effective means for constructing finite-difference approximations of a desired accuracy for differentials of any order [45]. The Taylor series of a function f(x) about the point "a" is given by:

$$f(x) = \sum_{k=0}^{\infty} \frac{f^{(k)}(a)(x-a)^k}{k!} \tag{4.10}$$

The domain may be discretized into equal intervals $x_{i\pm n} - x_i = \pm nH$ where "a" become x_i and the taylor series in discretized form yields

$$f(x_{i\pm n}) = \sum_{k=0}^{\infty} \frac{f^{(k)}(x_i)(\pm nH)^k}{k!} \tag{4.11}$$

The taylor series shown below is for x_{i+1} and x_{i-1}.

$$f(x_{i+1}) = f(x_i) + f'(x_i)H + \frac{f''(x_i)H^2}{2!} + \frac{f'''(x_i)H^3}{3!} + O(H^4) \tag{4.12}$$

$$f(x_{i-1}) = f(x_i) - f'(x_i)H + \frac{f''(x_i)H^2}{2!} - \frac{f'''(x_i)H^3}{3!} + O(H^4) \tag{4.13}$$

where the terms with H of order higher than 3 are dropped. This leads to an approximation error of order H^4. This is represented by $O(H^4)$ in Equations (4.12) and (4.13).

When $f'(x_i)$ is isolated in Equation (4.12) and (4.13) and terms of order H^2 or higher are ignored. The forward (4.14) and backward (4.15) finite difference approximation, respectively, are obtained:

$$f'(x_i) = \frac{f(x_{i+1}) - f(x_i)}{H} + O(H) \tag{4.14}$$

$$f'(x_i) = \frac{f(x_i) - f(x_{i-1})}{H} + O(H) \tag{4.15}$$

where the error of the approximation in each equation is of order H. In (4.14), the derivative at node x_i is determined from "f" at x_{i+1} and x_i, while for (4.15), the derivative at node x_i is determined from "f" at x_i and x_{i-1}. By substracting Equation (4.13) from (4.12) and isolating $f'(x_i)$ we get:

$$f'(x_i) = \frac{f(x_{i+1}) - f(x_{i-1})}{2H} + O(H^2) \tag{4.16}$$

which is the central difference with error of order H^2. In (4.16), the derivative at node x_i is determined from its adjacent nodes x_{i+1} and x_{i-1}. Now, imagine that there exist a node $i+\frac{1}{2}$ between i and i+1. Using 4.16, node i, node i+1, and replacing h by h/2, we get the central difference for a derivative at $i+\frac{1}{2}$:

$$f'(x_{i+\frac{1}{2}}) = \frac{f(x_{i+1}) - f(x_i)}{H} + O(H^2) \tag{4.17}$$

where the error is of order H^2. The only difference between (4.14) and (4.17) is that the derivative of (4.17) is determined between nodes and its order is H^2 rather than H. Doing the same between i and i-1, we get:

$$f'(x_{i-\frac{1}{2}}) = \frac{f(x_i) - f(x_{i-1})}{H} + O(H^2) \tag{4.18}$$

It is desirable to have a simple approximation but accurate representation of the differential operator. Equations (4.16), (4.17) and (4.18) seem to be good choices since they are rather simple and are of order $O(H^2)$. In Figure (4.2) $Q_{\pm x, \pm y}$ are always evaluated between their respective nodes (at the rectangular segments). In order for Q to be evaluated simply and accurately the following parameters are set to: $\theta_3(i\text{-}1,j)=\theta_1(i,j)$, $\theta_4(i,j+1)=\theta_2(i,j)$, $\theta_1(i+1,j)=\theta_3(i,j)$ and $\theta_2(i,j\text{-}1)=\theta_4(i,j)$ throughout space. This means that Q is evaluated in the middle between its respective nodes or equivalently at $i \pm \frac{1}{2}$ or $j \pm \frac{1}{2}$ in the x or y dimension respectively. Therefore, Equation (4.17) or (4.18) may be used in conjunction with (4.8) for the Q's in (4.9):

$$Q_{-x}(i-1/2, j) = -\frac{\partial T}{R_{tot-x}} \cong -\frac{T(i,j) - T(i-1,j)}{R_{tot-x}} \tag{4.19}$$

$$Q_{+y}(i, j+1/2) = -\frac{\partial T}{R_{tot+y}} \cong -\frac{T(i,j+1) - T(i,j)}{R_{tot+y}} \tag{4.20}$$

$$Q_{+x}(i+1/2, j) = -\frac{\partial T}{R_{tot+x}} \cong -\frac{T(i+1,j) - T(i,j)}{R_{tot+x}} \tag{4.21}$$

$$Q_{-y}(i, j-1/2) = -\frac{\partial T}{R_{tot-y}} \cong -\frac{T(i,j) - T(i,j-1)}{R_{tot-y}} \tag{4.22}$$

where the "∂n "hidden in each "R" becomes the distance between the two corresponding nodes. R_{tot-x}, R_{tot+y}, R_{tot+x},R_{tot-y} are the total effective thermal resistances between node (i,j) and (i-1,j), node (i,j) and (i,j+1), node (i,j) and (i+1,j) and node (i,j) and (i,j-1) respectively. Figure (4.3) represents the thermal resistance model of Figure (4.2) for R_{tot-x}. The other thermal resistances are determined in a similar way.

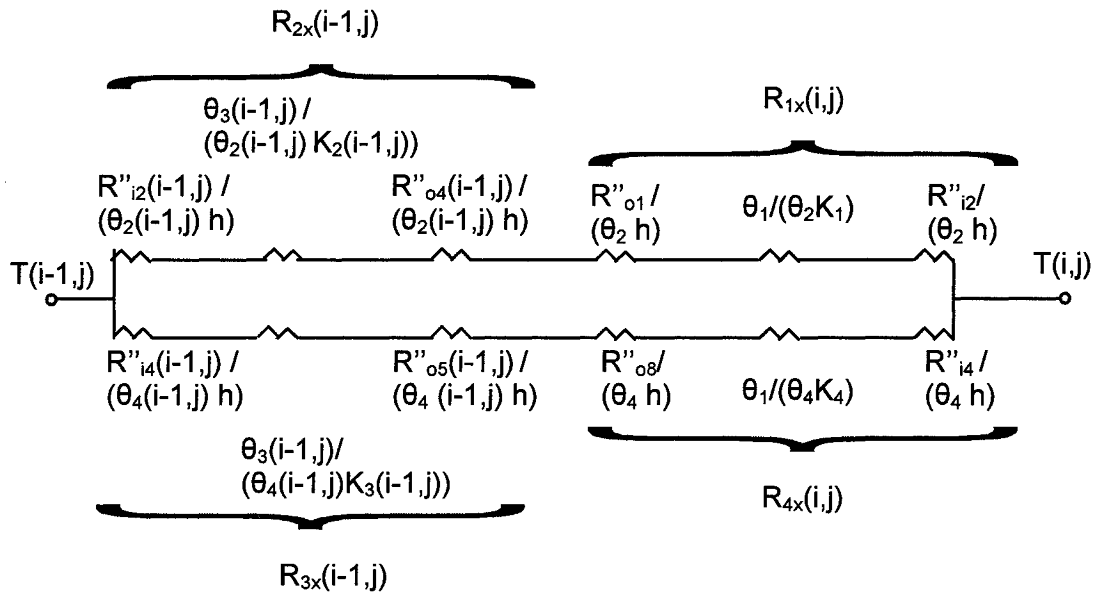

Figure 4.3: Complete thermal resitance model between the node (i-1,j) and (i,j).

In Figure 4.3, $R''_{o4}(i-1,j) = R''_{o1}(i,j)$ and $R''_{o5}(i-1,j) = R''_{o8}(i,j)$ since it is assumed that the vertical interface separating the quadrants falls directly in the middle of the contact resistance. The double prime on the contact resistance denotes a per-unit area value. For the same reason $R''_{i2}(i,j)$, $R''_{i2}(i-1,j)$, $R''_{i4}(i,j)$ and $R''_{i4}(i-1,j)$ represented in Figure (4.2) and (4.3) are only half of the total contact resistance. The resistance $R_{1x}(i,j)$, $R_{4x}(i,j)$, $R_{2x}(i-1,j)$ and $R_{3x}(i-1,j)$ shown in Figure (4.3) represent the individual thermal resistance contributions from each involved quadrants in R_{tot-x}. $R_{tot-x}=(R_{4x}(i,j) // R_{1x}(i,j)) + (R_{2x}(i-1,j)) // (R_{3x}(i-1,j))$ where the symbol "//" denote a parallel configuration. A similar derivation could be applied for R_{tot+y}, R_{tot+x} and R_{tot-y}. The resulting equations are:

$$R_{1x} = \frac{1}{\theta_2}\left[\frac{\theta_1}{K_1} + \frac{R''_{o1} + R''_{i2}}{h}\right] \quad (4.23)$$

$$R_{1y} = \frac{1}{\theta_1}\left[\frac{\theta_2}{K_1} + \frac{R''_{o2} + R''_{i1}}{h}\right] \quad (4.24)$$

$$R_{2x} = \frac{1}{\theta_2}\left[\frac{\theta_3}{K_2} + \frac{R''_{o4} + R''_{i2}}{h}\right] \quad (4.25)$$

$$R_{2y} = \frac{1}{\theta_3}\left[\frac{\theta_2}{K_2} + \frac{R''_{o3} + R''_{i3}}{h}\right] \quad (4.26)$$

$$R_{3x} = \frac{1}{\theta_4}\left[\frac{\theta_3}{K_3} + \frac{R''_{o5} + R''_{i4}}{h}\right] \quad (4.27)$$

$$R_{3y} = \frac{1}{\theta_3}\left[\frac{\theta_4}{K_3} + \frac{R''_{o6} + R''_{i3}}{h}\right] \quad (4.28)$$

$$R_{4x} = \frac{1}{\theta_4}\left[\frac{\theta_1}{K_4} + \frac{R''_{o8} + R''_{i4}}{h}\right] \quad (4.29) \qquad R_{4y} = \frac{1}{\theta_1}\left[\frac{\theta_4}{K_4} + \frac{R''_{o7} + R''_{i1}}{h}\right] \quad (4.30)$$

$$R_{tot\text{-}x} = (R_{4x}(i,j) \mathbin{//} R_{1x}(i,j)) + (R_{2x}(i-1,j)) \mathbin{//} (R_{3x}(i-1,j)) = 1/A \qquad (4.31)$$

$$R_{tot+y} = (R_{1y}(i,j) \mathbin{//} R_{2y}(i,j)) + (R_{3y}(i,j+1)) \mathbin{//} (R_{4y}(i,j+1)) = 1/B \qquad (4.32)$$

$$R_{tot+x} = (R_{2x}(i,j) \mathbin{//} R_{3x}(i,j)) + (R_{4x}(i+1,j)) \mathbin{//} (R_{1x}(i+1,j)) = 1/C \qquad (4.33)$$

$$R_{tot\text{-}y} = (R_{3y}(i,j) \mathbin{//} R_{4y}(i,j)) + (R_{1y}(i,j-1)) \mathbin{//} (R_{2y}(i,j-1)) = 1/D \qquad (4.34)$$

Finally, the left-most term of Equation (4.9) is discretized by integrating the power density generated over the infinitesimal area:

$$Q_G = \iint_S \frac{J^2}{\sigma} dS \Rightarrow h^2\left[\theta_1\left(\theta_2 \frac{J_1^2}{\sigma_1} + \theta_4 \frac{J_4^2}{\sigma_4}\right) + \theta_3\left(\theta_2 \frac{J_2^2}{\sigma_2} + \theta_4 \frac{J_3^2}{\sigma_3}\right)\right] \qquad (4.35)$$

In Equation (4.35), J_1 through J_4 is the average current density injected within its respective quadrant. Equations (4.31) to (4.34) are substituted in conjunction with (4.19) to (4.22) into (4.9) and T(i,j) is isolated; thus we obtain:

$$T(i,j) = \frac{T(i-1,j)A + T(i,j+1)B + T(i+1,j)C + T(i,j-1)D + Q_G(i,j)}{A+B+C+D} \qquad (4.36)$$

The thermal simulator is written from these principles.

The domain of computation cannot be infinitely large given the limited resources of the computer. At the edge of the domain, boundary conditions are set. There are three common types of boundary conditions. The first kind consists of setting the boundary at a fixed temperature. The second kind consists of fixing the heat flux. The final kind is a convective boundary condition where the heat conduction equals the heat convected by the fluid at the boundary.

In the TO VOA presented in earlier chapters, the prototype is a very large structure surrounded by air and placed on a heat sink. The top of the structure is bounded by air. Air is a very good thermal insulator if conduction is the only heat transfer mechanism. This is assumed the case for the TO VOA structure presented in earlier chapters. This assumption will be proven a good approximation in later sections. For this reason, the top boundary is a boundary of the second kind where the heat flux is set to zero or is adiabatic. In fact, given the particular geometry of the structure, the temperature of the waveguide was proven quite insensitive to the type of boundary condition of the top boundary [22].

Since the device sits on a heat sink, the bottom of the sample should be very close to the ambient temperature. From the superposition principle, it is possible to remove the ambient temperature offset of the result and set the bottom boundary to 0 K. In doing so, results generated by the thermal model will be seen as the temperature increase due to heating the metal optical waveguide. The bottom boundary is of the first kind.

The TO VOA has thermal half symmetry where the axis of symmetry is located at the vertical center of the waveguide. Because of thermal half symmetry of the structure, there is no heat flux crossing the vertical center of the waveguide. As a result, an adiabatic boundary condition can be set at the vertical center of the waveguide. Hence, only half of the domain can be computed to obtain the results of the full domain. The structure is assumed infinitely wide, but for computing purposes, an adiabatic boundary condition is set far away from the heat source such that it has little impact on the results. An adiabatic boundary condition can be interpreted as an infinite thermal resistance. For this reason, the adiabatic boundary condition is implemented by setting the corresponding R_{tot} in from Equation (4.31) to (4.34) to infinity or equivalently by setting the corresponding variables A, B, C or D to zero in Equation (4.36).

Equation (4.36) can be written in matrix form for all nodes in the computational domain and the system can be solved exactly (except for numerical truncation) by matrix inversion. Equation (4.36) can also be calculated for each nodes of the domain iteratively until the desired accuracy is obtained. The first method seems to be the best one, but for a domain with a large quantity of nodes, inversion of matrix can take a significant amount of time. On the other hand, within a given tolerance, the iterative method will generate results more quickly than the other method for large quantity of nodes. Therefore, the latter method was chosen. In order to obtain the temperature profile generated by the waveguide heater, Equation (4.36) is calculated for each point (i,j) in the domain. To begin the calculations, T(i,j) is set to 0 in the whole domain. The grid is computed iteratively until the desired accuracy is achieved. The condition for which the computation ends can take many forms. A simple choice is to apply the conservation of power over all the domain of computation in a similar way than that was done for the infinitesimal region shown in Figure (4.2). Equation

(4.9) represents this situation except that the power flux is taken at the boundary of the domain of computation. The iterative method is summarized by Equation (4.37):

$$Q_G - (Q_{-x}^k + Q_{+y}^k + Q_{+x}^k + Q_{-y}^k) = \Lambda^k \tag{4.37}$$

where Q_G is a value set by the amount of power inserted into the system. The superscript k represents the iteration number. Λ^k represents the deviation from the steady-state condition. As "k" tends to infinity Λ^k vanishes and, under that condition, (4.37) generates the true steady-state solution. A condition for which computations may be stopped is:

$$\left|\frac{\Lambda^k}{Q_G}\right| \leq \Psi \tag{4.38}$$

where Ψ is chosen between 0 and 1 inclusively, but should be chosen to be very small in order to obtain accurate results.

The domain of computation cannot be infinitely large since the resources of a computer are not unlimited. Furthermore, computation time depends on the size of the problem. Hence, the domain of calculation is set to be as small as possible to minimize computation time, but not so small as to perturb the results significantly. In order to obtain accurate thermal simulations, it is necessary that at least a few points lye along the thickness and width the waveguide heater. Given the small size of the waveguide heater in comparison to the minimized computational domain, the number of points required to cover the domain adequately is quite significant; therefore, computation time is not negligible. Computation time can be reduced further as discussed in Appendix C (Gauss-Siedel method, successive overrelaxation method (SOR), non-uniform meshes and multigrids). Also, because the problem has half symmetry, only half of the domain is computed as explained in Appendix C.

Most of the thermal model was implemented in FORTRAN. However, the non-uniform mesh was generated by using Matlab.

4.3 Validation

There are many steps to validate the thermal simulation. In the previous section, the side, middle and top boundary condition were set to be adiabatic. The top and side boundaries were set far enough from the source to not influence the results significantly.

"Far enough" is arbitrary and must be determined numerically. The side and top boundary were set far and results were obtained. Each boundary was then independently successively brought closer each with its own set of results. It is only when the results start to change more than by a given tolerance that the minimum boundary distance is determined. Next, results are determined as a function of mesh density to determine the convergence of the results. The mesh is non-uniform, so to increase the mesh density, the number of points inside the waveguide is increased and the spacing near the boundary is set smaller. With theses changes, our mesh-generating algorithm explained in Appendix B based on Equations (B.6) to (B.8) automatically generates a denser mesh.

In order to validate the thermal simulations, a structure was simulated via the commercial simulator ANSYS. Results from the present model were obtained and compared to those generated by ANSYS for the same structure [22]. The simulations provided by ANSYS are based on the finite element method. The structure consists of 10μm of silicon over which is placed 15μm of silica and 15μm of polymer respectively. The gold metal waveguide was 20nm thick and 8μm wide. The silicon has a thermal conductivity of $145\frac{W}{m.K}$, silica, $1.4\frac{W}{m.K}$, polymer, $0.11\frac{W}{m.K}$ and gold $298\frac{W}{m.K}$. The electrical conductivity of gold was $4.1*10^7\ (\Omega.m)^{-1}$. An electrical power of 9.756mW/mm was dissipated by the waveguide to generate heat. The result of the FDM simulation is shown in Figure 4.5. In order to compare both results, we subtracted them to observe the difference in temperature provided by both simulations. This is shown in Figure 4.6 where the largest difference in temperature is located at the edges of the waveguide and is of about 0.1°C. The node distribution of both methods is quite different, so to compare both simulations, we had to use a linear interpolation to obtain the temperature at the same node positions, which contributes to the error. Most of the error, though, is less than 0.06°C, which is very small compared to the maximum increase of temperature of the waveguide. Our simulations are deemed valid considering that the two numerical methods are different.

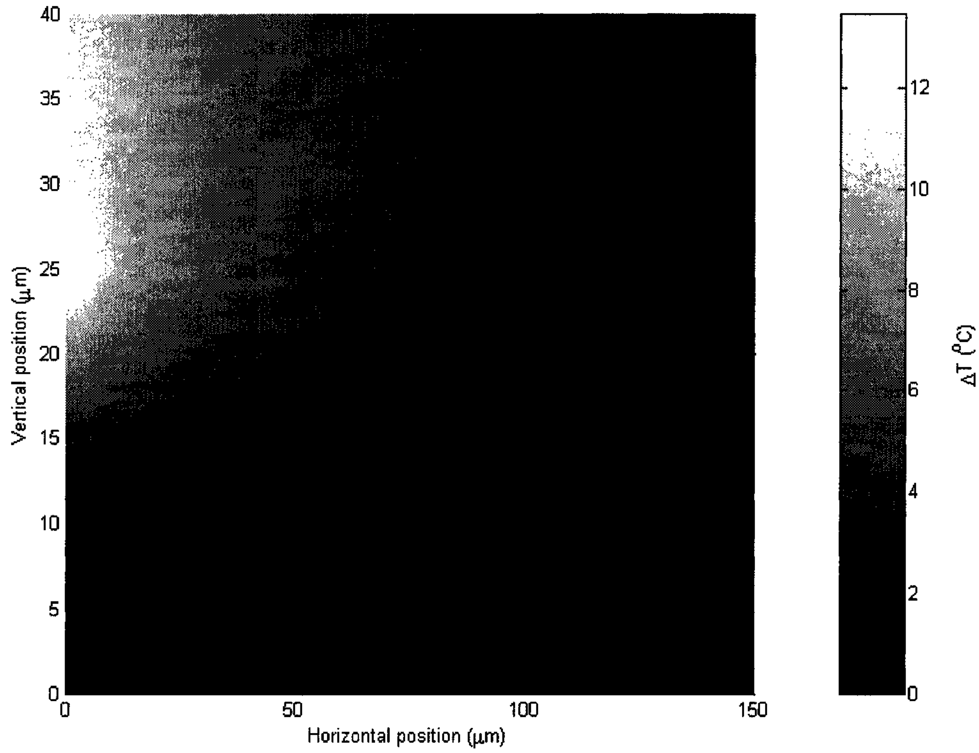

Figure 4.4: Increase of temperature of the waveguide for an applied electrical power of 9.756 W/mm.

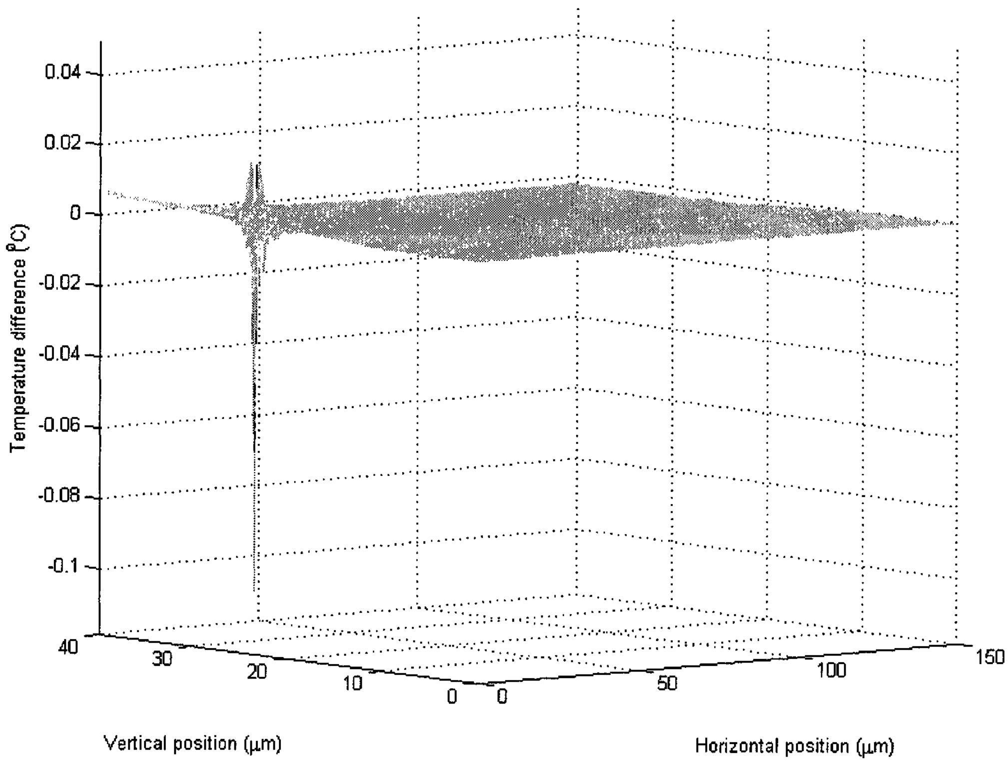

Figure 4.5: Difference of temperature between the results provided by ANSYS and the present work.

4.4 Results

In the previous sections, the thermal model was derived and validated. The results of the thermal simulation are presented in this section along with the refractive index distribution resulting from heating the waveguide.

The structure simulated and their material properties are similar than described in section 3.1. As explained in the earlier section, adiabatic boundary conditions were set at three out of the four sides of the computational domain where one of them is set at the vertical center of the waveguide. The temperature of the heat sink was set to 0 K due to the superposition principle as explained in the previous section. It suffices to add the ambient temperature to the results obtained by the thermal model to get the real temperature expected in the experiments.

From bottom to top, the structure includes 10μm of silicon, 15μm of silica, a gold waveguide 15nm thick and 8μm wide and polymer 125.85μm thick. The polymer and silica layers are not as thick as that present in the laboratory, but it makes simulations quicker with negligible differences in the results. Therefore, the whole structure is 150μm thick. Refer to section 3.1 for the material properties.

Figure 4.6 presents the temperature increase resulting from heating the various waveguides by injecting a current density of 66.66 GA/m^2 (or 9.756mW/mm), which was the maximum current density used in the experiments. Figure 4.6 (a), (b) and (c) show the temperature as a function as the cross sectional position for the 8, 6 and 4μm wide waveguides, respectively. Only the solution of half of the full domain is shown because of thermal half symmetry. The waveguide is located at a vertical position of 25μm. Figure 4.6 (d) is the temperature along the horizontal center of each waveguides. As can be seen in (d), the average temperature in the metal waveguide is about 32°C, 28°C and 22°C for the 8, 6 and 4μm wide waveguides, respectively. It also shows that the temperature of the waveguide is not constant within. There is a difference of about 7°C between the experimental results and the simulations, which is quite significant. This suggests that the material properties obtained from the literature could be quite different from that of the actual structure. Since the refractive index distribution is based on those results, it will also have repercussions on the optical simulations.

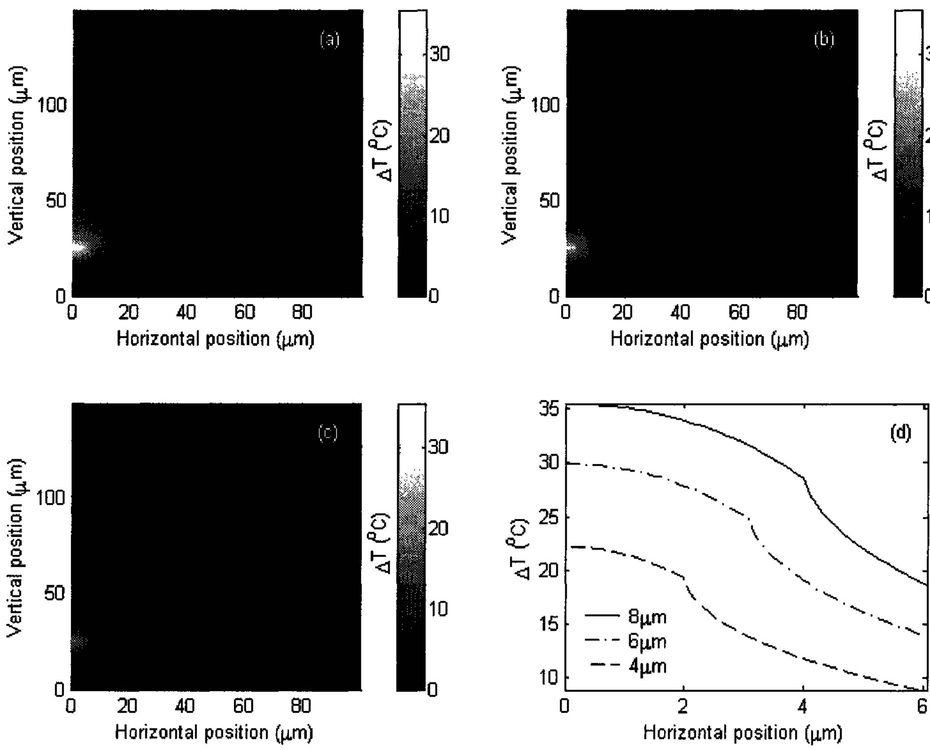

Figure 4.6: Increase of temperature of the 8, 6 and 4μm waveguide for an injected current density of 66.6 GA/m^2. (a), (b) and (c) are associated with the 8, 6 and 4μm waveguide, respectively. (d) is the temperature taken along the horizontal center of each waveguide.

The optical simulations that are conducted in Chapter 5 are 1D. For this reason, the temperature along the vertical center of the waveguide was used to obtain the refractive index profile, which will be used in the optical simulator. Figure 4.7 shows the temperature distribution along the vertical center of the waveguide as a function of injected current density. Finally, Figure 4.8 shows the refractive index distribution as a function of applied current density.

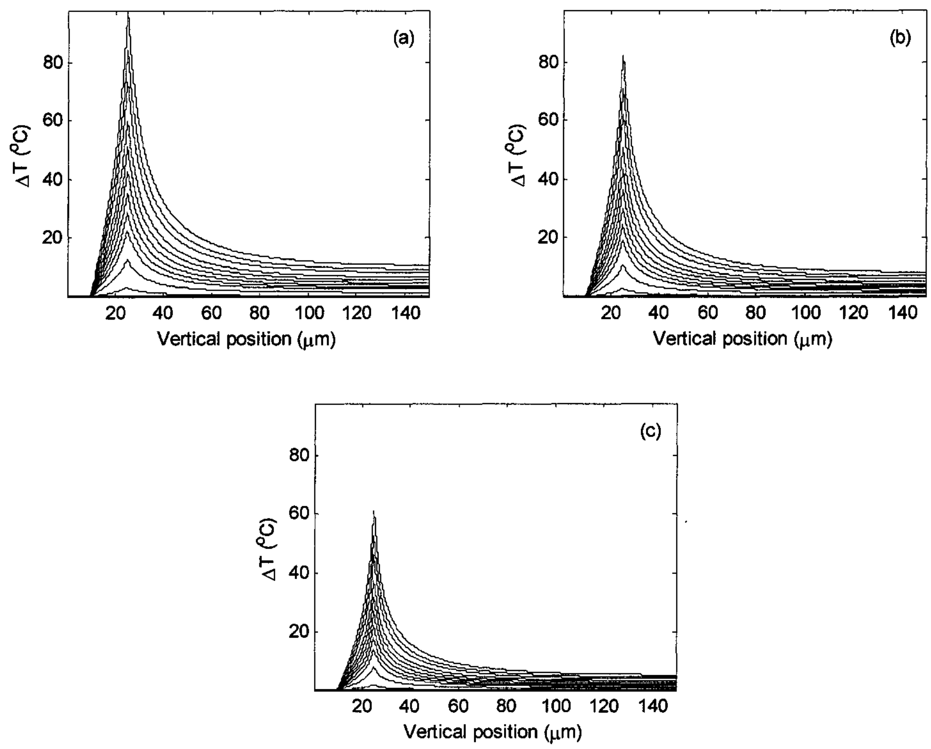

Figure 4.7: Increase of temperature along the vertical center of the waveguides as a function of injected current density. (a), (b) and (c) are associated with the 8, 6 and 4μm wide waveguides respectively. As the current density increases, the temperature also increases. The metal core of the waveguide is located at a vertical position of 25μm.The current densities are: 1.3, 20, 40, 53.3, 60, 66.6, 73.3, 80, 86.66, 96, 102.6 and 110.6 GA/m^2 respectively. The temperature profile associate to 1.3GA/m^2 is almost flat and is not visible in the figures.

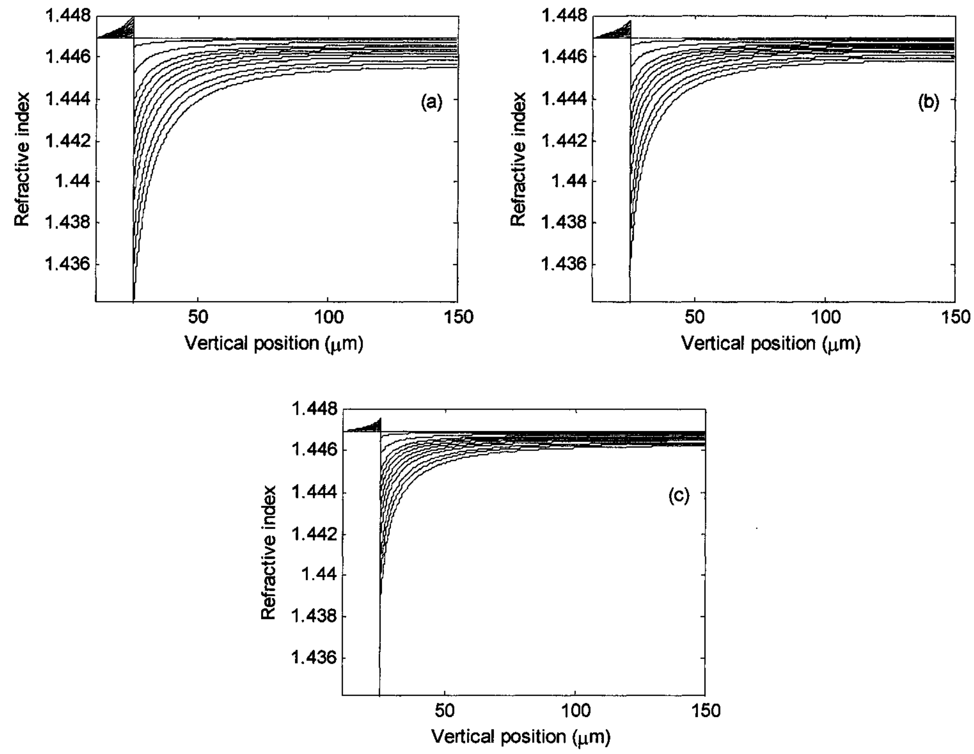

Figure 4.8: Refractive index along the vertical center of the 8, 6 and 4μm wide waveguides as a function of injected current density. (a), (b) and (c) are associated with the 8, 6 and 4μm wide waveguides, respectively. As the current density increases, the refractive index increases for the silica and reduces for the polymer. The metal core of the waveguide is located at a vertical position of 25μm. The current densities are: 1.3, 20, 40, 53.3, 60, 66.6, 73.3, 80, 86.66, 96, 102.6 and 110.6 GA/m^2 respectively.

5. Optical modeling of metal optical waveguide thermo-optic variable optical attenuator

To determine how light is propagating along the metal waveguide, a 3D optical model such as beam propagation method (BPM) could be used to generate results, but it is very computationally intensive given the small size of the waveguide in relation to the domain of computation. Also, BPM has never been developed for metal waveguides. Given that variations in the longitudinal direction are usually small, a 2D optical simulation should approximate the 3D situation rather well. Furthermore, it is of interest to see if such a situation could be approximated with a 1D model, because it could substantially reduce computation time. If such an approximation is deemed acceptable, it could be used to quickly estimate the behavior of simple structures.

The first goal of this chapter is to model a metal slab structure optically and validate it by comparisons with other authors. Subsequently, the waveguide that was analyzed in the laboratory presented in chapter 3 will be approximated by a 1D optical model. In particular, a modal analysis is conducted and results are obtained for the s_b and s_L modes. It is assumed that most of the power is contained within those modes due to the rather good mode overlap with the end-fire excitation of a PMF. Results will be presented, discussed and compared to those generated in the laboratory such that we can determine if the above assumptions and approximations are acceptable.

The thermal simulations of the previous chapter were useful to determine the refractive index profile surrounding the waveguide heater. Next, the refractive index profile will be used in optical simulations to determine the optical performance of the VOA. The theory surrounding the simulations of the metal optical waveguide has already been presented in detail in reference [20], but due to its importance and slight differences, it will be incorporated herein.

5.1 Derivation of the dispersion equation for a thin metal film slab

In order to determine the modes supported by the 1D thin metal film structure (or slab), Maxwell's equations are solved satisfying appropriate boundary conditions. Maxwell's equations are defined in a right-hand Cartesian coordinate system where propagation occurs in the +x direction along the metal film. In the present work the metal waveguide is made of gold, which is a non-magnetic material (μ_r=1). As was explained earlier a non-magnetic thin metal film supports purely TM modes only [7]. Furthermore, given purely TM modes and the convention defined above, only E_x, E_z and H_y field components exist. Because of the nature of the numerical method used to solve the problem, the z-dependence of the permittivity can be removed since the inhomogeneity along "z" is treated by dividing the structure into a number of layers that are homogeneous along this direction, and suitable boundary conditions are applied between them. The situation is illustrated in Figure 5.1.

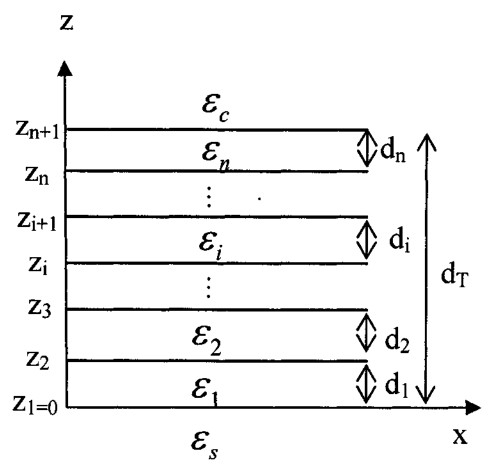

Figure 5.1: Multilayer structure from which the 1D optical model is derived.

In Figure 5.1, "z" denotes the various positions of each interface separating the layers where the subscript "i" indicates the layer number. The letter "d" represents the layer thickness and d_T is the total thickness of the structure. "s" and "c" represent the lower semi-infinite medium or substrate and upper semi-infinite medium or cover, respectively. It is assumed that the modal solutions take the form:

$$\vec{H}_i(x,z) = \hat{y}H_{y_i}(z)H_{y_i}(x) = \hat{y}\,H_{y_i}(z)\;e^{j(\omega t - k_x x)} \tag{5.1}$$

$$\vec{E}_i(x,z) = \left[\hat{x}\,E_{x_i}(z) + \hat{z}\,E_{z_i}(z)\right]E_i(x) = \left[\hat{x}\,E_{x_i}(z) + \hat{z}\,E_{z_i}(z)\right]e^{j(\omega t - k_x x)} \tag{5.2}$$

where $\vec{H}_i(x,z)$ and $\vec{E}_i(x,z)$ are dependent on "x" and "z". Because it is assumed that "x" and "z" are not interdependent, Equation (5.1) is composed of its individual "x" and "z" dependency: $H_{y_i}(x)$ and $H_{y_i}(z)$ respectively. A similar situation occurs for Equation (5.2). Given the 1D model and direction of propagation of the wave, there can only be x and z dependencies; hence, $\frac{\partial}{\partial y} = 0$. Maxwell's equations in a general isotropic linear homogeneous non-magnetic medium in phasor form are:

$$\nabla \times \vec{H}_i = j\omega\varepsilon_0\varepsilon_{r_i}\vec{E}_i + \vec{J}_{Ii} = \frac{jk_i^2}{\omega\mu_0}\vec{E}_i + \vec{J}_{Ii} \tag{5.3}$$

$$\nabla \times \vec{E}_i = -\, j\omega\mu_0\vec{H}_i \tag{5.4}$$

where the parameters ε_{r_i}, and k_i^2 may be complex numbers. ε_{r_i} is the permittivity of the material at layer "i". The effective permittivity of materials may be obtained from optical measurements, but for metals, Drude's model presented in section 2.1 may also be used, if appropriate. $\vec{J}_{Ii}$ denotes the impressed current density at layer "i". The propagation constants are related by:

$$k_i^2 = k_x^2 + k_y^2 + k_{z_i}^2 \tag{5.5}$$

where $k_y = 0$ in this planar structure.

$$k_i^2 = k_0^2\varepsilon_{r_i} \tag{5.6}$$

where $k_0^2 = \omega^2\mu_0\varepsilon_0$ and

$$k_{z_i} = \pm\sqrt{k_i^2 - k_x^2} \tag{5.7}$$

Applying (5.3) and (5.4) with (5.1) and (5.2) we obtain:

$$E_{z_i}(z) = \frac{-\left(jk_{x_i}H_{y_i} + J_{Iz_i}\right)}{j\omega\varepsilon_0\varepsilon_{r_i}} = \frac{j\omega\mu_0}{k_i^2}\left(jk_{x_i}H_{y_i} + J_{Iz_i}\right) \tag{5.8}$$

$$E_{x_i}(z) = \frac{-1}{(j\omega\varepsilon_0\varepsilon_{r_i})}\left(\frac{\partial H_{y_i}}{\partial z} + J_{Ix_i}\right) = \frac{j\omega\mu_o}{k_i^2}\left(\frac{\partial H_{y_i}}{\partial z} + J_{Ix_i}\right) \tag{5.9}$$

We raise the order of the derivative of (5.3) and (5.4), and get:

$$\nabla^2\vec{H}_i + k_i^2\vec{H}_i = -\nabla \times \vec{J}_{I_i} \tag{5.10}$$

$$\nabla^2\vec{E}_i + k_i^2\vec{E}_i = j\omega\mu_0\vec{J}_{I_i} \tag{5.11}$$

Equations (5.3) and (5.4) are first order coupled differential equations, which can be uncoupled by raising the order of the derivative only if the resulting equations (5.10 and 5.11) are homogeneous. This will be proven the case. In order to heat the waveguide a constant (DC) current is injected to heat it. Therefore, this can be modeled in Maxwell's equations by an impressed DC current density. Fortunately, by the superposition principle, it is possible to solve the problem by solving the DC and high frequency components independently. Subsequently, the results may be summed together. In any case, we have little interest of the static field distribution due to the impressed DC current density.

We are only interested in the refractive index variation occurring near a heated waveguide when a high current density is injected through it, because only the refractive index variation will have an impact on the high frequency solution. For this reason, only the high frequency solution will be investigated with consideration to the refractive index change. Therefore, in the metal layer, solving for the high frequency components only (without the DC source term: $\vec{J}_{I_i}$), (5.10) and (5.11) become homogeneous equations and can be decoupled.

Using the method of separation of variable, the homogeneous vector wave equation is decomposed into scalar Helmholtz Equations (5.12-5.14) where such decomposition is possible because of the initial assumption that $H_{y_i}(x,z) = H_{y_i}(z)H_{y_i}(x)$ and $\vec{E}_i(x,z) = \left[\hat{x}E_{x_i}(z) + \hat{z}E_{z_i}(z)\right]E_i(x)$.

$$\frac{\partial^2 H_{y_i}(z)}{\partial z^2} + k_{z_i}^2 H_{y_i}(z) = 0, \qquad \frac{\partial^2 H_{y_i}(x)}{\partial x^2} + k_{x_i}^2 H_{y_i}(x) = 0 \tag{5.12}$$

$$\frac{\partial^2 E_{z_i}(z)}{\partial z^2} + k_{z_i}^2 E_{z_i}(z) = 0, \qquad \frac{\partial^2 E_{z_i}(x)}{\partial x^2} + k_{x_i}^2 E_{z_i}(x) = 0 \tag{5.13}$$

$$\frac{\partial^2 E_{x_i}(z)}{\partial z^2} + k_{z_i}^2 E_{x_i}(z) = 0, \qquad \frac{\partial^2 E_{x_i}(x)}{\partial x^2} + k_{x_i}^2 E_{x_i}(x) = 0 \tag{5.14}$$

The general solution of (5.10), without the DC impressed current density, for the lower infinite medium is:

$$H_{y_s}(z) = Ae^{jk_{z_s}z} \tag{5.15}$$

where the subscript "s" denotes the substrate. The solution is inserted in (5.8) and (5.9), without the source terms, to obtain $E_{x_s}(z)$ and $E_{z_s}(z)$:

$$\omega\varepsilon_0 E_{x_s}(z) = \frac{-k_{z_s}}{\varepsilon_{r_s}} A e^{jk_{z_s}z} \tag{5.16}$$

$$\omega\varepsilon_0 E_{z_s}(z) = \frac{-k_x}{\varepsilon_{r_s}} A e^{jk_{z_s}z} \tag{5.17}$$

$$k_{z_s} = \pm\sqrt{k_s^2 - k_x^2} \tag{5.18}$$

Similarly, the solution within a layer is:

$$H_{y_i}(z) = B_i \cosh(jk_{z_i}(z - z_i)) + C_i \sinh(jk_{z_i}(z - z_i)) \tag{5.19}$$

$$\omega\varepsilon_0 E_{x_i}(z) = \frac{-k_{z_i}}{\varepsilon_{r_i}}[B_i \sinh(jk_{z_i}(z - z_i)) + C_i \cosh(jk_{z_i}(z - z_i))] \tag{5.20}$$

$$\omega\varepsilon_0 E_{z_i}(z) = \frac{-k_x}{\varepsilon_{r_i}}[B_i \cosh(jk_{z_i}(z - z_i)) + C_i \sinh(jk_{z_i}(z - z_i)) \tag{5.21}$$

$$k_{z_i} = \pm\sqrt{k_i^2 - k_x^2} \tag{5.22}$$

where the fields within a layer is written in terms of the fields at the bottom of this layer denoted z_i. The solution for the upper infinite medium is:

$$H_{y_c}(z) = De^{-jk_{z_c}(z-d_T)} \tag{5.23}$$

$$\omega\varepsilon_0 E_{x_c}(z) = \frac{k_{z_c}}{\varepsilon_{r_c}} De^{-jk_{z_c}(z-d_T)} \tag{5.24}$$

$$\omega\varepsilon_0 E_{z_c}(z) = \frac{-k_x}{\varepsilon_{r_c}} De^{-jk_{z_c}(z-d_T)} \tag{5.25}$$

$$k_{z_c} = \pm\sqrt{k_c^2 - k_x^2} \tag{5.26}$$

$$d_T = \sum_{i=1}^{n} d_i \tag{5.27}$$

where the subscript "c" denotes the upper cladding and "n" denotes the total number of layers. Choosing $\Im m\{k_{z_s}, k_{z_c}\}<0$ causes the solution to be bound while $\Im m\{k_{z_s}, k_{z_c}\}>0$ ensures that the solution is leaky. Depending on the desired solution, k_{z_s} and k_{z_s} must be chosen accordingly. As will become apparent shortly, all fields and parameters (D, B_i ,C_i, k_{z_s} ,k_{z_s} and k_{z_i}) are determined as a function of "A" and k_x where "A" is set arbitrarily and k_x is determined by solving the system. Because "A" is arbitrarily chosen, an appropriate way of displaying the resulting fields is to normalize them with the square root of the total power contained within as shown by:

$$\psi = \int_{-\infty}^{\infty} \vec{x} \cdot (E \times H^*) dz = \int_{-\infty}^{\infty} S_x(z) dz \Rightarrow \sqrt{\psi} \tag{5.28}$$

In order to link the parameters and fields of all layers to "A", appropriate boundary conditions are used. These boundary conditions reveal that all fields tangential to an interface are continuous. Hence, we may write in reference to (5.15) to (5.25):

$$H_{y_1}(z_1) = H_{y_s}(z_1) \Rightarrow B_1 = A \tag{5.29}$$

$$E_{x_1}(z_1) = E_{x_s}(z_1) \Rightarrow C_1 = \frac{k_{z_s} \varepsilon_{r_1}}{k_{z_1} \varepsilon_{r_s}} A \tag{5.30}$$

$$H_{y_{i+1}}(z_{i+1}) = H_{y_i}(z_{i+1}) \Rightarrow B_{i+1} = B_i \cosh(jk_{z_i} d_i) + C_i \sinh(jk_{z_i} d_i) \tag{5.31}$$

$$E_{x_{i+1}}(z_{i+1}) = E_{x_i}(z_{i+1}) \Rightarrow C_{i+1} = \frac{k_{z_i} \varepsilon_{r_{i+1}}}{k_{z_{i+1}} \varepsilon_{r_i}} \left[B_i \sinh(jk_{z_i} d_i) + C_i \cosh(jk_{z_i} d_i) \right] \tag{5.32}$$

$$H_{y_c}(z_{n+1}) = H_{y_n}(z_{n+1}) \Rightarrow D = B_n \cosh(jk_{z_n} d_n) + C_n \sinh(jk_{z_n} d_n) \tag{5.33}$$

and using the following two equations: $H_{y_i}(z_i) = H_{y_{i-1}}(z_i) = B_i$ and $\omega\varepsilon_0 E_{x_i}(z_i) = \omega\varepsilon_0 E_{x_{i-1}}(z_i) = \frac{-k_{z_i}}{\varepsilon_{r_i}} C_i$ we may rewrite (5.16) and (5.17) in the following matrix form:

$$\begin{pmatrix} H_{y_i}(z) \\ \omega\varepsilon_0 E_{x_i}(z) \end{pmatrix} = \begin{pmatrix} \cosh(jk_{z_i}(z - z_i)) & \frac{-\varepsilon_{r_i}}{k_{z_i}} \sinh(jk_{z_i}(z - z_i)) \\ \frac{-k_{z_i}}{\varepsilon_{r_i}} \sinh(jk_{z_i}(z - z_i)) & \cosh(jk_{z_i}(z - z_i)) \end{pmatrix} \begin{pmatrix} H_{y_{i-1}}(z_i) \\ \omega\varepsilon_0 E_{x_{i-1}}(z_i) \end{pmatrix} \tag{5.34}$$

which clearly shows the interdependence of the fields of each layer. The fields at "i" are determined from the fields at "i-1". Similarly, the fields at "i-1" can be determined from the fields at "i-2" and so on. We define the matrix M_i as:

$$M_i = \begin{pmatrix} \cosh(jk_{z_i}d_i) & \frac{-\varepsilon_{r_i}}{k_{z_i}}\sinh(jk_{z_i}d_i) \\ \frac{-k_{z_i}}{\varepsilon_{r_i}}\sinh(jk_{z_i}d_i) & \cosh(jk_{z_i}d_i) \end{pmatrix} = \begin{pmatrix} m_{11_i} & m_{12_i} \\ m_{21i} & m_{22_i} \end{pmatrix} \tag{5.35}$$

where the fields at "b" may be determined from the fields at "u" from the equation:

$$\begin{pmatrix} H_{y_{b+1}}(z_{b+1}) \\ \omega\varepsilon_0 E_{x_{b+1}}(z_{b+1}) \end{pmatrix} = \begin{pmatrix} H_{y_b}(z_{b+1}) \\ \omega\varepsilon_0 E_{x_b}(z_{b+1}) \end{pmatrix} = \prod_{i=0}^{b-(u+1)} M_{b-i} \begin{pmatrix} H_{y_u}(z_{u+1}) \\ \omega\varepsilon_0 E_{x_u}(z_{u+1}) \end{pmatrix} = \prod_{i=0}^{b-(u+1)} M_{b-i} \begin{pmatrix} H_{y_{u+1}}(z_{u+1}) \\ \omega\varepsilon_0 E_{x_{u+1}}(z_{u+1}) \end{pmatrix} \tag{5.36}$$

The following must hold: b>=u+1. The layers are numbered from 1 to n and therefore u>=0 and b<=n. Hence, the fields at the upper interface can be determined from the fields at the lower interface with:

$$\begin{pmatrix} H_{y_c}(z_{n+1}) \\ \omega\varepsilon_0 E_{x_c}(z_{n+1}) \end{pmatrix} = \prod_{i=0}^{n-1} M_{n-i} \begin{pmatrix} H_{y_s}(z_1) \\ \omega\varepsilon_0 E_{x_s}(z_1) \end{pmatrix} \tag{5.37}$$

where "n" is the total number of layers excluding semi-infinite media. For this particular situation, the following matrix is defined:

$$\begin{pmatrix} m_{11} & m_{12} \\ m_{21} & m_{22} \end{pmatrix} = \prod_{i=0}^{n-1} M_{n-i} \tag{5.38}$$

Equation (5.37) can be rewritten as:

$$H_{y_n}(z_{n+1}) = H_{y_c}(z_{n+1}) = m_{11}H_{y_s}(z_1) + m_{12}\omega\varepsilon_0 E_{x_s}(z_1) \tag{5.39}$$

$$\omega\varepsilon_0 E_{x_n}(z_{n+1}) = \omega\varepsilon_0 E_{x_c}(z_{n+1}) = m_{21}H_{y_s}(z_1) + m_{22}\omega\varepsilon_0 E_{x_s}(z_1) \tag{5.40}$$

These fields are substituted by their parametric values in Equations (5.15) and (5.16) and (5.23) and (5.24). The Equations (5.39) and (5.40) are then manipulated to obtain:

$$\left(m_{11} - m_{12}\frac{k_{z_s}}{\varepsilon_{r_s}}\right) - \frac{\varepsilon_{r_c}}{k_{z_c}}\left(m_{21} - m_{22}\frac{k_{z_s}}{\varepsilon_{r_s}}\right) = 0 \tag{5.41}$$

A solution to (5.40) is in fact a value of k_x from which k_{z_s} and k_{z_c} are determined and which satisfies Equation (5.41). In practice, Equation (5.41) takes the form of (5.42) because the left-hand side of Equation (5.41) usually does not become exactly zero:

$$\left|\left(m_{11} - m_{12}\frac{k_{z_s}}{\varepsilon_{r_s}}\right) - \frac{\varepsilon_{r_c}}{k_{z_c}}\left(m_{21} - m_{22}\frac{k_{z_s}}{\varepsilon_{r_s}}\right)\right| = |F(k_x)| \tag{5.42}$$

Instead, a solution occurs when (5.41) is closest to zero or equivalently a local or global minimum. The condition for which a solution is found is written in the form of (5.43).

$$|F(k_x)| < \text{tol} \tag{5.43}$$

where "tol" is the value under which $|F(k_x)|$ must remain if it is going to have an acceptable solution, k_x, solving the system. In order to have an accurate solution, "tol" must be set as close as possible to the minimum of (5.42). This can be done by setting "tol" smaller than the minimum of (5.42) and successively increasing it until a solution is found.

A guess for k_x is passed as an argument to a root-finding function which subsequently finds the exact value of k_x satisfying Equation (5.43). In particular, Muller's root-finding method was used since it is a robust method, which can find complex roots. The details of the root finding method are included in Appendix C.

5.2 VALIDATION

In order to validate the results obtained by the optical simulator described above, results are compared to some obtained from the literature. We consider the same symmetric structure analyzed by Burke et Al. [14]. A thin silver metal film with permittivity ε_m = -19-0.53i is bounded by dielectrics of refractive index $n_1 = \sqrt{\varepsilon_1} = 2$ at He-Ne wavelength (λ_o=632.8nm). The normalized phase constant, $\frac{\beta}{\beta_0}$, and normalized attenuation constant, $\frac{\alpha}{\beta_0}$, is plotted as a function of metal film thickness in Figure 5.2. An asymmetric and symmetric mode were found denoted "a" and "s" respectively on the graph. The curves correspond to results generated by this work while the markers are points taken from [14]. The markers were obtained by measuring specific points on the graph with a ruler. The measurement errors may explain the small discrepancy in the figure. In general, however there is a good agreement with the literature.

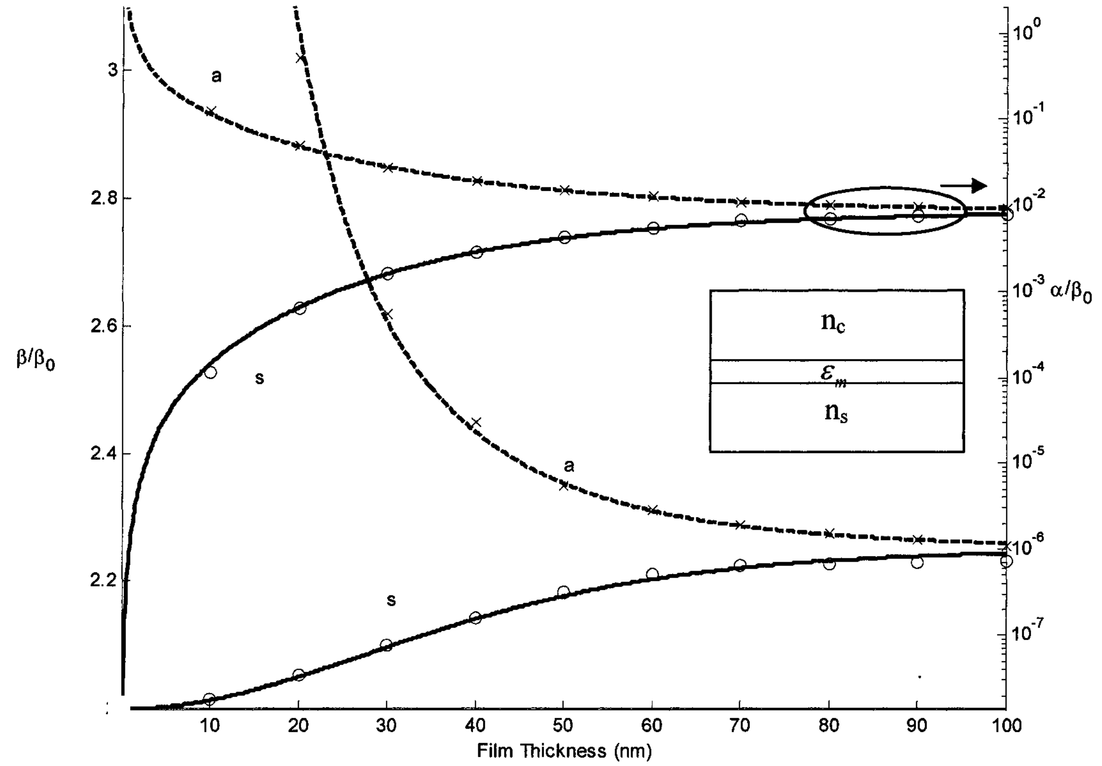

Figure 5.2: Normalized phase constant and normalized attenuation constant of the modes propagating along the waveguide as a function of metal film thickness. The letter "a" and "s" indicates the symmetric and asymmetric bound modes respectively. The curves correspond to results generated by this work while the markers are points taken from reference [14]. ε_m**=-19-0.53i, n_s=2, n_c=2, λ_0=0.6328μm.**

In order to further the validation process, the asymmetric structure considered by Burke [14] has also been simulated. In particular, a silver metal film is bounded by two dielectrics with refractive index $\sqrt{\varepsilon_1} = 1.9$ and $\sqrt{\varepsilon_2} = 2$ respectively at He-Ne wavelength. The results are presented in Figure 5.3 and 5.4.

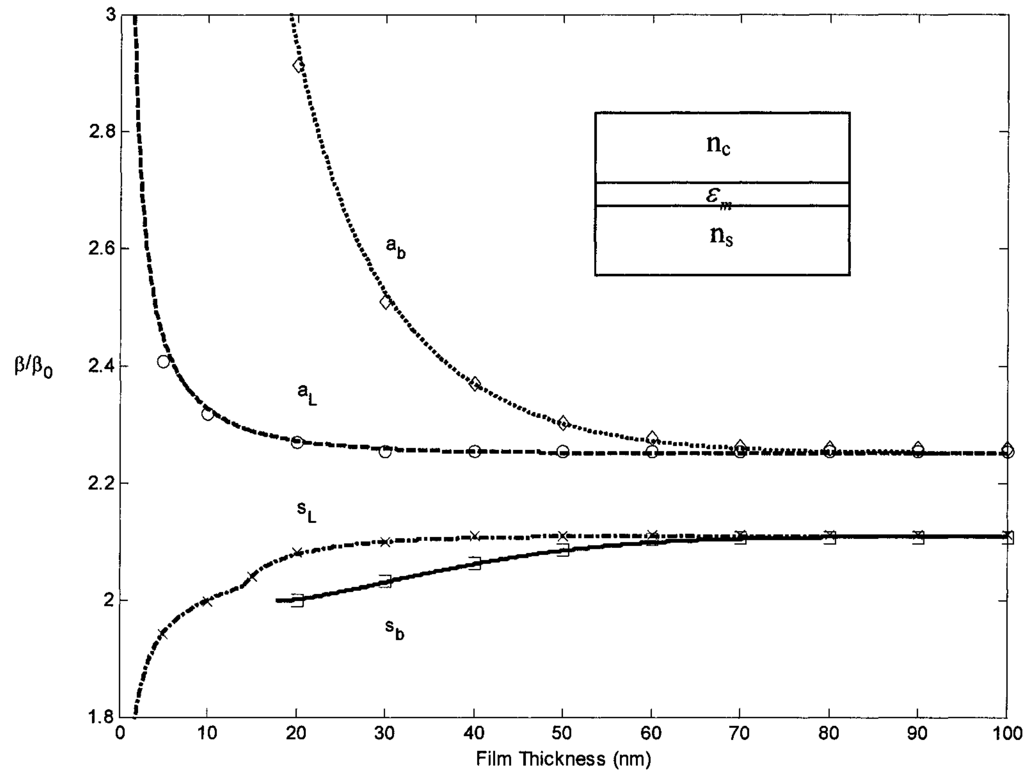

Figure 5.3: Normalized phasen constant of the propagating modes as a function of metal film thickness. The letters "a" and "s" symbolizes the asymmetric and symmetric mode respectively, while "L" and "b" symbolizes a leaky and bound mode respectively. The curves correspond to results generated by this work while the markers are points taken from reference [14]. ε_m=-19-0.53i, n_s=1.9, n_c=2, λ_0=0.6328μm

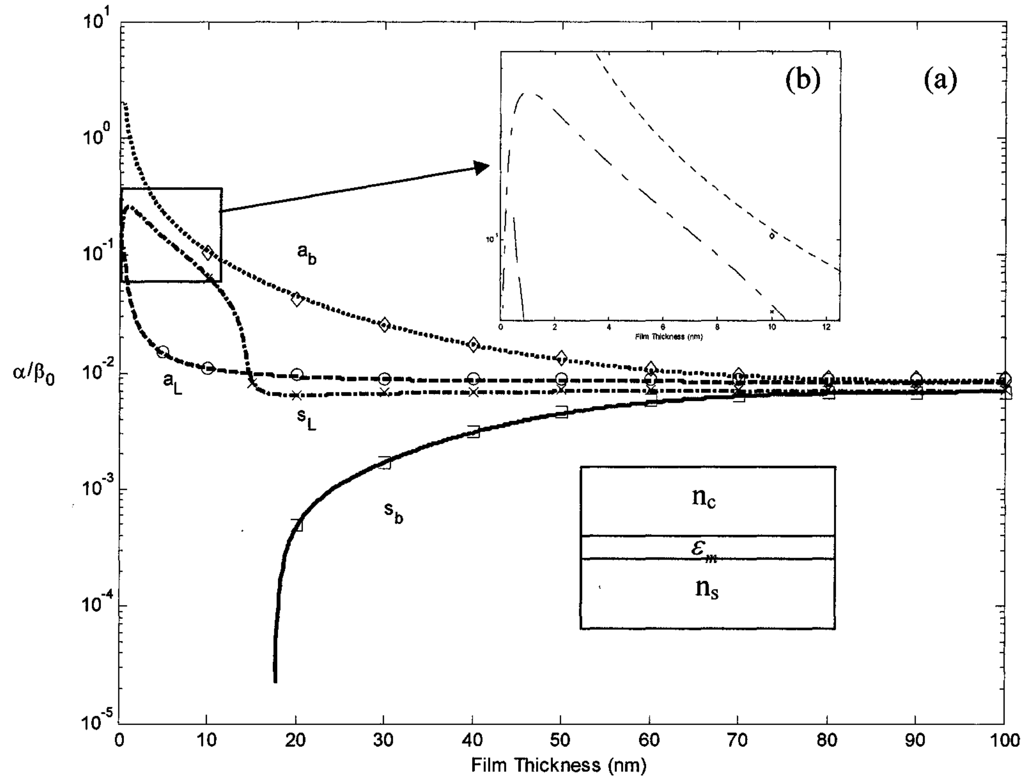

Figure 5.4: Normalized attenuation constant of the propagating modes as a function of metal film thickness. (b) is a zoom in the region that is not clear in (a). The letters "a" and "s" symbolizes the asymmetric and symmetric mode respectively, while "L" and "b" symbolizes a leaky and bound mode respectively. The curves correspond to results generated by this work while the markers are points taken from reference [14]. ε_m **=-19-0.53i,** n_s**=1.9,** n_c**=2,** λ_0**=0.6328μm**

As is shown by these figures the results are in good agreement with the literature. Furthermore, Burke plotted the normalized attenuation constant down to 1 or 2 nanometers for the s_L mode. In this work, by doing the same down to 0.1 nm for the s_L mode, we notice that the normalized attenuation constant does not continue increasing but in fact starts decreasing as shown in Figure 5.4 (b).

5.3 Results and discussion for s_b mode

The structure that was investigated in the laboratory was modeled. The finite width metal waveguide was approximated as a thin film slab for the purpose of the optical model. The results generated by the optical model implemented in section 5.1 are presented in this section. The results for the s_b mode will be presented.

The structure contains a gold metal film bound by silica and polymer materials. The silica and polymer are 15μm and 124.985μm thick respectively. The metal film thickness is 15nm. There is also a 10μm layer of silicon on top of a semi-infinite layer of silicon (n=3.475) for the purpose of the model. On top of the polymer lies a semi-infinite layer of air (n=1). The thickness of the total structure is 150μm in this model. Upon heating, a temperature gradient occurs in the structure as was shown in chapter 4, which was converted to its corresponding refractive index gradient in the structure given the existence of TOCs describing the materials. In the optical model, it was assumed that the polymer and silica were matched at n=1.4469 without the presence of heating. Results were generated at communications wavelength: λ_o=1.55μm.

Because we are dealing with waveguides of various widths in the laboratory, it is more meaningful to express the results as a function of current density [A/m^2] rather than current [A]. For the same reason, the results will be presented as a function of power density [W/m^3] rather than power [W]. To obtain current or power it suffices to multiply them by the dimensions of the waveguide.

The nomenclature for the modes as expressed by Burke and other authors cannot be strictly applied for our structure given the complex spatial dispersion of the refractive index. However, we may trace the evolution of the mode from the simple case towards the desired structure and state that it is the evolution of the mode instead of the mode per say. Therefore, whenever, a particular mode is mentioned for this structure, it in fact refers to the evolution of that mode.

Figure 5.5 presents the normalized phase constant as a function of metal film thickness for a variety of injected current density into the metal optical waveguide. Each curve is related to a particular current density and is identified by the letters "a" through "i", where the successive letters are attributed to the decreasing curves. As shown in the figure, the normalized propagation suffers dispersion with thin metal film thickness. In particular, the normalized phase constant decreases with reduction of thin film thickness. It tends to that of the TEM mode supported by the background material as the thin film vanishes. On the other hand, as the thin film thickness increases, the normalized attenuation constant tends to that supported by a single interface. The power densities associated to the current densities expressed in the caption of Figure 5.5 to 5.7 and Figure 5.11 to 5.18 are: a)

0.177$\mu W/\mu m^3$ b) 160 $\mu W/\mu m^3$ c) 284.4 $\mu W/\mu m^3$ d) 360 $\mu W/\mu m^3$ e) 444.4 $\mu W/\mu m^3$ f) 537.7 $\mu W/\mu m^3$ g) 640 $\mu W/\mu m^3$ h) 751.1 $\mu W/\mu m^3$ i) 921.6 $\mu W/\mu m^3$, respectively. As the waveguide is heated for a given metal film thickness, the normalized phase constant is reduced. This can be explained by the fact that the sign of the TOC for the polymer is negative and its amplitude is much greater than that of silica. Upon heating, the refractive index of the polymer will be reduced much more than the corresponding increase of the refractive index of silica. The average refractive index near the waveguide is therefore reduced.

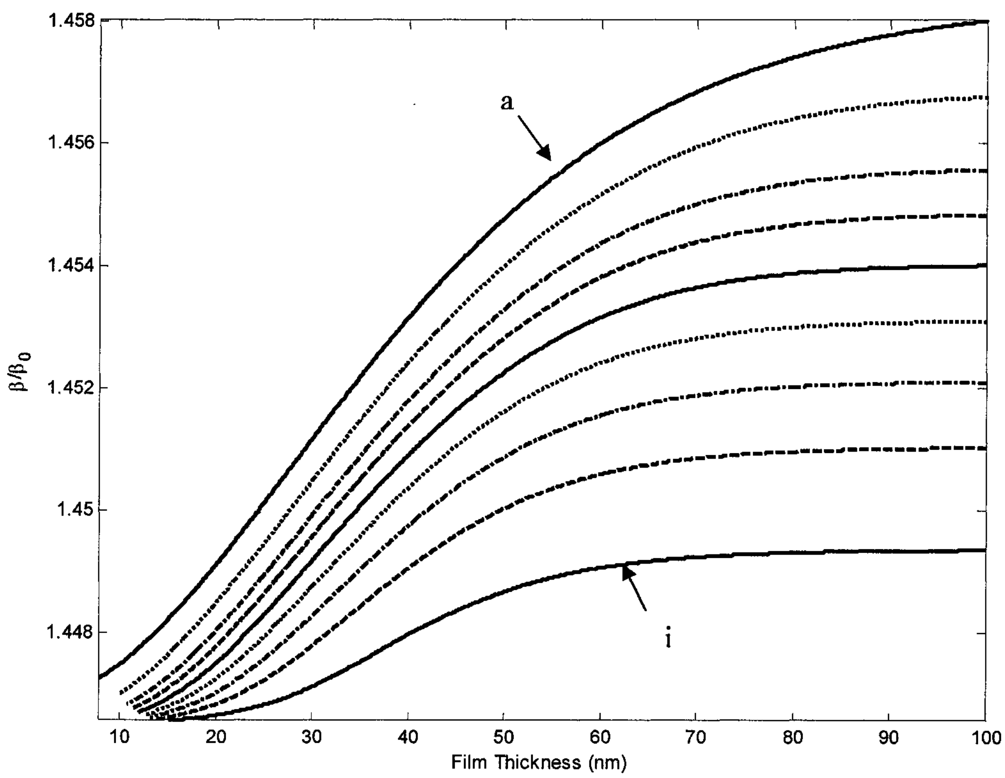

Figure 5.5: Normalized phase constant of the s_b mode as a function of metal film thickness for a variety of injected current densities into the metal optical waveguide. Each curve is related to a particular current density and is identified by the letters "a" through "i", where the successive letters are attributed to the decreasing curves. a) 1.33 GA/m^2 b) 40 GA/m^2 c) 53.33 GA/m^2 d) 60 GA/m^2 e) 66.66 GA/m^2 f) 73.33 GA/m^2 g) 80 GA/m^2 h) 86.66 GA/m^2 i) 96 GA/m^2

Figure 5.6 (a) represents the normalized attenuation constant as a function of metal film thickness for a variety of injected current densities into the metal optical waveguide. Figure 5.6 (b) and (c) zoom into areas that are not clear in Figure (a). Each curve is related to a particular current density and is identified by the letters "a" through "i" as in Figure 5.5. The letters in Figure 5.6 (b) are successive from bottom to top and from left to right in Figure (c). There are three important effects portrayed by this figure. For films around 35nm-80nm thick, the normalized attenuation constant increases upon heating as shown in (b). For thinner films and for enough heating, the opposite situation occurs as shown in (c). Finally, we see that the mode cutoff thickness increases with heating as shown in (c). For increasing film thickness, the normalized attenuation and phase constant tend towards that of the modes supported by a single interface.

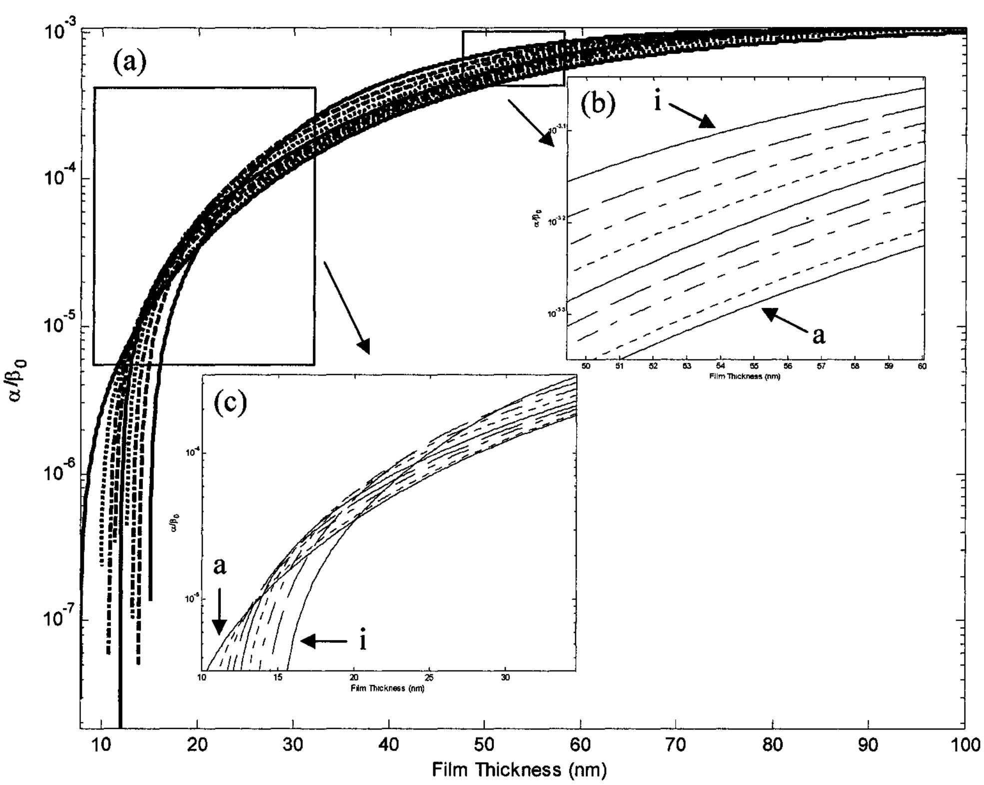

Figure 5.6: Normalized attenuation constant of the s_b mode as a function of metal film thickness for a variety of injected current densities into the metal optical waveguide. (b) and (c) are zooms in areas that are not clear in (a). Each curve is related to a particular current density and is identified by the letters "a" through "i". The letters in (b) are successive from bottom to top and from left to right in (c). a) 1.33 GA/m^2 b) 40 GA/m^2 c) 53.33 GA/m^2 d)60GA/m^2 e) 66.66 GA/m^2 f) 73.33 GA/m^2 g) 80 GA/m^2 h) 86.66 GA/m^2 i) 96 GA/m^2

Figure 5.7 illustrates the mode power attenuation as a function of metal film thickness for a variety of injected current densities into the metal optical waveguide. Each curve is related to a particular current density and is labeled "a" through "i". The successive letters are attributed to the increasing curves as in Figure 5.5. Figure 5.7 contains the same information as Figure 5.6 but expressed in dB/cm. It is clear from Figure 5.7 that, for a metal film to have useful waveguiding characteristics, it must be very thin, otherwise, its propagation loss will be very high and power will be wasted.

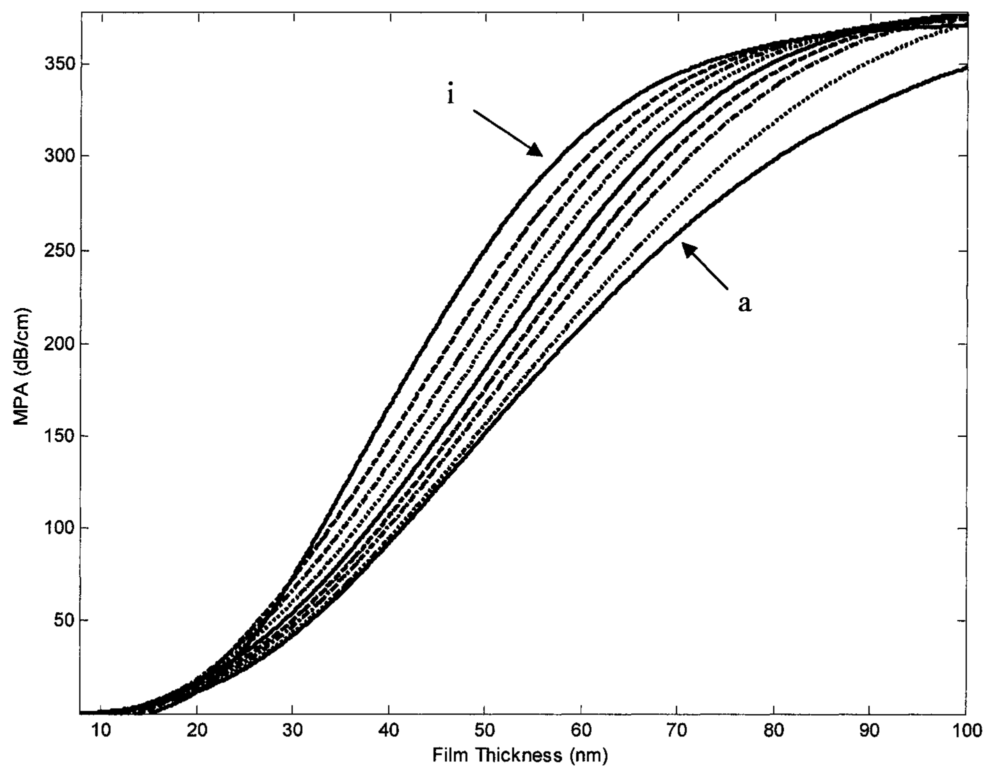

Figure 5.7: Mode power attenuation of the s_b mode as a function of metal film thickness for a variety of injected current density into the metal optical waveguide. Each curve is related to a particular current density and is identified by the letters "a" through "i". The successive letters are attributed to the increasing curves. a) 1.33 GA/m^2 b) 40 GA/m^2 c) 53.33 GA/m^2 d) 60 GA/m^2 e) 66.66 GA/m^2 f) 73.33 GA/m^2 g) 80 GA/m^2 h) 86.66 GA/m^2 i) 96 GA/m^2

Figure 5.8 (a), (b), (c), and (d) represent the normalized attenuation constant, normalized phase constant, mode power attenuation (MPA) and coupling loss (L_c) respectively as a function of injected current density for a 15nm thick metal film. For small applied heating powers, the normalized attenuation constant is rather invariant as depicted by the flat region in Figure 5.8 (a) and (c). For current densities in the region of 60 GA/m^2, there is an increase in the normalized attenuation constant, while for further heating powers, it decreases until mode cutoff. The normalized phase constant is reduced as heat is applied as illustrated in Figure 5.8 (b), because the average refractive index of the claddings surrounding the metal waveguide is reduced.

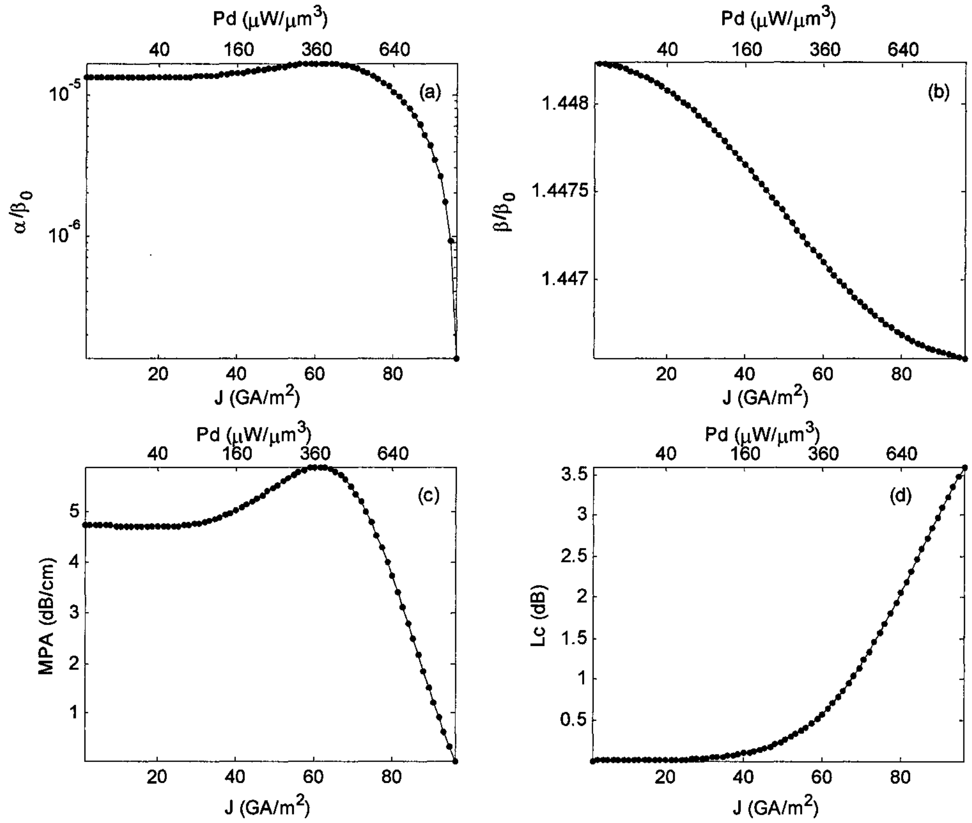

Figure 5.8: Normalized phase constant, attenuation constants, mode power attenuation and coupling loss of the s_b mode as a function of injected current density (or power density). The scale on top of each figure is nonlinear and represented by Pd=J^2/σ.

The coupling loss is determined from the coupling coefficient, which is calculated as [46]:

$$CC = \frac{\int_{-\infty}^{\infty} \hat{x}\cdot(E_1^* \times H_2 + E_2 \times H_1^*)dz}{\sqrt{\psi_1 \psi_2}} = \frac{\int_{-\infty}^{\infty} (E_{z1}^* H_{y2} + E_{z2} H_{y1}^*)dz}{\sqrt{\psi_1 \psi_2}} \tag{5.44}$$

where

$$\psi_2 = \int_{-\infty}^{\infty} \hat{x}\cdot(E_2^* \times H_2 + E_2 \times H_2^*)dz = \int_{-\infty}^{\infty}(E_{z2}^* H_{y2} + E_{z2} H_{y2}^*)dz,$$

$$\psi_1 = \int_{-\infty}^{\infty} \hat{x}\cdot(E_1^* \times H_1 + E_1 \times H_1^*)dz = \int_{-\infty}^{\infty}(E_{z1}^* H_{y1} + E_{z1} H_{y1}^*)dz$$

and the subscript "1" and "2" denotes the fields of the unheated and heated section of the waveguide respectively. Given that only the E_z, H_y and E_x fields exist, these equations were simplified as shown on the right hand side of each equation.

The coupling loss is defined as:

$$LC = -10\,\log\left(|CC|^2\right) \tag{5.45}$$

As heat is applied, the field distribution changes such that an increasing mismatch in the the mode field-overlap occurs, as shown in Figure 5.8 (d). Coupling loss may also be determined approximately between the fiber and mode supported by the waveguide from the following:

$$CC = \frac{\int_{-\infty}^{\infty} E_1 E_2^* dz}{\sqrt{\psi_1 \psi_2}} \tag{5.46}$$

where $\psi_1 = \int_{-\infty}^{\infty} |E_1|^2 dz$, $\psi_2 = \int_{-\infty}^{\infty} |E_2|^2 dz$,

$$E_2 = E_0 e^{\frac{-z^2}{w_0^2}} \tag{5.47}$$

where $\frac{w_0}{a} = 0.65 + \frac{1.619}{V^{3/2}} + \frac{2.879}{V^6}$ and $V = \frac{2\pi a}{\lambda_0} NA$. E_2 is the field of the fiber and E_1 is the most significant field of the mode supported by the waveguide namely Ez. "a" and NA are the radius of the core of the fiber and numerical aperture of the fiber, respectively.

In order to compare the simulations to the IL found in the laboratory, we must develop a model to determine the IL of the waveguide as shown in Figure 5.9. Keep in mind that heating a fraction of the total length of the plasmon-polariton waveguide introduces a transversal and longitudinal refractive index gradient, which opposes one of the initial assumptions in the first paragraph of chapter 5. In the longitudinal direction, the amplitude of the refractive index gradient is large only near the region separating the heated and unheated section of the waveguide [22], whereas it is small in other regions. To consider this effect into the 1D model, we can approximate the 3D domain as three 3D domains of longitudinally homogeneous regions (longitudinal gradient is 0). The three domains comprise one heated domain separating two unheated domains. Each homogeneous region is separated by an infinitely small region with a longitudinal gradient that resembles a Dirac-Delta function. The Dirac gradient is considered into the 1D model by introducing a coupling loss as shown by LC1 in Figure 5.9. Each domain has its own MPA as represented in the figure. All these considerations and approximations were added to the 1D model via Equation (5.48) to obtain the total loss of the light propagating along the plasmon-polariton waveguide:

$$TL=MPA1*L1+MPA2*L2+2*LC1+LC2 \tag{5.48}$$

where TL, MPA, L, LC denotes the total loss expressed in dB, mode power attenuation expressed in dB/cm, length expressed in cm and coupling loss expressed in dB, respectively.

In the laboratory, an 8μm wide and 7.28mm length waveguide had a 4.44mm heated section. There are distinct MPAs and lengths for the heated and unheated sections denoted MPA1, MPA2, L1 and L2 respectively. Coupling losses between the PMF and the waveguide is denoted by LC2, while coupling losses between the MMF and the waveguide is denoted LC3. Coupling losses also occur at each end of the heated section between the heated and unheated waveguide and it is denoted LC1. However, as can be seen by Equation (5.48), there is only one coupling loss attributed to the fibers. This is so because, in the experiments, the input fiber was a PMF while the output fiber was a MMF. The core of the MMF is much larger than the waveguide and the coupling loss is assumed negligible compared to that of the PMF. The total loss is calculated for the various current densities and results are presented in Figure 5.10 (a). The coupling loss found between the PM fiber and unheated waveguide is 0.147 dB.

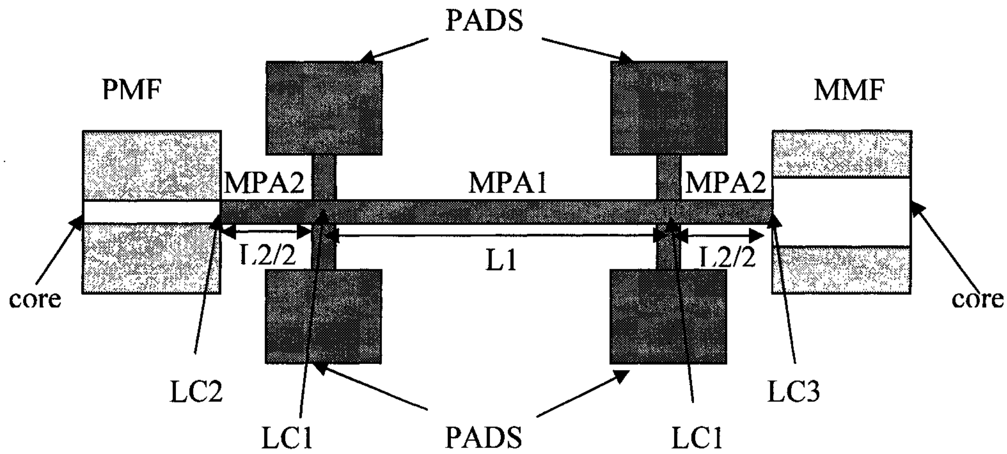

Figure 5.9: Illustration of the coupling losses and propagation losses of the heated waveguide. The waveguide is heated by injecting current into the waveguides through the pads and arms perpendicular to it. The waveguide is excited through end-fire coupling with a PMF at the input. A multimode fiber is located at the output.

Figure 5.10 (a) and (b) represent the IL and mode field diameter of the s_b mode as a function of injected current density. The IL increases as a function of current density. The same applies to the MFD except that at the highest current density, the MFD is reduced. It is important to note that the terminology "mode field diameter" is not quite appropriate, since there are no diameters to be considered in a slab structure. In this context, when we refer to mode field diameter, we actually mean the distance separating the two $1/e^2$ points of the maximum power. The MFD is determined from the following equations:

$$c = \frac{\int_{-\infty}^{\infty} z\,\Re(S_x(z))dz}{\psi} \qquad (5.49)$$

where "c" is the center of the power distribution. $\psi = \int_{-\infty}^{\infty} \Re(S_x(z))dz$ is a normalization factor used in Equation (5.49). From the center of the power distribution, we search outward for the two $1/e^2$ points of the maximum optical power and the distance separating them is obtained. In this work, this distance is defined as the mode field diameter.

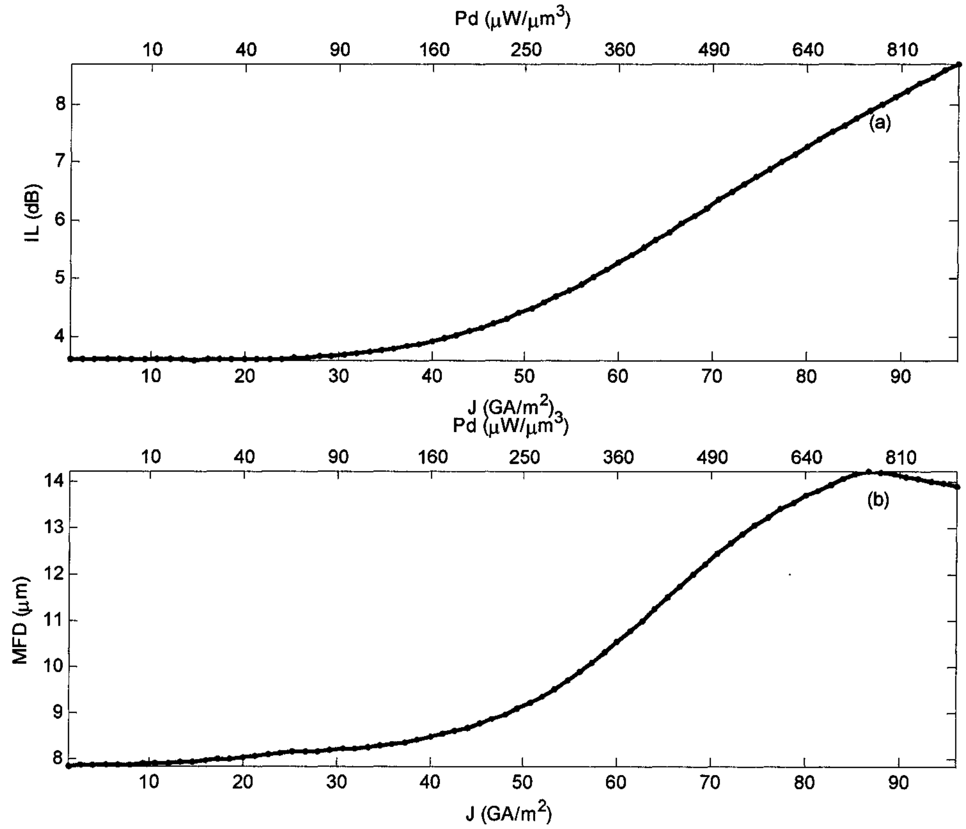

Figure 5.10: Insertion loss and mode field diameter of the s_b mode as a function of injected current density (or power density). The scale on top of each figure is nonlinear and represented by $Pd=J^2/\sigma$.

It is clear by comparing Figure 5.8 (b) and (d) to Figure 5.10 (a) that at low heating power most of the loss contribution is from the MPA, while at high heating power, it mostly comes from the coupling loss. An example of the power density distribution of the finite width waveguide is shown in Figure 8 of ref [15]. As the finite width waveguide is heated, it is expected that the field distribution evolve in both directions transversal to the mode propagation. A mode mismatch will therefore occur over the whole cross-section and coupling loss should be higher than expected by the 1D model. For Gaussian beams, it is common practice to calculate the 1D coupling losses and double these results to obtain an approximation of the 2D situation. Figure 8 in [15] shows a beam that somewhat resembles a Gaussian beam. For this reason, the coupling loss found in Figure 5.8 (d) can be doubled to approximate the 2D case. The total loss at high heating power should also be increased substantially given twice the coupling loss.

Next, the fields associated with the s_b mode are plotted for a few injected current densities. Evolution of the mode as a function of applied heat is analyzed. For comparison purposes, all fields (E_z, E_x, H_y) for the various injected current densities were normalized by $\sqrt{\psi}$ following the equation:

$$\psi = \int_{-\infty}^{\infty} \hat{x} \cdot \left| \Re(E \times H^*) \right| dz = \int_{-\infty}^{\infty} \left| \Re(E_z H_y^*) \right| dz \tag{5.50}$$

Figure 5.11 represents the real part of the E_z field for the s_b mode as a function of the "z" position for a variety of injected current densities. Each curve is related to a particular current density and is identified by the letters "a" through "i". In (a), the general trend of the fields as a function of applied heat is to move towards the left side of the figure (closer to the silicon). In (b) the amplitude of the oscillation as a function of position increases with heat. The amplitude of the real Ez field in (c) is reduced as a function of applied heat. The behavior in (b) also occurs for the other fields; therefore, it will not be presented in the other figures to prevent redundancy. The interpretation of these results will be presented later.

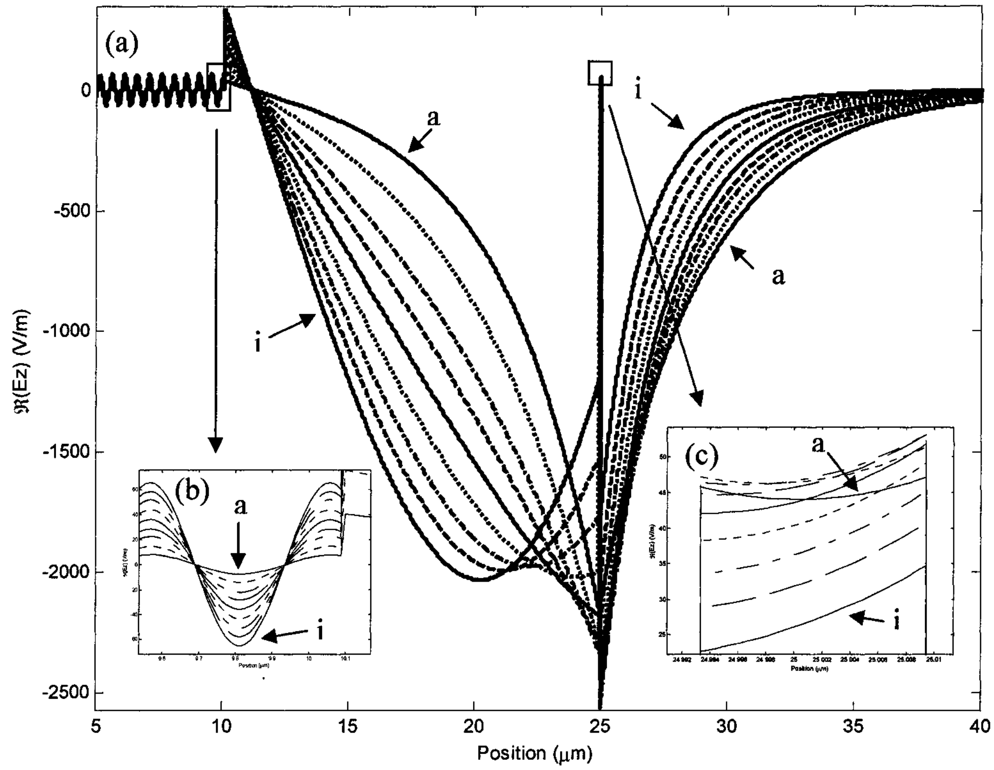

Figure 5.11: Real part of the Ez field for the s_b mode as a function of the vertical position for a variety of injected current densities. Each curve is related to a particular current density and is identified by the letters "a" through "i". a) 1.33 GA/m^2 b) 40 GA/m^2 c) 53.33 GA/m^2 d) 60 GA/m^2 e) 66.66 GA/m^2 f) 73.33 GA/m^2 g) 80 GA/m^2 h) 86.66 GA/m^2 i) 96 GA/m^2. The silicon, silica, metal slab, polymer and air are located at z<10μm, 10μm<z<25μm, 25μm<z<25.015μm, 25.015μm<z<150μm, z>150 respectively.

Figure 5.12 (a) represents the imaginary part of Ez for the s_b mode as a function of "z" position for a variety of injected current densities. Each curve is related to a particular current density and is identified by the letters "a" through "i". In Figure 5.12 (a), the general trend of the imaginary Ez amplitude is to be displaced towards the left of the figure. In (b) the imaginary Ez field amplitude decreases as a function of applied heat.

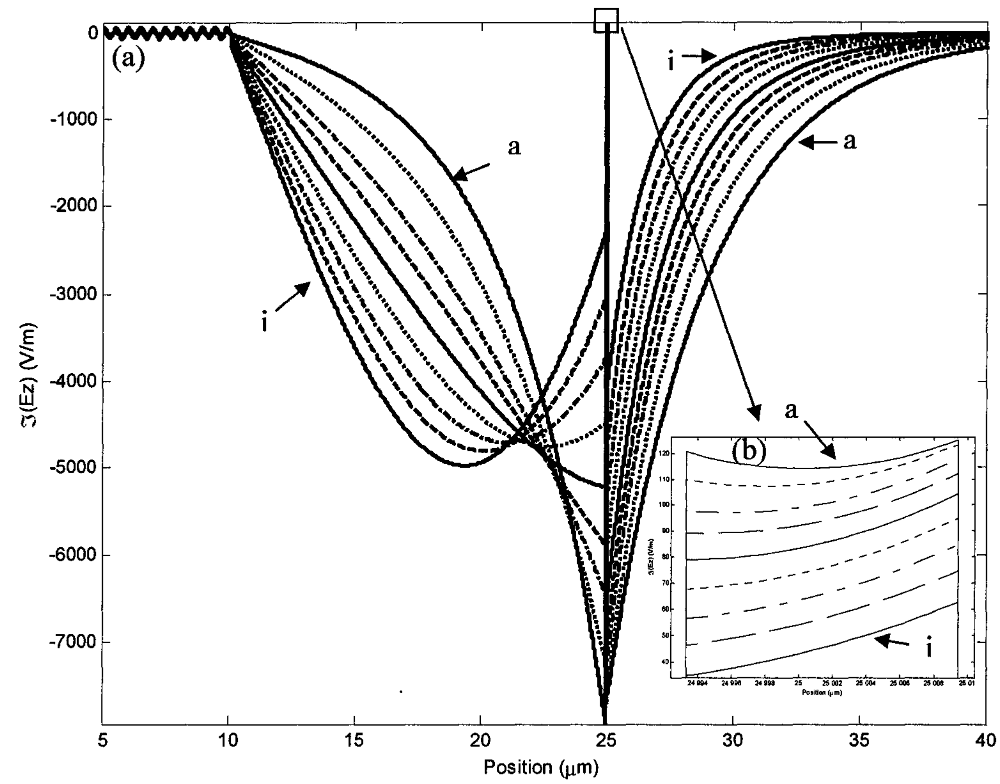

Figure 5.12: Imaginary part of Ez field for the s_b mode as a function of the vertical position for a variety of injected current densities. Each curve is related to a particular current density and is identified by the letters "a" through "i". a) 1.33 GA/m^2 b) 40 GA/m^2 c) 53.33 GA/m^2 d) 60 GA/m^2 e) 66.66 GA/m^2 f) 73.33 GA/m^2 g) 80 GA/m^2 h) 86.66 GA/m^2 i) 96 GA/m^2.
Silicon, silica, metal slab, polymer and air are located at z<10μm, 10μm<z<25μm, 25μm<z<25.015μm, 25.015μm<z<150μm, z>150 respectively.

Figure 5.13 represents the real part of the H_y field for the s_b mode as a function of "z" position for a variety of injected current density. Each curve is related to a particular current density and is identified by the letters "a" through "i". The general trend of the fields in the figure is a displacement towards the left of the figure as a function of injected current density (towards the silicon).

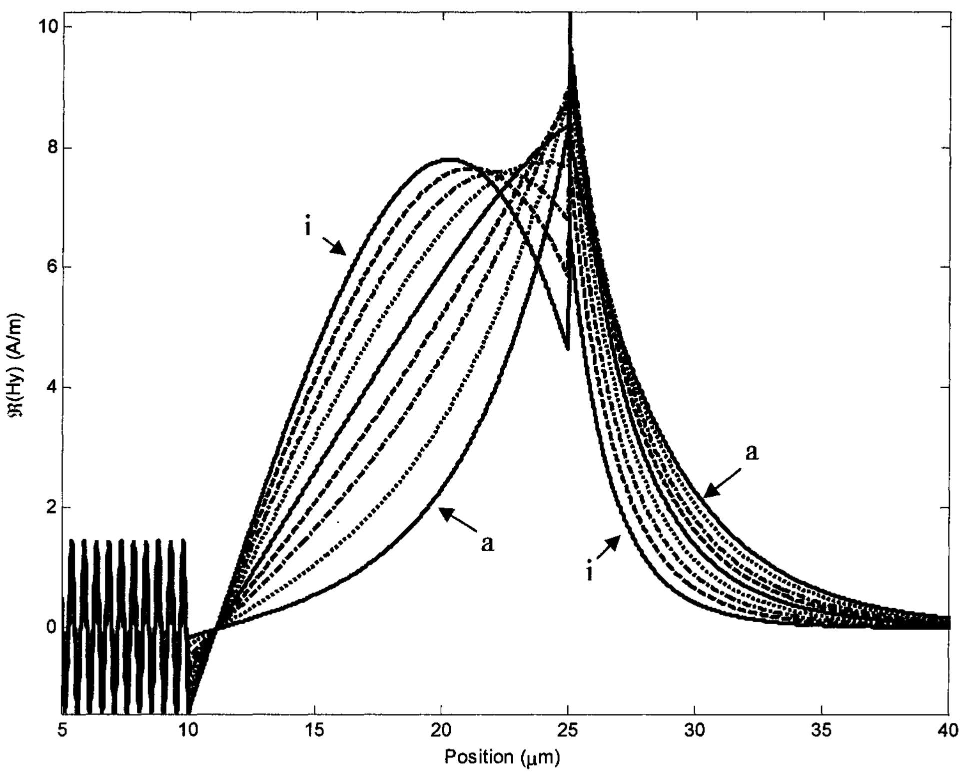

Figure 5.13: Real part of the H_y field for the s_b mode as a function of the vertical position for a variety of injected current densities. Each curve is related to a particular current density and is identified by the letters "a" through "i". a) 1.33 GA/m^2 b) 40 GA/m^2 c) 53.33 GA/m^2 d) 60 GA/m^2 e) 66.66 GA/m^2 f) 73.33 GA/m^2 g) 80 GA/m^2 h) 86.66 GA/m^2 i) 96 GA/m^2. Silicon, silica, metal slab, polymer and air are located at z<10μm, 10μm<z<25μm, 25μm<z<25.015μm, 25.015μm<z<150μm, z>150 respectively.

Figure 5.14 represents the imaginary part of the H_y field for the s_b mode as a function of the "z" position for a variety of injected current density. Each curve is related to a particular current density and is identified by the letters "a" through "i". The fields in the figure are displaced towards the left of the figure as a function of injected current density.

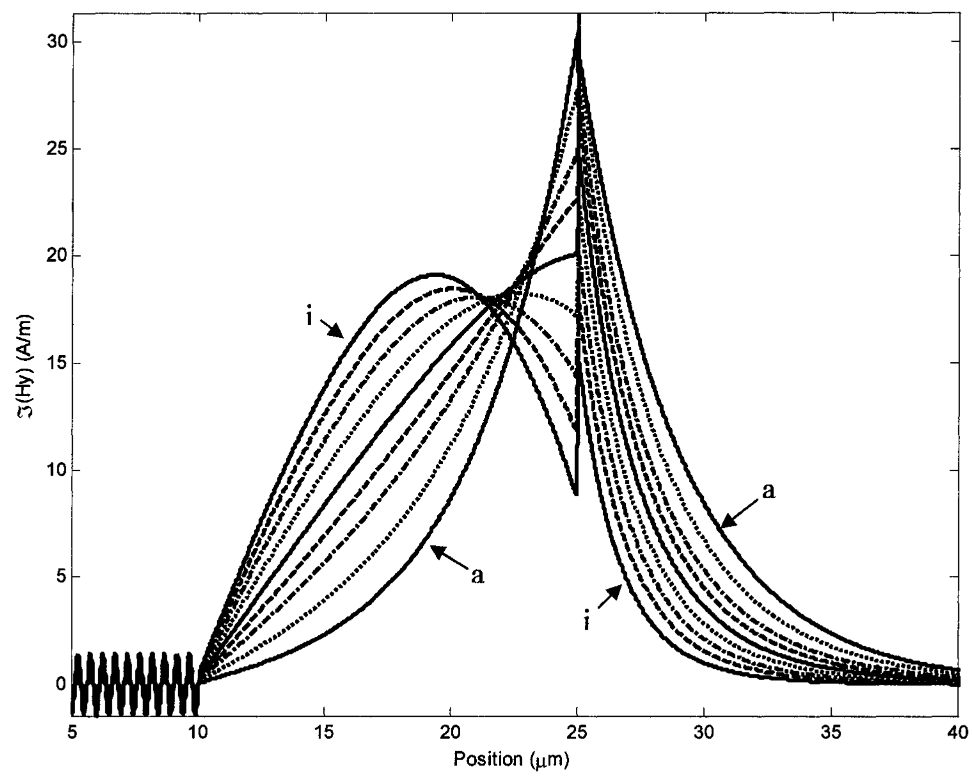

Figure 5.14: Imaginary part of the H_y field for the s_b mode as a function of the vertical position for a variety of injected current densities. Each curve is related to a particular current density and is identified by the letters "a" through "i". a) 1.33 GA/m^2 b) 40 GA/m^2 c) 53.33 GA/m^2 d) 60 GA/m^2 e) 66.66 GA/m^2 f) 73.33 GA/m^2 g) 80 GA/m^2 h) 86.66 GA/m^2 i) 96 GA/m^2. Silicon, silica, metal slab, polymer and air are located at $z<10\mu m$, $10\mu m<z<25\mu m$, $25\mu m<z<25.015\mu m$, $25.015\mu m<z<150\mu m$, $z>150$ respectively.

Figure 5.15 represents the real part of the Ex field for the s_b mode as a function of "z" position for a variety of injected current density. Each curve is related to a particular current density and is identified by the letters "a" through "i". By looking at Equation (5.6), it is clear that the Figure 5.15 is essentially the derivative of Figure 5.13.

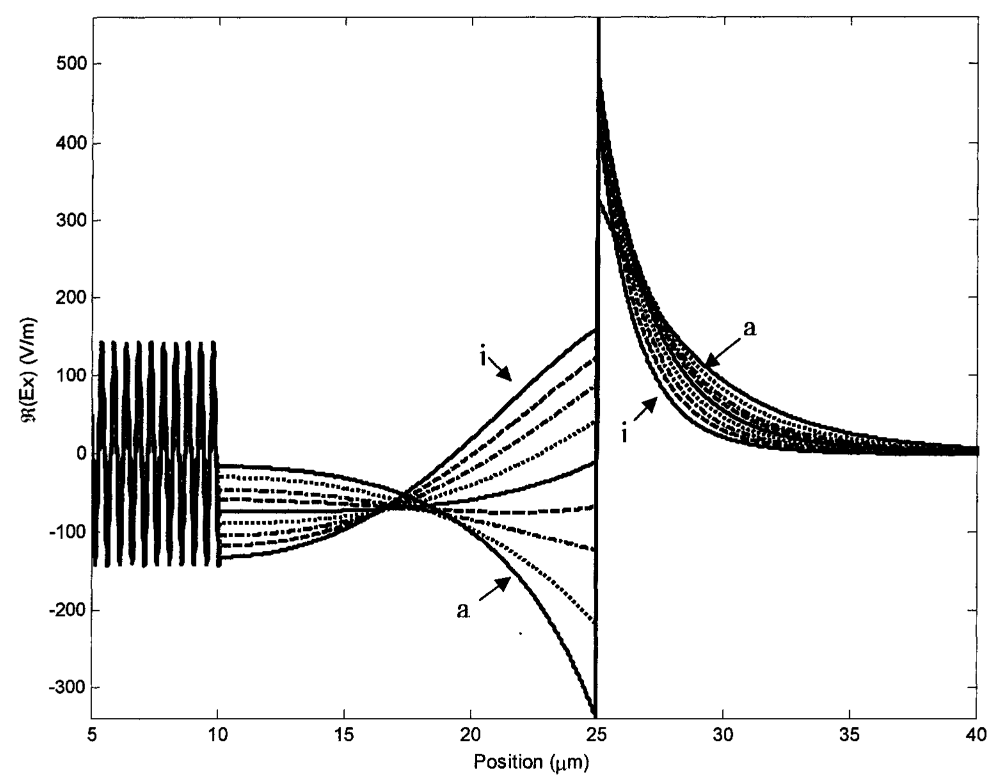

Figure 5.15: Real part of the Ex field for the s_b mode as a function of the vertical position for a variety of injected current densities. Each curve is related to a particular current density and is identified by the letters "a" through "i". a) 1.33 GA/m^2 b) 40 GA/m^2 c) 53.33 GA/m^2 d) 60 GA/m^2 e) 66.66 GA/m^2 f) 73.33 GA/m^2 g) 80 GA/m^2 h) 86.66 GA/m^2 i) 96 GA/m^2. Silicon, silica, metal slab, polymer and air are located at z<10μm, 10μm<z<25μm, 25μm<z<25.015μm, 25.015μm<z<150μm, z>150 respectively.

Figure 5.16 represents the imaginary part of the Ex field for the s_b mode as a function of "z" position for a variety of injected current densities. Each curve is related to a particular current density and is identified by the letters "a" through "i". This figure is essentially the derivative of Figure 5.14 as is apparent from Equation (5.6).

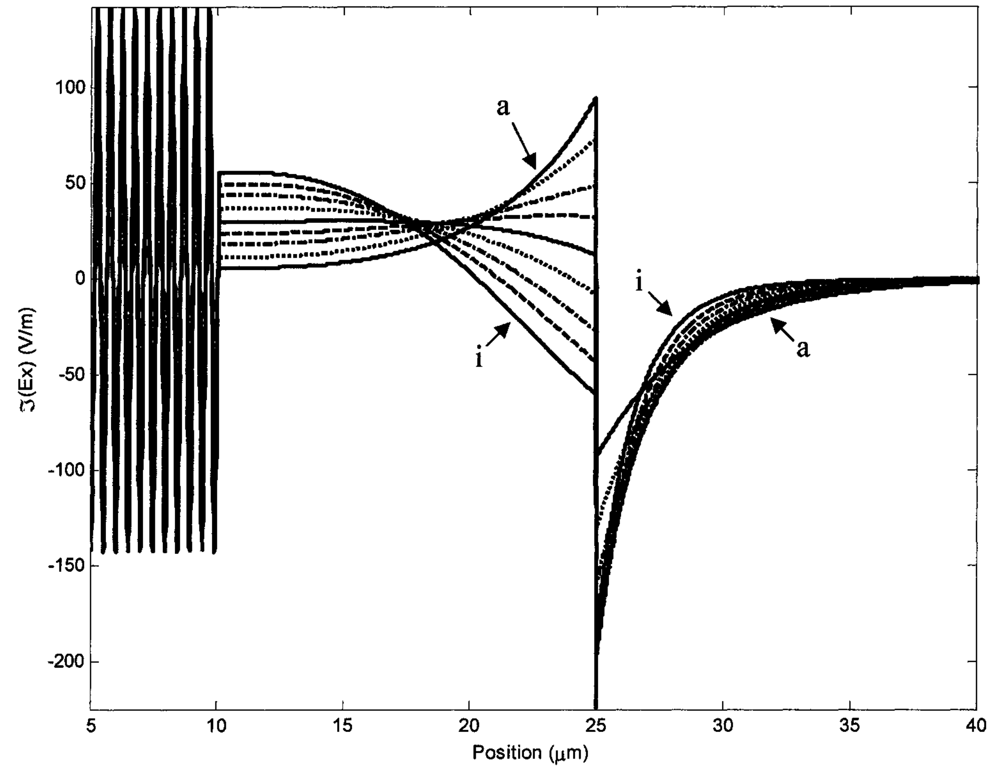

Figure 5.16: Imaginary part of the Ex field for the s_b mode as a function of the vertical position for a variety of injected current densities. Each curve is related to a particular current density and is identified by the letters "a" through "i". a) 1.33 GA/m^2 b) 40 GA/m^2 c) 53.33 GA/m^2 d) 60 GA/m^2 e) 66.66 GA/m^2 f) 73.33 GA/m^2 g) 80 GA/m^2 h) 86.66 GA/m^2 i) 96 GA/m^2. Silicon, silica, metal slab, polymer and air are located at $z<10\mu m$, $10\mu m<z<25\mu m$, $25\mu m<z<25.015\mu m$, $25.015\mu m<z<150\mu m$, $z>150$ respectively.

Figure 5.17 represents the real part of the x component of the poynting vector of the s_b mode as a function of the "z" position for a variety of injected current density. Each curve is related to a particular current density and is identified by the letters "a" through "i". This is the optical power that is expected to come out at the end of the sample and can be detected by a CCD camera. The mode power distribution changes characteristics as the waveguide is heated. It starts with a mode that has sharp edges at its center decaying exponentially with distance from the waveguide and evolves to a TM mode as would be supported by a dielectric slab waveguide as shown in Figure 5.17.

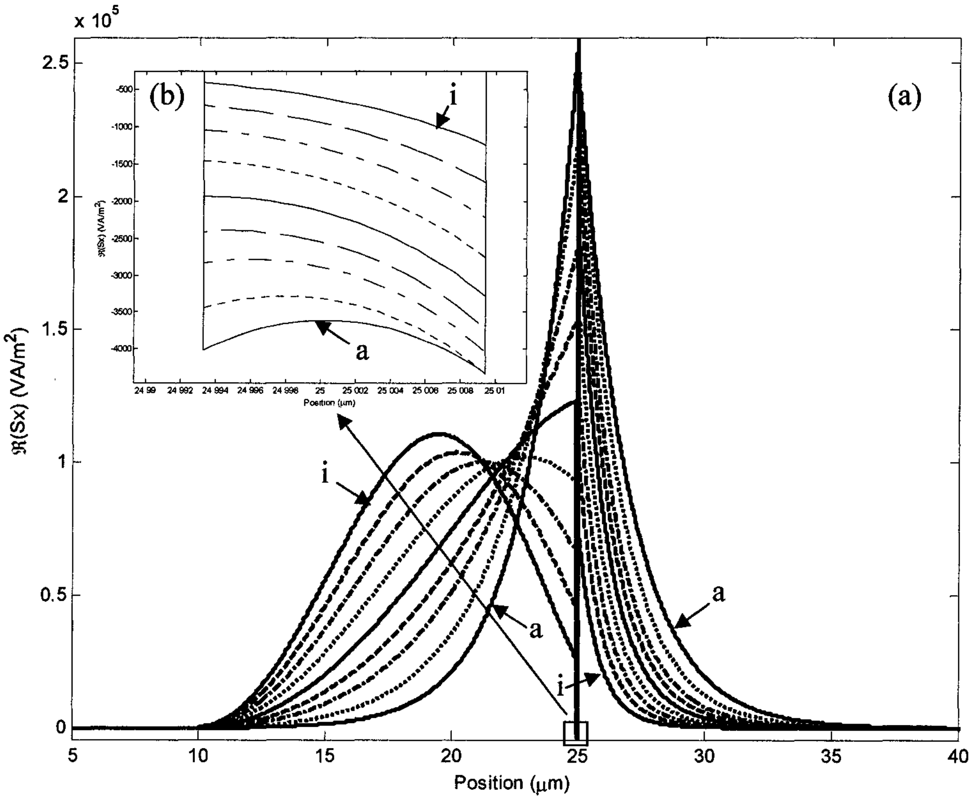

Figure 5.17: Real part of the x component of the Poynting vector of the s_b mode as a function of the vertical position for a variety of injected current densities. Each curve is related to a particular current density and is identified by the letters "a" through "i". a) 1.33 GA/m² b) 40 GA/m² c) 53.33 GA/m² d) 60 GA/m² e) 66.66 GA/m² f) 73.33 GA/m² g) 80 GA/m² h) 86.66 GA/m² i) 96 GA/m². Silicon, silica, metal slab, polymer and air are located at z<10μm, 10μm<z<25μm, 25μm<z<25.015μm, 25.015μm<z<150μm, z>150 respectively.

The phase velocity and group velocity are classically defined by:

$$v_p = \frac{\omega}{\beta} \tag{5.51}$$

$$v_g = \frac{d\omega}{d\beta} \tag{5.52}$$

Under general assumptions, the group velocity is also given by the ratio of the net power flow of the Poynting vector to the electromagnetic energy density [47]. It is interesting to see in Figure 5.17 that the real part of the power density is positive everywhere except inside the metal. This indicates that the power inside the metal propagates in the –x direction or contrapropagates with the phase. Equivalently, the phase velocity and group velocity will have a different polarity. This could potentially have interesting applications; however, it is not the objective of this thesis to investigate this phenomenon further.

Figure 5.18 represents the real part of the z component of the poynting vector from the s_b mode as a function of the "z" position for a variety of injected current density. Each curve is related to a particular current density and is identified by the letters "a" through "i. This figure shows the real power density propagating in the "z" direction.

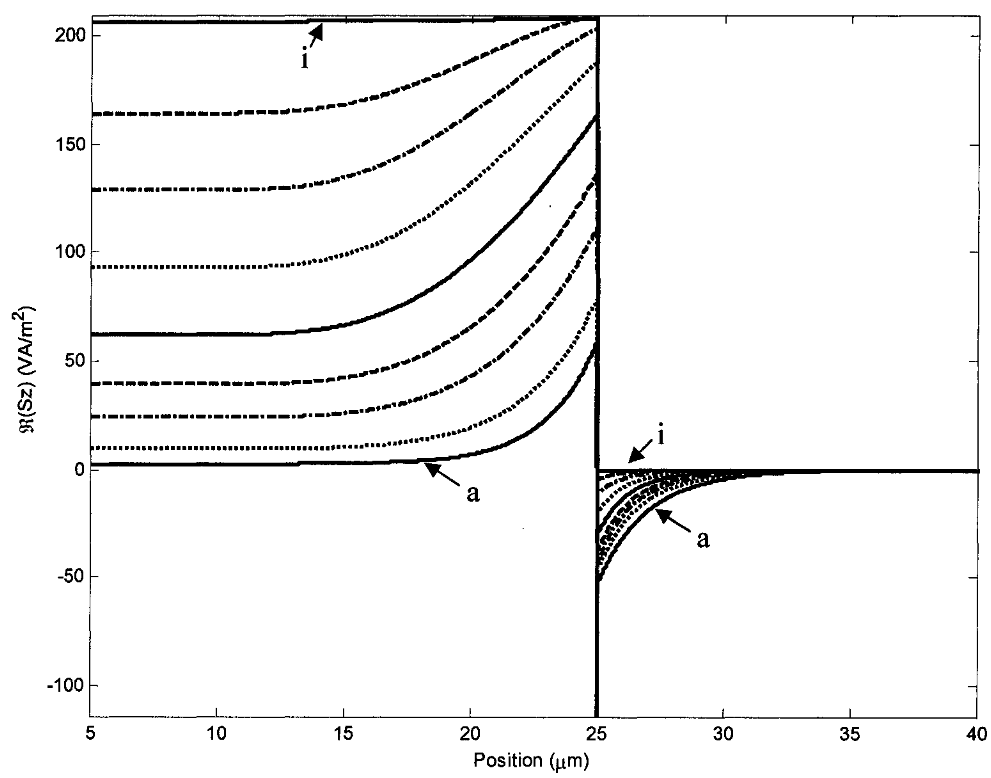

Figure 5.18: Real part of the z component of the Poynting vector of the s_b mode as a function of the vertical position for a variety of injected current densities. Each curve is related to a particular current density and is identified by the letters "a" through "i". a) 1.33 GA/m^2 b) 40 GA/m^2 c) 53.33 GA/m^2 d) 60 GA/m^2 e) 66.66 GA/m^2 f) 73.33 GA/m^2 g) 80 GA/m^2 h) 86.66 GA/m^2 i) 96 GA/m^2. Silicon, silica, metal slab, polymer and air are located at z<10μm, 10μm<z<25μm, 25μm<z<25.015μm, 25.015μm<z<150μm, z>150 respectively.

The combined results of Figures 5.16 and 5.17, show that the optical power flows at an angle towards the metal film, as required in order to remove energy from the dielectric media (for dissipation in the metal) as the wave attenuates with propagation distance [14].

Since the metal is the only lossy material in the system, it is to be expected that the propagating loss is proportional to the ratio of the optical power contained within the metal relative to the power contained through space. This is represented by the confinement factor:

$$cf = \frac{\int_b^a S_x(z)dz}{\int_{-\infty}^{\infty} S_x(z)dz} \tag{5.53}$$

where $S_x = -\frac{1}{2}E_z H_y^*$ for our waveguide. The core of the waveguide is assumed to be between "a" and "b". The confinement factor as a function of injected current density is shown in Figure 5.19. This is consistent with the propagation loss or mode power attenuation shown in Figure 5.8 (a) or (c) respectively.

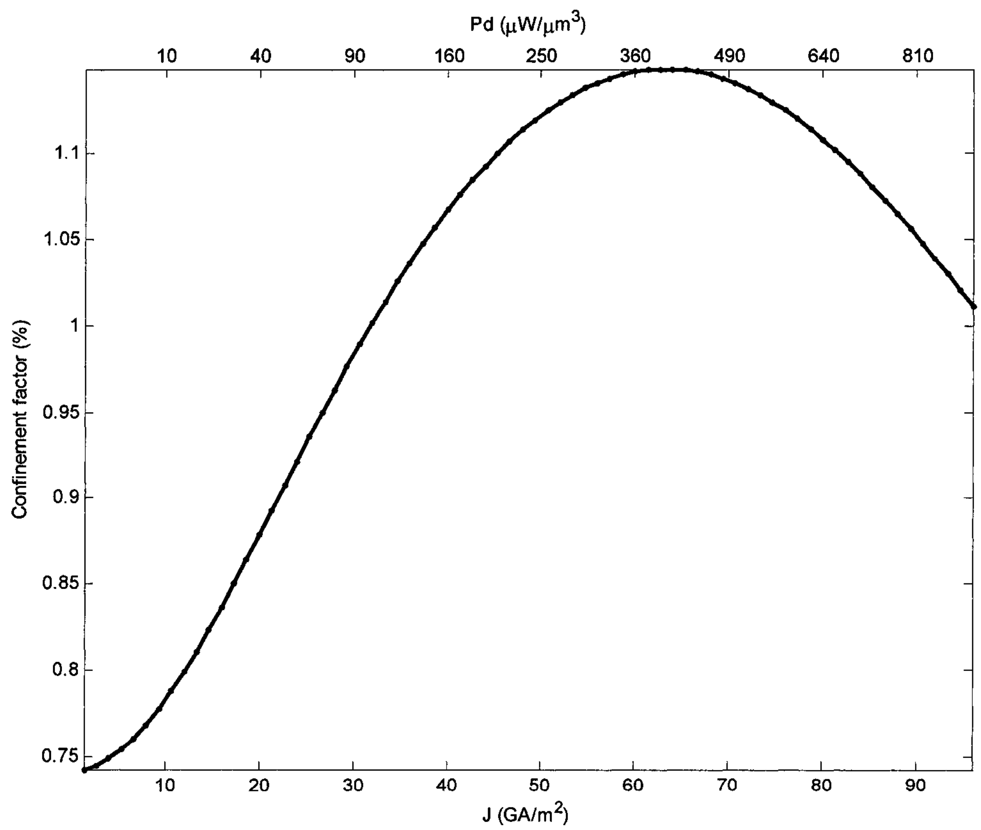

Figure 5.19: Confinement factor as a function of injected current density. The applied heating power density as shown by the scale on top of each figure is nonlinear and represented by Pd=J^2/σ.

In summary, the results of chapter 5 for this particular structure reveal that, when the slab is heated, the refractive index of the polymer is reduced displacing the optical power of the s_b mode supported by the waveguide towards the silica. The lower refractive index of polymer and much higher refractive index of silicon in comparison to silica confine the optical power within the silica. This confinement occurs because light propagates essentially parallel to the material interfaces. Eventually, when the waveguide is sufficiently heated near its cutoff, most of the optical power is displaced in the silica and a mode similar to the TM mode supported by the polymer-silica-silicon structure (without considering the thin metal film) becomes supported.

As the optical power is transferred to the silica, the confinement factor increases at first, but then reduces as the waveguide is further heated. Hence, the same occurs for the normalized attenuation constant. In addition, the normalized phase constant evolves from that of the metal optical waveguide to that of the TM mode supported by the dielectric structure; the normalized phase constant is reduced. As the power is transferred to silica, the mode field diameter evolves from that supported by the metal optical waveguide to that of the TM mode supported by the dielectric structure as shown in Figures 5.17 and 5.10 (b); the mode field diameter increases.

Because the optical power is displaced into the silica, it is expected that the coupling loss between this mode and that of a PMF centered at the metal waveguide will increase. As heat is applied, the propagation loss contribution to the IL decreases while that of the coupling loss increases. As a result, the IL increases from the dominating effect of the coupling loss at high heating power.

It was shown that when the slab waveguide is heated, the mode of the metal optical waveguide evolves into that of a TM mode supported by the dielectric structure. This would not occur if silicon were replaced by another heat sink whose refractive index is matched to silica. In such a situation, the optical power would most likely radiate, since the mode supported by the metal optical waveguide is almost cutoff. As a result, the metal slab structure should have a much better ER than obtained from the optical simulations. For the same reason, the performance of the finite width waveguide should be improved by doing the same to its structure. Partial evidence of this behavior was observed in the laboratory [38].

By comparing the experimental results with the optical model, we observe that they are different. More experimentation could be conducted to strengthen measurements of the propagation loss, coupling loss, IL and mode field diameter measured in the laboratory. It is known from simulations that the confinement of a metal slab waveguide is higher than that of a finite width waveguide [24]. For this reason, it is expected that the ER and coupling loss obtained from a 2D optical model be higher than that obtained from our 1D model. Also, the mode field diameter should be larger and the propagation loss lower.

Assuming a 8 μm x 15nm x 7.28mm waveguide where a 4.44 mm section is heated, the power consumption at cutoff of the mode (96 GA/m^2) is 491mW at which point an ER of about 5.25dB (or around 11.89dB by considering the 2D coupling loss explained earlier) is predicted by the model. In the laboratory, the maximum current density considered was 66.66GA/m^2 where any more current density injected could destroy the waveguide. With this in mind, with a power consumption of 236 mW (or 66.66 GA/m^2), an ER of only 2.50dB (or around 2.9 dB by considering the 2D coupling loss) is predicted by the model. For the 8μm wide waveguide, an ER of about 19dB was achieved with 222 mW in the laboratory. We see that there are large discrepancies between the s_b mode model and experimental results.

The 1D simulations showing that the mode of the metal waveguide evolves to the TM mode supported by the dielectric structure did predict the behavior of the finite width waveguide when its structure is uniformly heated with a TEC.

On the other hand, the optical model did not predict the behavior of the optical mode supported by the finite width waveguide when current is injected through. As the heating was applied, it appeared as if the optical output dimmed instead. This assumes that the effect of thermal expansion was negligible in the experiments; otherwise, because the fibers were not bonded onto the sample, the misalignment would be the main contribution to the discrepency. After reflection, the main difference between the results is because the optical model is 1D while the real structure is 3D (or its cross-section is 2D). In the optical model, the slab is heated and the polymer's refractive index is decreased while that of the silica is increased uniformly along the whole width of the slab. The optical power has no choice but to be displaced towards the silica (insignificant radiative modes supported by the structure). On the other hand, in the real structure, when the waveguide is heated, the polymer's refractive index is only reduced near the waveguide, as does the increase of refractive index in silica. Further from the waveguide, the refractive index of the polymer and silica are matched. In this particular refractive index distribution, the optical mode may leak laterally and from the top. For this reason, the optical power need not be displaced into the silica as predicted the 1D model.

This discrepancy suggests that the 1D modal analysis is not sufficient to predict the behavior of finite width waveguides. It is possible that the model predicts the behavior of much larger waveguides, but their propagating losses are expected to be so high that they would not be useful devices. A more sophisticated model should be used to predict the waveguide's behavior such as a 2D modal analysis or 3D beam propagation method.

In addition, we wanted to verify if the second most significant mode, the s_L mode, supported by the waveguide could explain the discrepancy. The results of the s_L mode is presented in Appendix D and the results did not explain the discrepancy.

Other sources of errors are attributed to obtaining materials properties from the literature. In order to obtain accurate material properties, it is important to get them in experimental conditions that are most representative of ours. Furthermore, unless material deposition conditions are not exactly the same, it is expected that the material property will differ. Unfortunately, it is almost impossible to reproduce exactly the same deposition conditions. This is why it is most appropriate to measure the material properties of your particular sample if the instrument and resources are available. Unfortunately, most of the time, the resources and instruments were not available to do so. We had to rely on the literature or make estimates based on the literature. Often bulk values were given, but not for the thin film situation, which can be significantly different.

As the waveguide is heated, it was proven in the laboratory that the thin metal film's electrical resistivity increases. The resistivity increase was not accounted for in the thermal and optical model.

Conclusion

Summary

The TO effect within the plasmon-polariton waveguide was shown to work for the first time. The metal optical waveguide was heated due to ohmic losses when a high current density was injected through. The maximum temperature of the waveguide is at its core and reduces with distance from it. As a result, the refractive index near the waveguide increased or reduced according to the temperature increase and TOCs. In effect, a refractive index asymmetry was introduced in the structure, which could cutoff the optical mode supported by the waveguide.

Given that the optical power has a similar distribution to that of the heat, it was expected that the device would consume less electrical power to achieve the same ER as other TO VOA devices. In fact, the prototype achieved an ER of 19dB with 222 mW of electrical power, a performance slightly worse than competing TO VOAs. However, it is expected that a few modification to the current design could improve the performance of the device and achieve the initial expectation.

The response time of the device was shown to be as quick as 50μs, which is faster than most other competing technologies. The IL of the device is shown to be quite high given the lossy nature of the metal. It is expected however, that the propagation losses of the finite width waveguide be lower than 11.83dB/cm from comparisons with other measurements [40]. The mode field diameter was also determined.

The change in resistivity of metals as a function of temperature was used to calibrate the waveguide as a temperature sensor, which was subsequently used to determine non-invasively, directly and accurately the temperature of the waveguide when heat is applied.

Given the high current densities injected into the waveguide, we investigated its degradation due to electromigration. Short-term experiments showed that degradation could occur at around 110 GA/m^2. Long-term experiments could show that the threshold electromigration current density is in fact lower, which is consistent with values reported from other authors. It was determined that the optical output dimmed as the metal film degraded due to electromigration. For this reason, we propose a new method of investigating the degradation of metals due to electromigration. The waveguide was shown to be very sensitive to the destructive nature of ESD. Precautions had to be taken to prevent the waveguide from being destroyed from this phenomenon.

In this work, we attempted to predict the behavior of the metal optical waveguide used as a TO VOA with a thermal and optical model. The waveguide was heated due to ohmic losses when a higher current density was injected through. It changed the refractive index of the polymer and silica surrounding it in such a way that the metal waveguide was cutoff and optical power was transferred into the silica; the new refractive index distribution of the dielectric slab structure supports a TM mode because of the presence of the silicon having a high refractive index. However, these results obtained from the 1D optical model failed to predict the behavior of the real heated waveguide. A more elaborate 2D or 3D model should be used. On the other hand, the model did predict the behavior of the waveguide when a refractive index asymmetry was introduced by heating the TEC given the uniformity of the temperature distribution along the horizontal axis.

Contributions

This thesis makes a number of contributions to the advancement of science and engineering. For the first time, an active capability is introduced to a new metal optical waveguide technology, in particular, the TO effect. The TO effect is used to affect the electromagnetic field propagating through a waveguide; hence, it can be used to modulate or attenuate an optical signal. A VOA based on mode cutoff is a relatively new concept within TO applications and the present thesis suggests a novel way of achieving this. The metal optical waveguide technology simplifies fabrication of active devices since the electrical and optical function is agglomerated into a single waveguide layer. The metal optical waveguide used as a heater influences light more efficiently than that of conventional thin film heating technologies. The heat source is already in the optical path such that little heat diffusion is needed to affect the optical mode substantially; however, heat diffusion is necessary for cooling. It follows that the device size, power consumption and switching time of the device may be reduced in comparison to other conventional PLC TO VOA technologies. Some inherent properties of the metal optical waveguide enable accurate, direct and non-invasive temperature monitoring of the device, which may be useful for TO devices. Electromigation tests are conducted on the metal waveguide and a new qualitative optical method to monitor the degradation of thin films due to electromigration is suggested and experimented as this method is an alternative to the resistance measurements and scanning electron microscopy. The failure of the 1D modal analysis to predict the waveguide's behavior suggests that a more elaborate optical model be used such as a 2D or 3D model.

Suggestion for future work

Resulting from this thesis, we have a few suggestions for future work. It was shown that the presence of silicon a heat sink having a refractive index unmatched to silica would prevent some optical power to escape the TO VOA when heated. As a result, the ER and electrical power consumption could be improved if we would replace silicon with another heat sink having a refractive index matched to the lower cladding.

A major disadvantage of our design is that we are using multiple materials with different TOCs. This is a problem because, although the device works at ambient temperature, it would not achieve the desired performance throughout the range of operating temperature. For this reason, the device must be temperature stabilized in some sort of way. This increases the complexity and cost of building the device. Furthermore, the temperature stabilization process consumes electrical power. Therefore, the total power consumption of the device is seen to increase significantly and cannot compete with other TO VOA devices not requiring temperature stabilization.

Our suggestion is to build a TO VOA, in which the metal optical waveguide is embedded into a single material having a large negative TOC (such as a polymer). The VOA function would not be implemented on the principle of refractive index asymmetry. Instead, when the waveguide is heated, it introduces a large refractive index gradient all around the waveguide. Assuming a negative TOC of the material, the refractive index near the waveguide would be much lower than that further from the waveguide. Consequently, the optical power would tend to propagate away from the waveguide where the refractive index is higher causing the waveguide to cutoff. Independent of the ambient temperature, the refractive index near the metal is uniform; only the refractive index gradient from heating the waveguide can cause its mode to be cutoff.

Another major disadvantage of the waveguide is its polarization sensitivity. The device is limited to applications where the input optical power is TM polarized. A waveguide having a square geometry is known not having this problem [21]. In order, for this square metal optical waveguide not to have significant losses, its size must be around 200 nm x 200 nm. However, we would need to investigate if such small metal cross-section can support enough current to heat the waveguide sufficiently to achieve useful attenuation.

In order to model the behavior of the waveguide properly, I suggest to use at least a 2D optical model. However, in particular, I suggest using the 3D beam propagation method. Since BPM for metal optical waveguides has never been developed before, we will have to do so before using it for our metal optical waveguide. This method can model the transients and the effect of the multiple modes that are supported by the waveguide in addition to considering its multiple dimensionalities. The disadvantage of this method is that it would require long periods of simulations, but it is probably one of the only ways to model the waveguide adequately.

Bibliography

[1] E. D. Palik, G. Ghosh, “Electronic Handbook of Optical Constants of Solids”,Academic Press ,1999.

[2] Sang-Shin Lee et Al., “Variable Optical attenuator based on a cutoff modulator with Tapered Waveguides in Polymers”, Journal of lightwave technology, Vol. 17, No. 12, December 1999.

[3] Kowalczyk et al. “Anti-waveguide Routing Structure”, U.S. Pat. No. 6,507,681 B1, January 14, 2003.

[4] Bischel et al,. “Device and Method for Variable Attenuation of an Optical Channel”, U.S. Pat. No. 2002/0018636 A1, February 14, 2002.

[5] Yasuhiro Hida et Al “Polymer Waveguide Thermooptic Switch with Low Electric Power Consumption at 1.3μm” IEEE Photonics Technology Letters, vol. 5, No. 7, July 1993.

[6] R. R. Hayes, “Thermally Driven Optical Switch Method and Apparatus”, U.S. Pat. No. 5,173,956, December 22, 1992.

[7] A. D. Boardman, “Electromagnetic Surface Modes”, John Wiley & Sons, pp. 1-75,1982.

[8] Ashcroft, Mermin, “Solid state Physics”, Saunders College,1976,pp.1-27.

[9] Fano, U., Journal of the Optical Society of America, Vol. 31, pp.213, 1941.

[10] Zenneck, Journal of the Annals of Physics, Vol. 23, p.846, 1907.

[11] Fuzi Yang et Al., “Long-range surface modes supported by thin films”, Physical Review B, volume 44, number 11, 15 September 1991

[12] A.Otto, :Excitation of Nonradiateive Surface Plasma Waves in Silver by the Method of Frustrated Total Reflection”, Zeitschrift fur Physik, 216, pp. 398-410, 1968.

[13] E. Kretchman et al., “Radiative Decay of Non Radiative Surface Plasmons Excited by Light”, Z. Naturforsch, 23 a, pp. 2135-2136, 1968.

[14] J. J. Burke, G.I. Stegeman and T.Tamir, “Surface-polariton-like waves guided by thin, lossy metal films”, Physical Review B, Volume 33, number 8, 15 April 1986.

[15] P. Berini, “Plasmon-polariton waves guided by thin lossy metal films of finite width: Bound modes of symmetric structures”, Physical Review B, Vol. 61, No. 15, April 15, 2000.

[16] P. Berini, “Plasmon-polariton waves guided by thin lossy metal films of finite width: Bound modes of asymmetric structures”, Physical Review B, Vol. 63, 4 May 2000.

[17] P. Berini, “Plasmon-polaritons modes guided by a metal film of finite width bounded by different dielectrics”, Optics Express, pp. 329-335, August 17, 2000.

[18] R. Charbonneau, P. Berini, “Long-Range Plasmon-Polariton wave propagation in thin metal films of finite width excited using an end-fire technique”, International Conference on the Application of Photonic Technology, ICAPT 2000, Proceedings SPIE, Vol. 4087, pp. 534-540, June 2000.

[19] R. Charbonneau et al., “Experimental observation of plasmon-polariton waves supported by a thin metal film of finite width”, Optics Letters, Vol. 25.,

Issue 11, pp. 844-846, June 2000.

[20] R. Charbonneau, "Demonstration of a passive integrated optics technology based on plasmons", Master's defense thesis, University of Ottawa, September 5th 2003

[21] P. Berini, "Optical Waveguide Structures", U.S. Pat. No. 2003/0059147 A1, March 27,2003.

[22] J. Zeng, G. Gagnon, Internal document, Spectalis Corp.

[23] R. Charbonneau, P. Berini, Private communication, Spectalis Corp.

[24] P. Berini, Internal document, Spectalis Corp.

[25] M. Paniccia et al.," Scanning probe microscopy studies of electromigration in electroplated Au wires", Journal of Applied Physics, 73, p. 8189, 1993.

[26] M. B. Kleiner et al. "Thermal Conductivity Measurements of Thin Silicon Dioxide Films in Integrated Circuits", IEEE Transactions on Electron Devices, Vol. 13, No. 9, September 1996.

[27] www.jahm.com Material property database (MPDB) software

[28] J. Hartmann et al.,"Measuring Local Thermal Conductivity in Polycrystalline Diamond with a High Resolution Photothermal Microscope", Journal of Applied Physics, 81, 7, April 1, 1997.

[29] www.nyelubricants.com Curing optical gel OCK-433 data sheets.

[30] C. Hu et al.,"Thermal conductivity and interfacial thermal resistance of polymeric low k films", Applied Physics letters,Vol.79, No. 25, December 17, 2001.

[31] C. Durkan et al.,"Size effects in the electrical resistivity of polycrystalline nanowires", Physical Review B, Vol 61, No. 20, 15 May 2000.

[32] P. Berini et al., "Conductors, electric" Wiley

[33] A. S. Oates, "Electromigration transport mechanisms in Al thin-film conductors", Journal of Applied Physics, Vol. 79, No. 1, January 1, 1996.

[34] M.F. Chisholm and al. "Electromigration studies in amorphous and polycrystalline alloys", Applied Physics Letters, Vol. 53, No. 2, July 11, 1988.

[35] K.P. Rodbell and al., "Reduction of electromigration in gold thin films in the presence of hydrogen", Applied Physics Letters, Vol. 47, No. 9, November 1, 1985.

[36] M.A. Kelly, and al., "An Investigation of Human Body Electrostatic Discharge", ISTFA '93: The 19th International Symposium for Testing & Failure Analysis, Los Angeles, California USA/15-19 November 1993.

[37] Electrostatic Discharge Association, http://www.esda.org/esdbasics1.htm

[38] R. Charbonneau, P. Berini, Internal document, Spectalis Corp.

[39] TIA-455-78-B IEC 60793-1-40 "Measurement Methods and Test Procedures – Attenuation"

[40] C. Cardarelli, R. Charbonneau, P. Berini, Internal document, Spectalis Corp.

[41] www.thorlabs.com PDA-400 Data sheets

[42] FOTP-107, TIA/EIA-455-107A, "Determination of component reflectance or link/system return loss using a loss test set.

[43] D Poulikakos, "Conduction Heat Transfer" Prentice Hall, 1994, pp. 1-16

[44] Frank P. Incropera, David P. Dewitt, "Fundamentals of Heat and Mass Transfer", fourth edition, John Wiley & Sons, 1996, pp.1-181.

[45] Pierre Berini, ELG 5379 "Numerical Methods in Electromagnetic Engineering", Course Notes, 2000 Edition, University of Ottawa.

[46] Katsunari Okamoto, "Fundamentals of Optical Waveguides",Academic

Press, 2000, pp.125-131
[47] Pierre Tournois et. Al., "Negative group velocities in metal-film optical waveguides", Optics Communications, No.137, 1997, pp.41-45
[48] C. Vassallo, "Orthogonality and Normalization of Radiation Modes in Dielectric Waveguides: an Alternative Derivation", Journal of the Optical Society of America, p.680, May 1983.

Appendix A: Proof

The goal of this section is to prove that the temperature measured by the thermistor lying on top of the TEC is approximately the same as that located at the waveguide level. The TEC's temperature is relatively uniform along its whole surface because the material on which the sample lies is very thermally conductive. However, near its edges, the temperature is not uniform. The TEC is surrounded by air, which is a very good thermal insulator as long as convection is negligible. As mentioned in chapter 3, the thermistor was bonded to the TEC via a thermal conductive epoxy. The thermistor was placed near the center of the TEC away from its edges. In addition, the sample was placed near the thermistor. As stated in section 3.2.1, a silver based thermally conductive compound was spread on the TEC such that, when a sample is positioned firmly on its surface, the compound will fill the voids at the sample-TEC interface and reduce the interface's thermal contact resistance. The temperature of the sample is therefore assumed uniform on a given plane. The thermal disturbance due to the metal waveguide is assumed negligible given its small cross-section relative to that of the other layers constituting the sample's structure. Because the thickness of the structure is small compared to its width and length in addition to the small metal cross-section, an analytical 1D model should closely approximate the temperature at the waveguide level. The heat flux flowing through the structure is governed by the following equation:

$$q''=\frac{T_{tec}-T_{\infty}}{\frac{l_1}{k_1}+\frac{l_2}{k_2}+\frac{l_3}{k_3}+\frac{1}{h_4}} \tag{A.1}$$

where q'', T_{tec} and T_{∞} are the heat flux flowing through the layers of the structure, the temperature at the surface of the TEC and the ambient temperature respectively. The worst case scenario is considered. In our experiments, the maximum temperature of the TEC is 60°C and the room temperature is 20.3°C most of the time. k_1, k_2, k_3 have been estimated as 145 $\frac{W}{m.K}$, 1.1 $\frac{W}{m.K}$ and 0.14 $\frac{W}{m.K}$ respectively. l_1 and l_2 are known to be 600μm and 15μm respectively. The gel is thick and has low thermal conductivity such that its non-uniform thickness should have negligible impact on the waveguide layer's temperature. The gel thickness varied from sample to sample. The average thickness of the gel was 800μm thick.

Therefore, l_3 is set to 800μm. The free convection coefficient h_4 ranges between 2 and 25 for gases such as air. h_4 has been set to 25 for the worst case evaluation. The flux "q''" was determined from the previous equation and used in the following equation to determine the temperature at the waveguide layer.

$$T_{tec} - T_3 = q''\left(\frac{l_1}{k_1} + \frac{l_2}{k_2}\right) \tag{A.2}$$

where T_3 is the waveguide layer's temperature. As a result, only a maximum temperature difference of 0.0156°C could occur between the thermistor and the waveguide layer. It is acceptable to assume both temperatures equal.

A simple experiment was conducted to confirm this result. The sample described in section 3.1.2 was placed on the TEC via a thermally conductive compound. The sample was heated at a temperature usually used during the experiments, which was near 28°C. As explained above, the temperature of the sample should be uniform on a given plane; a thermo-couple placed at the waveguide layer (through the gel) is not believed to perturb the measurement significantly. A thermo-couple was used to measure the ambient temperature, the TEC's temperature, the waveguide layer's temperature and the temperature on top of the polymer. The measured temperatures with the thermo-couple were 22.8°C, 28.6°C, 28.5°C and 27.5°C, respectively. The ambient and TEC temperatures measured by the thermistor were 22.25°C and 28.35°C respectively. The temperature measurements provided by the thermo-couple are not as accurate as the thermistor. Typically, the temperature varied as a function of time by as much as ±0.3°C, while for the thermistor, it varied by only ±0.01°C. This proves that the temperature measurements between the TEC and waveguide layer is believed to be less or equal to the precision of the measuring device. Hence, this is sufficient to show that the temperatures of the TEC and waveguide layer are close enough to justify assuming them equal.

Appendix B:Accelerating numerical computation

The purpose of this section is to present numerical methods that will significantly reduce the computation time required to generate results. In order to accelerate computation time, Gauss-Siedel method, Successive Overrelaxation (SOR) method, non-uniform meshes and multigrids are presented. In addition, because the computational domain has half-symmetry along the vertical center of the metal waveguide, only half of the domain needs to be computed.

The Gauss-Siedel method is an iterative method by which the equation used to generate results on a grid is done in a particular order. Computation is done such that newly-found results on the grid are used as soon as there are available for subsequent calculations; it consists of raster-scanning calculations through the nodes of the rectangular grid. We can apply Gauss-Siedel method to Equation (4.36) by raster-scanning calculations through the nodes of the rectangular grid in any order shown in Figure (B.1). Equation (B.1) is represented by Figure (B.1A).

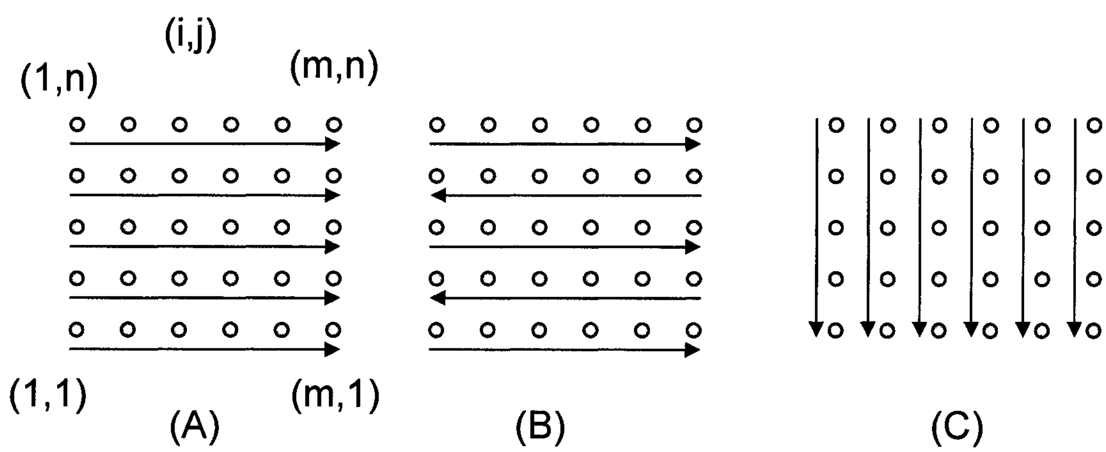

Figure B.1: Illustration of Gauss-Siedel method.

$$T^{k+1}(i,j) = \frac{T^{k+1}(i-1,j)A + T^{k}(i,j+1)B + T^{k}(i+1,j)C + T^{k+1}(i,j-1)D + Q_G{}^{k}(i,j)}{A+B+C+D} \quad \text{(B.1)}$$

"k" corresponds to the iteration number. For a thermal diffusion problem, which incorporates a single thermal source such as in this thesis, calculations converge more rapidly if raster-scanning starts at the source towards a direction that is most compatible with the power flux density's direction and the grid's mesh.

A node's temperature variation between successive iterations should vanish as "k" tends towards infinity and it is expressed by:

$$T^{k+1}(i,j) - T^{k}(i,j) = \varepsilon^{k}(i,j) \text{ [K]} \tag{B.2}$$

where $\left|\varepsilon^{m}(i,j)\right| < \left|\varepsilon^{n}(i,j)\right|$ for m>n.

Equation (B.1) is substituted into (B.2) and we obtain:

$$\varepsilon^{k}(i,j) = \frac{T^{k+1}(i-1,j)A + T^{k}(i,j+1)B + T^{k}(i+1,j)C + T^{k+1}(i,j-1)D + Q_G{}^{k}(i,j)}{A+B+C+D} - T^{k}(i,j) \tag{B.3}$$

Alternatively, Equation (B.2) may be expressed differently to give it another interpretation:

$$T^{k+1}(i,j) = T^{k}(i,j) + \varepsilon^{k}(i,j) \tag{B.4}$$

where a correction, $\varepsilon^{k}(i,j)$, is added to T^{k} to get T^{k+1}. However, we know that $\varepsilon^{k+1}(i,j)$ is non-zero except for "k" tending towards infinity. Therefore, the SOR method adds an overrelaxation factor, Γ, into the equation to apply an overcorrection and to accelerates the convergence. This is shown by:

$$T^{k+1}(i,j) = T^{k}(i,j) + \Gamma\varepsilon^{k}(i,j) \tag{B.5}$$

where $\varepsilon^{k}(i,j)$ comes from Equation (B.3)

A better choice of Γ leads to a faster convergence, but Γ usually lies between 1 and 2 for a thermal diffusion equation. There are many issues regarding the SOR method such as stability just to name one, but this is out of the scope of this thesis.

Generally, a coarse uniform mesh will generate results converging rapidly but its accuracy will be poor if data values vary quickly within that region. Conversely, a dense uniform mesh will generate results accurately but its convergence will be slow. A solution to this problem is to make the mesh dense only in regions where data values vary rapidly; hence, a non-uniform mesh. In FDM such as presented in section 4.2, it is important that the mesh density does not vary too rapidly, otherwise, it may produce numerical errors. For this reason, a 2D geometric progression separating each points of the mesh is selected.

A 1D geometric progression takes the form:

$$h_n = h_1\eta^{n-1} \tag{B.6}$$

where h_1, h_n and η are the first and nth spacing between nodes and the geometric factor, respectively. The total distance of the whole geometric progression is defined by:

$$\Phi = \sum_{n=1}^{N} h_n \tag{B.7}$$

where "N" is the total number of spacings. h_1, h_N and Φ are usually given while "N" and η are determined numerically. η is typically kept between 1 and 1.1, otherwise, the mesh density variation occurs too rapidly. The case of η=1 is a uniform grid. Usually, it is impossible to obtain h_1, h_N and Φ exactly for given values "N" and η. Consequently, numerical computation determines a value $\hat{h}_N$, which is close to h_N within a given tolerance. This equation can be applied individually in each dimension to obtain the 2D case. Once each h_n is determined via Equations (B.6) and (B.7), it can be introduced to the mesh defined by the FDM derivation through:

$$h\,(\theta_a+\theta_b)=h_n \tag{B.8}$$

where "h" is an arbitrarily chosen parameter constant throughout the domain. θ_a and θ_b may be any of the θs shown in Figure 4.2. It is the θs that vary such that the result is equal to h_n.

As a starting condition, if all the points of the grid are set at a temperature near the real solution, the result will converge more rapidly than if they are all set to 0 or any arbitrary value. Hence, in order to accelerate convergence a coarse mesh is used to compute quickly an approximate result. The result from the coarse mesh is transferred to a denser mesh via interpolation and it is used as the starting condition for the calculations of the denser mesh; it is called a multigrid method. This is done iteratively until the desired accuracy is obtained.

If the structure has half-symmetry, there is no thermal power flux crossing the plane of symmetry. Consequently, the plane of symmetry can be considered adiabatic. An adiabatic boundary condition is set at the plane of symmetry and only half of the domain needs to be computed. When half of the domain is computed, the result can be mirror-reflected to the other side of the plane of symmetry to obtain that of the full domain. All of these techniques are programmed in the computer to save substantial amount of computation time.

Appendix C: Muller's complex root finding method

Muller's root finding method is a method by which the root of a given function is approximately determined by finding the root of a curve passing by three points on that function. The new approximate root has a corresponding value of abscissa. The function is evaluated at that abscissa value. Only the three values of abscissa nearest the true root are kept for the next iteration of the method. The approximate root becomes more accurate as the number of iterations increases. When the approximate root lies within a given tolerance of the true root, the method is said to have found a solution. Equation (C.1) describes the curve passing through three points of the function. Given three points x_0, x_1 and x_2, the parameters of Equation (C.1) may be determined.

$$a(x-x_0)^2+b(x-x_0)+c=f(x) \tag{C.1}$$

$$c=f(x_0) \tag{C.2}$$

$$a(x_1-x_0)^2+b(x_1-x_0)+c=f(x_1) \tag{C.3}$$

$$a(x_2-x_0)^2+b(x_2-x_0)+c=f(x_2) \tag{C.4}$$

Solving for "a", "b" and "c" yields:

$$a=\frac{\gamma f(x_1)-f(x_0)[1+\gamma]+f(x_2)}{\gamma h_1^2[\gamma+1]} \tag{C.5}$$

$$b=\frac{f(x_1)-f(x_0)-ah_1^2}{h_1} \tag{C.6}$$

$$c=f(x_0) \tag{C.7}$$

Equation (C.1) is quadratic and its roots may be determined easily. There are two solutions to the equation and the one closest to x_0 is chosen. Given the finite nature of computers, care must be taken to make sure that there is not any subtractive cancellation leading to numerical errors in the calculation of the solution. Therefore, the solution to (C.1) is written in a particular form to eliminate this potential problem.

$$x_r=x_0-\frac{2c}{b+sign(b)\sqrt{b^2-4ac}} \tag{C.8}$$

Muller's method can find complex roots, because the argument under the root in the denominator of (C.8) may be negative.

Appendix D: s_L mode

The objective of this section is to analyze the behavior of the s_L mode as a function of injected current (or power density) through the metal waveguide such as was done for the s_b mode. The same structure that was explained in section 3.1.1 and 3.1.2 and used to analyze the s_b mode will also be used to analyze the s_L mode for comparison purposes.

The motivation for analyzing the s_L mode is as follows. When a waveguide is excited, the optical power that propagates along the waveguide will distribute itself amongst all its supported modes. The ratio of power distributed to each mode depends on many factors including the method by which the waveguide is excited. A modal analysis along with mode overlap calculations is not an effective way to determine the proportion of power distributed to each mode, but experimental evidence shows that most of the optical power remains in the s_b and s_L modes. All modes except the s_b and s_L modes have very high propagation loss; therefore, low IL of a 7 mm sample as obtained in the laboratory (section 3.4.1) can only be achieved if most of the optical power remains within these two modes. Furthermore, the asymmetric modes have field distributions that are incompatible with those of a PM fiber reinforcing the argument that most of the optical power remains in the symmetric modes.

Because the fields distribution of the s_L mode closely resemble those of the s_b mode, only those significantly different from that of the s_b mode will be presented. Furthermore, most of the comments applied to the s_b mode in section 5.3 will, in most part, be applicable to the s_L mode.

The fields $\Re(Ex)$, $\Im(Ez)$, $\Im(Hy)$, $\Re(Sz)$ found for the s_L mode are a 180° rotation of those of the s_b mode where the axis of rotation is the 0 absisa of these figures (refer to section 5.3). The other fields are similar than what is shown for the s_b mode. Another difference is that the oscillation amplitude of the fields in the silicon increase with decreasing z. In the polymer and silica there are only small differences in field amplitudes because the s_L mode evolves slightly differently than the s_b mode as more heat is applied.

An issue for the s_L mode is that normalization of the mode is ambiguous because the fields increase to infinity on the radiating side of the waveguide. Therefore, the coupling loss, MFD and IL model in chapter 5 cannot be appropriately determined. There is another way of deriving Maxwell's equations such that the leaky modes can be determined unambiguously [48], but this is out of the scope of this thesis since it will not generate significant results. The interpretation of the increasing fields with distance to the waveguide comes from spatial transients expressed in the steady-state results. The reader is referred to [14] for more details. In any case, this interpretation reveals that, in fact, the fields do not really increase to infinity. Since most of the fields distributions are similar than that of the s_b mode, it is expected that the coupling loss and MFD of the s_L mode be close to that of the s_b mode.

Figure D.1 presents the normalized phase constant of the s_L mode as a function of metal film thickness for a variety of injected current density into the plasmon-polariton waveguide. Each curve is related to a particular current density and is identified by the letters "a" through "L", where the successive letters are attributed to the decreasing curves.

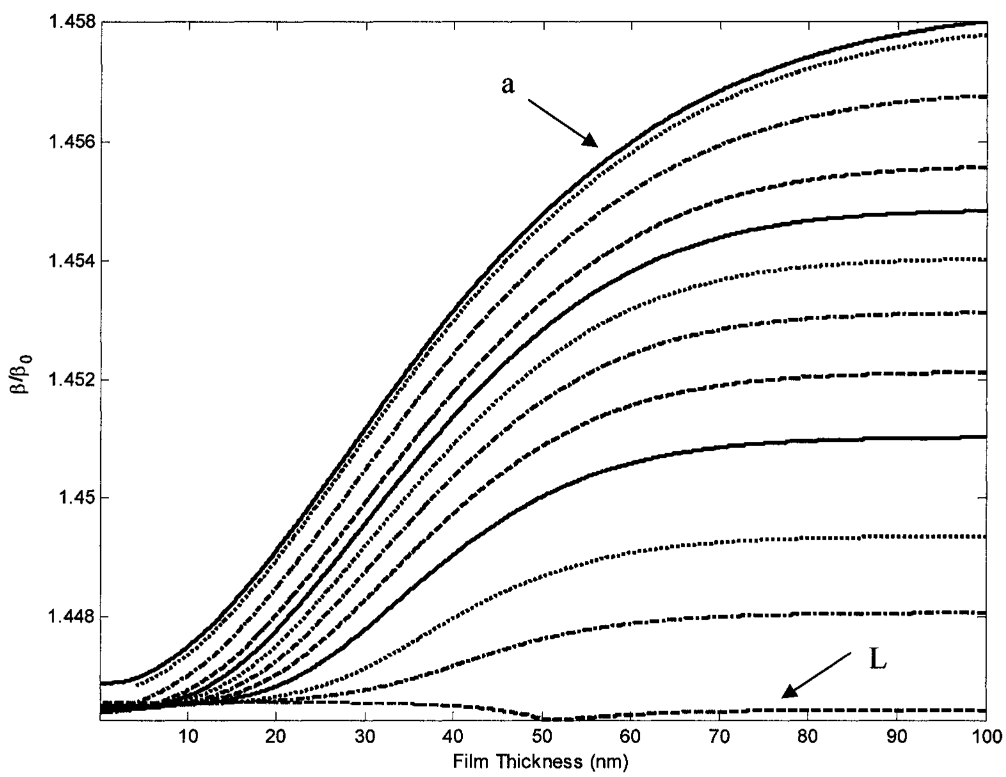

Figure D.1: Normalized phase constant of the s_L mode as a function of metal film thickness for a variety of injected current densities into the metal optical waveguide. Each curve is related to a particular current density and is identified by the letters "a" through "L", where the successive letters are

attributed to the decreasing curves. a) 1.33 GA/m^2 b) 20 GA/m^2 c) 40 GA/m^2 d) 53.33 GA/m^2 e) 60 GA/m^2 f) 66.66 GA/m^2 g) 73.33 GA/m^2 h) 80 GA/m^2 i) 86.66 GA/m^2 j) 96 GA/m^2 k) 102.6GA/m^2 l) 110.6 GA/m^2

Figure D.2 represents the normalized attenuation constant of the s_L mode as a function of metal film thickness for a variety of injected current densities into the plasmon-polariton waveguide. As can be observed, the s_L mode does not have a cutoff thickness like that of the s_b mode (although some curves are not complete because I had trouble with the numerical solver). As heating of the waveguide is increased, the normalized attenuation constant changes dramatically for thinner metal films.

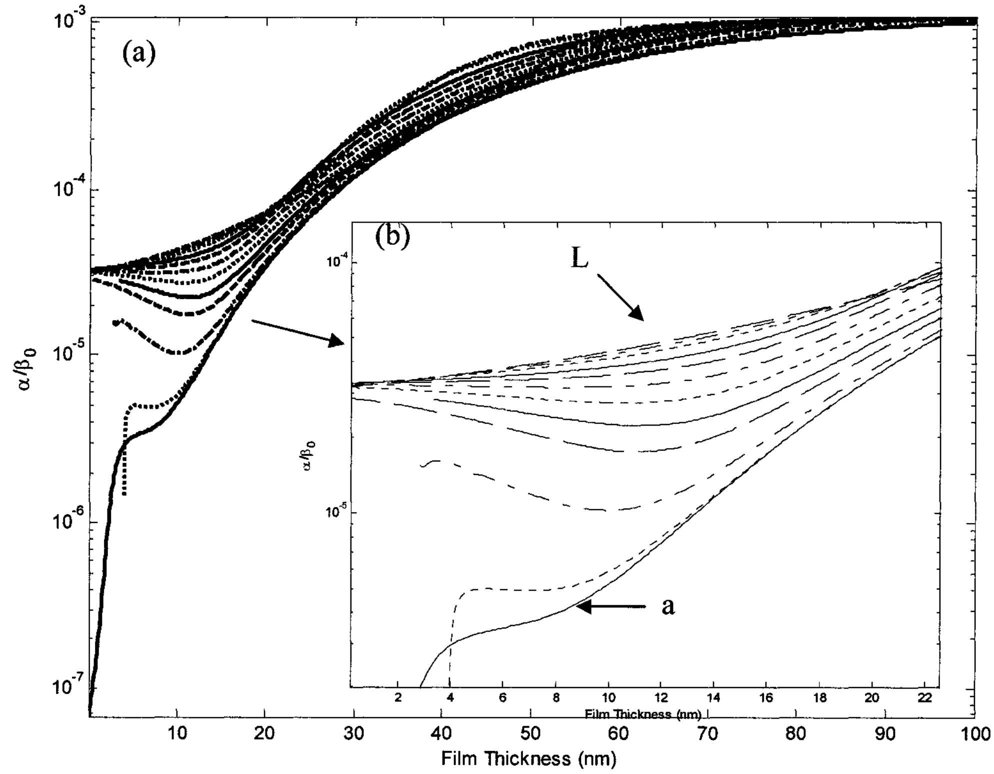

Figure D.2: Normalized attenuation constant of the s_L mode as a function of metal film thickness for a variety of injected current densities into the metal optical waveguide. . Each curve is related to a particular current density and is identified by the letters "a" through "L". The letters in Figure (b) are successive from bottom to top. a) 1.33 GA/m^2 b) 20 GA/m^2 c) 40 GA/m^2 d) 53.33 GA/m^2 e) 60 GA/m^2 f) 66.66 GA/m^2 g) 73.33 GA/m^2 h) 80 GA/m^2 i) 86.66 GA/m^2 j) 96 GA/m^2 k) 102.6GA/m^2 L) 110.6 GA/m^2

Figure D.3 shows the real part of the z component of the Poynting vector of the s_L mode as a function of the vertical position of the waveguide structure for a variety of injected current densities. In opposition to the s_b mode, some of the power in the s_L mode propagates away from the waveguide (radiates) as shown by the poynting vector in Figure D.3. By comparing Figure D.2 with Figure D.3, we quickly realize that the attenuation constant is comprised of two important loss mechanisms for the s_L mode: material loss and radiation loss. As was explained earlier, confinement is reduced for decreasing metal film, which leaves the mode more susceptible to radiation loss. This explains why heating influences the attenuation constant more dramatically for thinner metal films. The IL of the s_L mode in Figure D.4 is higher than that of the s_b mode attributable to radiation loss. For current density beyond 96GA/m^2, the s_b mode is cutoff and optical power must be transferred into the other existing modes. Due to the good mode overlap between the s_b and s_L mode, most of the optical power should be transferred to the s_L mode.

In a similar way than the s_b mode, when the waveguide is heated, the s_L mode evolves to that which resembles a TM mode supported by a dielectric structure. Even if power is transferred amongst both symmetric modes, it is not able to account for the fact that, in the experiments, we did not observe this dielectric mode.

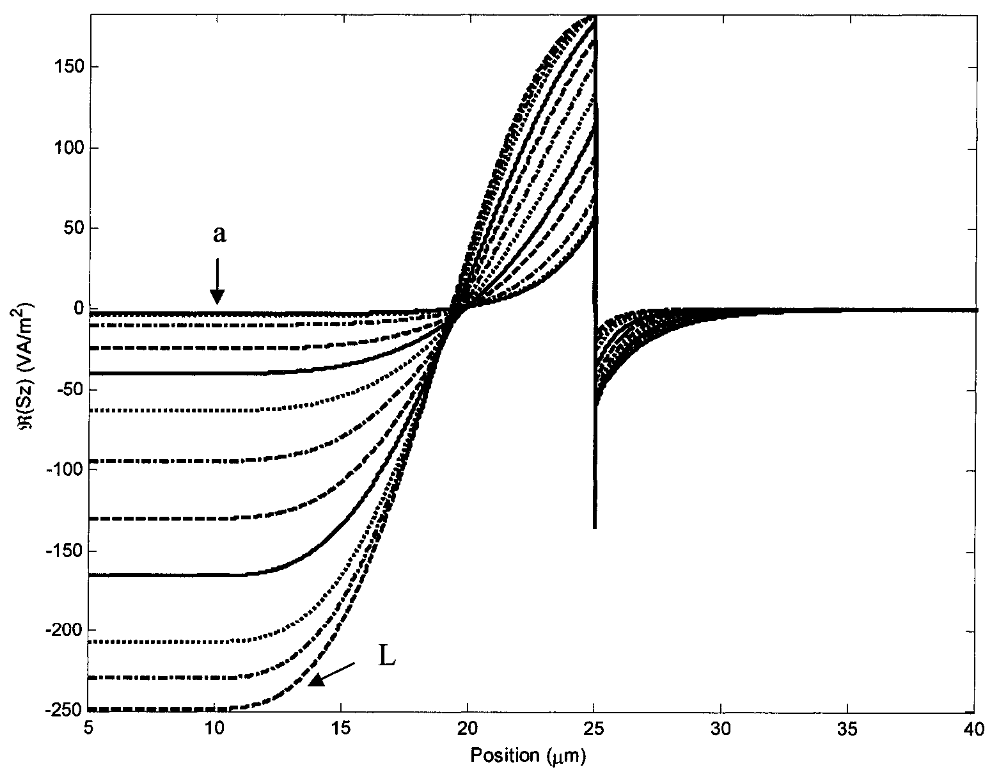

Figure D.3: Real part of the z component of the Poynting vector of the s_L mode as a function of the vertical position for a variety of injected current densities. Each curve is related to a particular current

density and is identified by the letters "a" through "i". a) 1.33 GA/m^2 b) 40 GA/m^2 c) 53.33 GA/m^2 d) 60 GA/m^2 e) 66.66 GA/m^2 f) 73.33 GA/m^2 g) 80 GA/m^2 h) 86.66 GA/m^2 i) 96 GA/m^2. Silicon, silica, metal slab, polymer and air are located at z<10μm, 10μm<z<25μm, 25μm<z<25.015μm, 25.015μm<z<150μm, z>150 respectively.

Figure D.4 (a), (b) and (c) represent the normalized attenuation constant, normalized phase constant and MPA of the s_L mode as a function of injected current density (or power density) for a 15nm thick metal film. Figure D.4 (c) illustrates the MPA as a function of applied current density through the plasmon-polariton waveguide. The figure shows that because the waveguide is radiating, its MPA can be much higher than that of the s_b mode for any applied heat.

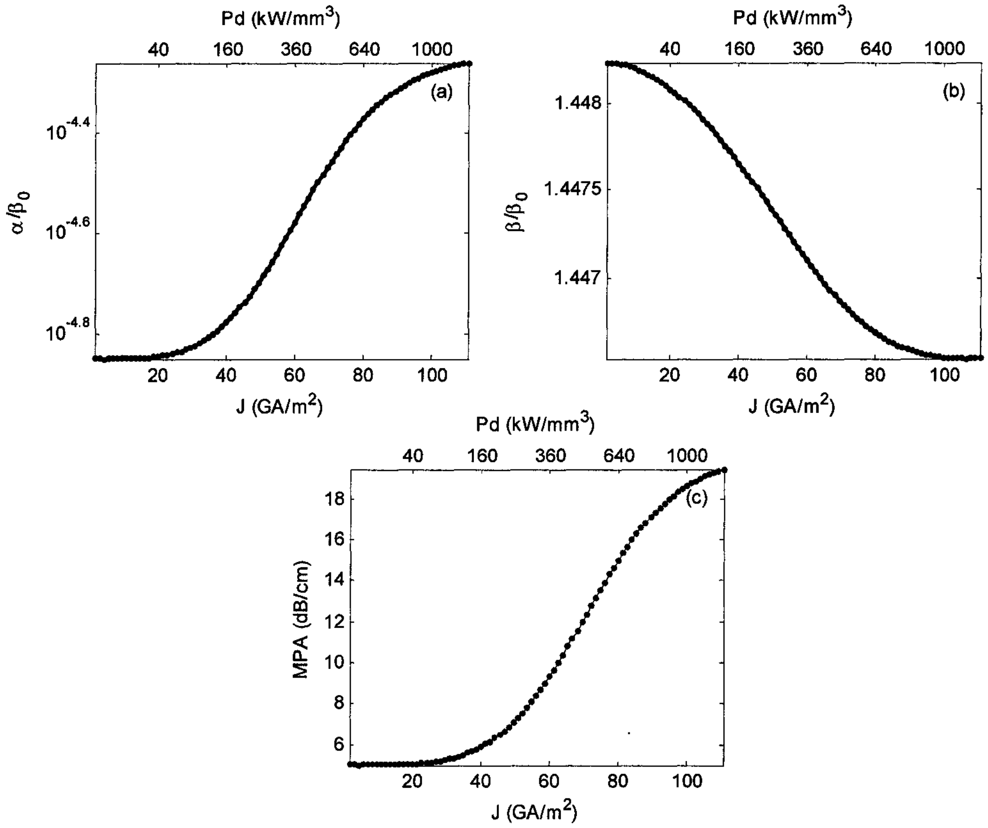

Figure D.4: Normalized attenuation constant, normalized phase constant and mode power attenuation of the s_L mode as a function of injected current density (or power density) for a 15nm thick metal film. The scale on top of each figure is nonlinear and represented by Pd=J^2/σ.

To address the design problem introduced in chapter 5, if the refractive index of the heat sink is matched to that of silica and the waveguide is heated, the mode would not be confined by the structure anymore and radiation would increase. This observation is made by comparing the Poynting vector of the least heated case in Figure D.4 with that of the matched structure in Figure D.6. Figure D.5 represent the normalized phase and attenuation constants as a function of film thickness for the s_L mode. The structure is an unheated waveguide with the following refractive indices: 1.4484, 1.4469, 0.55-11.5i, 1.4469 and 1 for the heat sink, silica, metal, polymer and air respectively. The refractive index of the heat sink was purposely set very close to that of the silica instead of matching it (given how the optical simulator was implemented, matching the refractive indices exactly would have generated erroneous results). The silica, metal and polymer are 15μm, 15nm and 124.985

μm thick respectively. The attenuation constant for a metal thickness of 15nm is shown to be higher than the least heated case of Figure D.2.

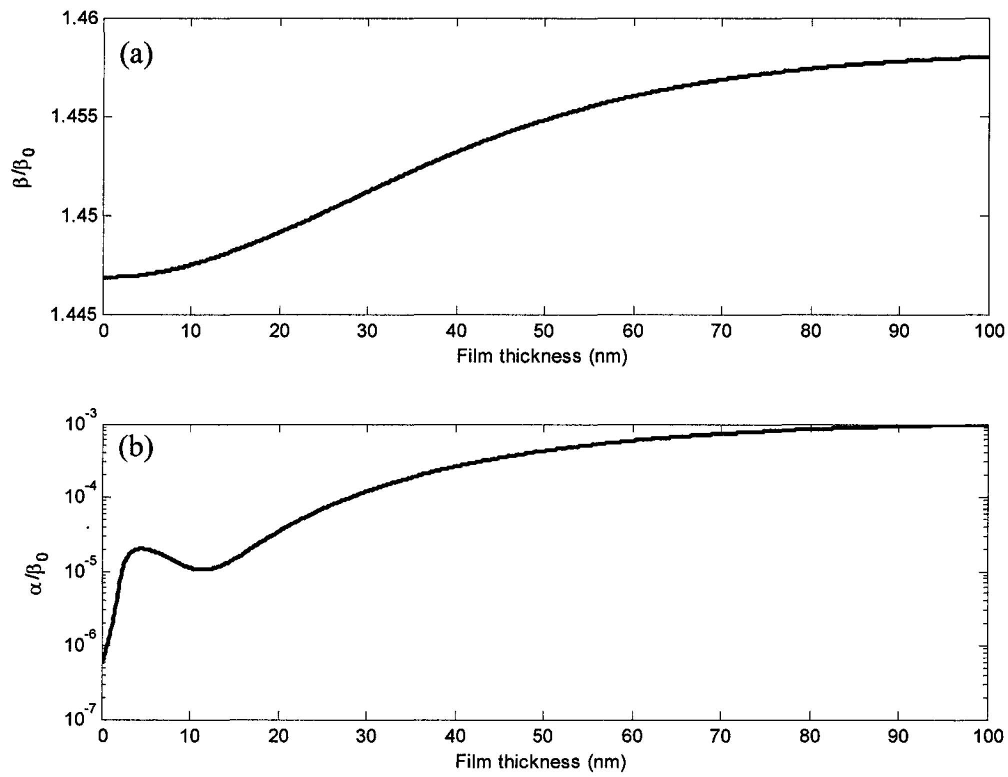

Figure D.5: Normalized phase constant and normalized attenuation constant when the heat sink's refractive index is matched to that of silica when the waveguide is not heated. The refractive indices are: 1.4484, 1.4469, 0.55-11.5i, 1.4469 and 1 for the substrate, silica, metal, polymer and air respectively.

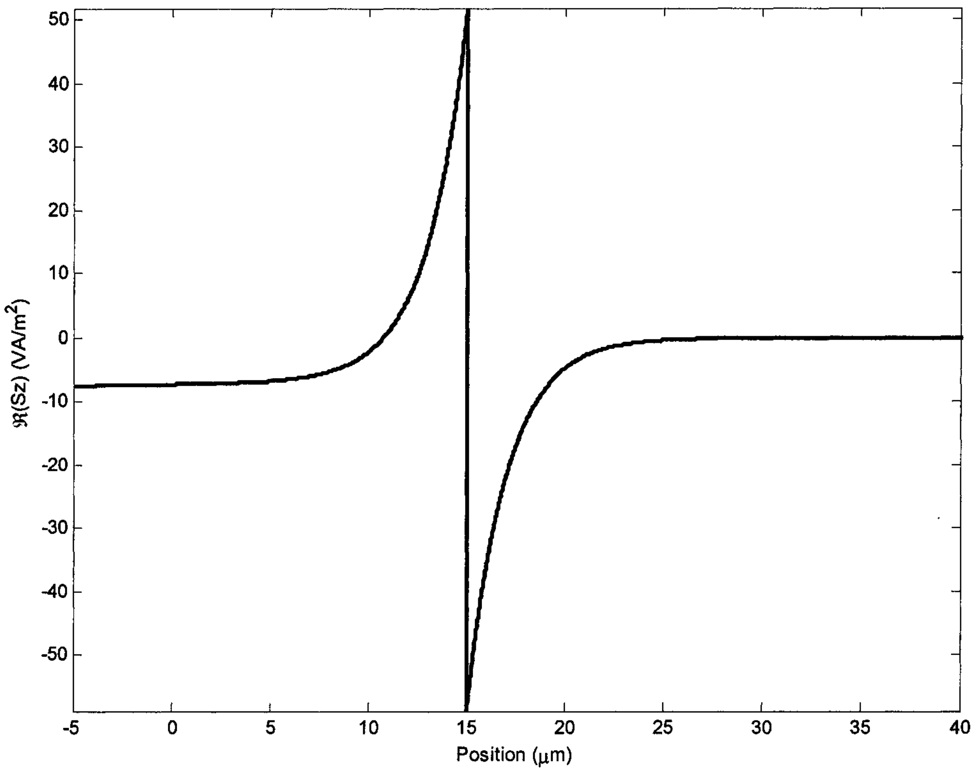

Figure D.6: Real part of the "z" component of the Poynting vector of a structure comprising a heat sink whose refractive index is matched to that of silica when the waveguide is not heated. The structure simulated comprises the following refractive indices: 1.4484, 1.4469, 0.55-11.5i, 1.4469 and 1 for the substrate, silica, metal, polymer and air respectively.